

DISSERTATION

QUANTIFYING AND UNDERSTANDING CURRENT AND FUTURE LINKS BETWEEN
TROPICAL CONVECTION AND THE LARGE-SCALE CIRCULATION

Submitted by

Andrea M. Jenney

Department of Atmospheric Science

In partial fulfillment of the requirements

For the Degree of Doctor of Philosophy

Colorado State University

Fort Collins, Colorado

Fall 2020

Doctoral Committee:

Advisor: David A. Randall

Co-Advisor: Elizabeth A. Barnes

Eric Maloney

Kristen Rasmussen

Georgiana Brooke Anderson

Copyright by Andrea M. Jenney 2020

All Rights Reserved

ABSTRACT

QUANTIFYING AND UNDERSTANDING CURRENT AND FUTURE LINKS BETWEEN TROPICAL CONVECTION AND THE LARGE-SCALE CIRCULATION

Tropical deep convection plays an important role in the variability of the global circulation. The Madden Julian Oscillation (MJO) is a large tropical organized convective system that propagates eastward along the equator. It is a key contributor to weather predictability at extended time scales (10-40 days). For example, variability in the MJO is linked with variability in meteorological phenomena such as landfalling atmospheric rivers, tornado and hail activity over parts of North America, and extreme temperature and rainfall patterns across the Northern Hemisphere.

Links between the MJO and atmospheric variability in remote locations are heavily studied. This is in part because the current skill of weather forecasts at extended time scales is mediocre, and because of evidence suggesting that the potential predictability offered by the MJO may not be fully captured in numerical prediction models. In the first part of this dissertation, I develop a tool for these types of studies. The "Sensitivity to the Remote Influence of Periodic Events" (STRIPES) index is a novel index that condenses the information obtained through composite analysis of variables after a periodic event (such as the MJO) into a single number, which includes information about the life cycle of the event, and for a range of lags with respect to each stage of the event. I apply the STRIPES index to surface observations and show that the MJO signal is detectable and significant at the level of individual weather stations over many parts of North America, and that the maximum strength of this signal exhibits regionality and seasonality.

Tropical convection affects the extratropics primarily through the excitation of Rossby waves at the places where the upper-tropospheric divergent outflow associated with deep convection interacts with the background wind. In a future warmer climate, the strength of the mean circulation and convective mass flux is expected to weaken. A potential consequence is a weakening of Rossby

wave excitation by tropical convective systems such as the MJO. In the second part of this study, I analyze a set of idealized simulations with specified surface warming and superparameterized convection and develop a framework to better understand why the mean circulation weakens with warming. I show that the decrease in the strength of the mean circulation can be explained by the slow rate at which atmospheric radiative cooling intensifies relative to the comparatively fast rate that the tropical dry static stability increases. I also show that despite a decrease in the mean convective mass flux, the warming tendency of the convective mass flux over the most deeply-convecting regions is not constrained to follow that of the global mean.

In the final part of this dissertation, I consider how changes in the MJO and of the mean atmospheric state due to warming from increases in greenhouse gas concentrations may lead to changes in the the MJO's impact over the North Pacific and North America. Specifically, I show that changes to the atmosphere's mean state dry static energy and winds have a larger impact on the MJO teleconnection than changes to MJO intensity and propagation characteristics.

ACKNOWLEDGEMENTS

This work would not have been possible alone and without help. I am particularly thankful to the National Science Foundation's Research Experiences for Undergraduates program, which introduced me to atmospheric science research and CSU. Thank you to my advisors, David Randall and Elizabeth Barnes, who have been extremely supportive, accepting, and encouraging. Thank you to my committee, Eric Maloney, Kristen Rasmussen, and Brooke Anderson for your time and feedback. I am extremely grateful for the larger CSU Atmospheric Science community, including the supportive faculty, the administrative staff, and the students. Much of this work relied on the technological and computational help of certain Randall group staff and scientists: Kelley Branson, Mark Branson, and Don Dazlich. I am also grateful to Kai-Chih Tseng and Stephanie Henderson for their help in running and understanding how to use the LBM. Finally, I would like to thank my husband, Tim Creed, for his constant support, and my family, for their love and acceptance.

This work was possible thanks to funding from the National Science Foundation (Grant AGS-1445191) and the National Oceanographic and Atmospheric Administration (Grant 4590155).

TABLE OF CONTENTS

	ABSTRACT	ii
	ACKNOWLEDGEMENTS	iv
Chapter 1	Introduction	1
1.1	The Madden-Julian oscillation and its teleconnections	1
Chapter 2	STRIPES index	6
2.1	Introduction	6
2.2	Data and Methods	8
2.2.1	Data	8
2.2.2	MJO	9
2.2.3	Composites	9
2.3	Calculation of the STRIPES Index	10
2.4	Application of the STRIPES Index to the MJO	15
2.4.1	Daily maximum temperature	15
2.4.2	Daily minimum temperature	19
2.4.3	Precipitation	20
2.4.4	Geopotential Height	22
2.5	Discussion	24
2.6	Summary and Conclusions	26
Chapter 3	The Seasonality and Regionality of MJO Impacts over North America	28
3.1	Introduction	28
3.2	Data and Methods	30
3.2.1	Observed MJO impacts	30
3.3	Results	31
3.3.1	Observed MJO Links	31
3.4	Discussion and Conclusions	35
Chapter 4	Climate change and the tropical mean circulation	37
4.1	Methods	40
4.1.1	Model	40
4.1.2	Diagnostics	41
4.2	Results	42
4.2.1	Mean circulation	42
4.2.2	Stratiform heating	50
4.2.3	Response of the convective mass flux to warming	54
4.2.4	Humidity dependence	61
4.3	Discussion and Conclusions	68

Chapter 5	The future MJO teleconnection	72
5.1	Introduction	72
5.2	Methods	75
5.2.1	Linear Baroclinic Model Simulations	75
5.2.2	Defining the MJO in CESM	78
5.3	Results	79
5.3.1	Simulated teleconnection change in CESM	79
5.3.2	Sensitivity experiments with a linear baroclinic model	80
5.4	Discussion and conclusions	90
Chapter 6	Conclusions	93
References		96
Appendix A	Supplemental figures	115

Chapter 1

Introduction

Tropical convection influences the climate of the entire earth. Some of the atmosphere's largest circulation features, including those associated with monsoon rainfall and the locations of deserts, are tightly coupled to convection in the tropics. Organized convection in the tropics is one of the major sources of weather predictability on "subseasonal-to-seasonal" (S2S) time scales of about 10-40 days, and is one of the key ways that the El Niño teleconnection is communicated to the globe from sea surface temperature anomalies in the equatorial Pacific. This dissertation focuses primarily on the impact of one specific tropical convective phenomenon, the Madden-Julian oscillation (MJO), on the extratropics.

1.1 The Madden-Julian oscillation and its teleconnections

The MJO is a regularly recurring, eastward propagating, organized storm cluster in the equatorial Indian and West Pacific Oceans (Madden & Julian, 1971, 1972). Its eastward propagation is slow, taking about 40 days to traverse the region from the Indian Ocean to the date line, although the periodicity of MJO convection can vary between about 35-95 days (Salby & Hendon, 1994). MJO convection is coupled to a strong circulation, consisting of upward motion and upper-level divergence in the region of precipitation, and sinking motion and upper-level convergence in the clear region.

The MJO is perhaps the strongest driver of intraseasonal variability over many extratropical regions (Robertson et al., 2015). It is able to affect weather in remote regions primarily through the excitation of Rossby waves. The divergent circulation associated with the MJO interacts with the background vorticity gradient, and can be a strong generator of vorticity in the jet stream area (Sardeshmukh & Hoskins, 1988; Mori & Watanabe, 2008; Seo & Son, 2012). There are many studies quantifying the influence of the MJO on the extratropics: its signal is detectable in observations of landfalling atmospheric rivers (e.g., Baggett et al., 2017; Mundhenk et al., 2016;

Ralph et al., 2010), precipitation (e.g., Curtis, 2017; DelSole et al., 2017; Jones et al., 2011; Lin, Brunet, & Mo, 2010; Zheng et al., 2018), temperature (e.g., Barrett, 2019; Johnson et al., 2014; Lee & Grotjahn, 2019; Matsueda & Takaya, 2015; Rodney et al., 2013; Zheng et al., 2018), and tornadoes (e.g., Baggett et al., 2018; Tippett, 2018; Gensini et al., 2019). In fact, the signal is sometimes strong enough to enable skillful empirical forecasts of these phenomena using just the MJO as a predictor (e.g., Baggett et al., 2018). Such studies have been important evidence demonstrating the potential for skillful predictions at S2S timescales. In Chapter 2¹, I develop an index, the “Sensitivity To the Remote Influence of Periodic Events” (STRIPES) index, that supports these types of studies. STRIPES quantifies the magnitude of the consistent MJO signal over a region as a single number by condensing the information contained in composites of a variable, such as wind speed, at various lags after the MJO, and with respect to the complete MJO life cycle. In addition to the novelty of the index, one of the key outcomes of this study is the new result that the MJO signal is detectable and significant at the level of individual weather stations.

The MJO’s teleconnections to the extratropics are strongest in the winter hemisphere (Knutson & Weickmann, 1987; Ghil & Mo, 1991). This is most likely due to the stronger tropospheric westerlies, which permit a broader spectrum of Rossby wave propagation through the atmosphere (e.g., Hoskins & Ambrizzi, 1993). Additionally, intraseasonal variability of tropical winds and outgoing longwave radiation over the Indian and West Pacific Oceans is stronger in boreal winter than in other seasons (Gutzler & Madden, 1989; Madden, 1986; W. Lu & Hsu, 2017). The boreal summer MJO behaves quite differently, with prominent northward and westward propagation an important part of the intraseasonal variability over MJO convective region, some of which is tied to the active and break periods of the Asian Summer Monsoon (Yasunari, 1979; B. Wang & Rui, 1990; Lau & Chan, 1986; B. Wang & Xie, 1997). While many MJO teleconnection studies have tended to focus on boreal winter, there is evidence that the MJO impacts weather over North America in other seasons as well. For example, the MJO is tied to variability of extreme heat

¹This study, titled “Quantifying regional sensitivities to periodic events: Application to the MJO,” has been published in *Journal of Geophysical Research: Atmospheres* (Jenney, Randall, & Barnes, 2019, ©2019 American Geophysical Union). The pre-typeset and copyedited version appears in this dissertation.

in California (Lee & Grotjahn, 2019), and to springtime tornado and hail variability over parts of North America (Baggett et al., 2018). In Chapter 3², I use the STRIPES index to explicitly quantify the seasonality of the observed MJO teleconnection over North America, and show that while across the region the strongest signals are indeed in winter, in some places the peak MJO teleconnection strength occurs in other seasons.

The strength of the MJO's circulation is important for the strength of the Rossby waves that it excites. To first order, latent heat release associated with MJO precipitation is balanced by the upward advection of dry static energy. Similarly, radiative cooling in the MJO's dry region is balanced by slow, adiabatic subsidence. The rate that air rises and sinks in the MJO's circulation is tightly constrained by, and inversely proportional to, the tropical dry static stability (Wolding et al., 2016). It is expected that the static stability will increase in the future as the tropical temperature profile adjusts towards the more stable moist adiabatic lapse rate of a warmer surface temperature. Ignoring changes to the intensity of the MJO's precipitation, this increase of the tropical dry static stability will likely decrease the strength of the circulation associated with the MJO, at least per unit precipitation (Bui & Maloney, 2018; Maloney et al., 2019). A potential consequence of this is a weakening of the excitation of Rossby waves by the MJO, and perhaps a subsequent weakening of the MJO teleconnection to the extratropics.

The projected weakening of the strength of the MJO's circulation is part of the broader-scale projected weakening of the strength of the mean tropical atmospheric overturning circulation, and of the mean convective mass flux, which is the rate that mass circulates through convective updrafts and downdrafts. Historical arguments used to explain why the future mean circulation and convective mass flux weaken rely on simple models of atmospheric moisture balance (Held & Soden, 2006). In Chapter 4³, aided by results from a set of idealized simulations with specified surface

²This study, titled "The seasonality and regionality of MJO impacts on North American temperature," has been published in *Geophysical Research Letters* (Jenney, Nardi, et al., 2019, ©2019 American Geophysical Union). A pre-typeset and copyedited subset of the text appears in this dissertation.

³This study, titled "Understanding the response of tropical ascent to warming using an energy balance framework," has been published in *Journal of Advances in Modeling Earth Systems* (Jenney, Randall, & Branson, 2020, ©2020 The Authors). The pre-typeset and copyedited version appears in this dissertation.

warming, I develop a diagnostic based on both energy and mass balance that links the strength of the mean circulation to heating rates in convective and clear regions. I show that the strength of the mean circulation weakens because of the relatively slow rate that atmospheric radiative cooling intensifies with warming. I also show that the climate change tendency of the convective mass flux over the most deeply convective regions is not constrained to follow that of the global mean. In other words, it may be possible for the MJO convective mass flux to increase, despite a weakening of the global mean.

In simulations of future MJO teleconnections, MJO circulation change does not correlate to MJO teleconnection strength change (W. Zhou et al., 2020). There are other avenues through which climate change can influence the MJO teleconnection aside from changes to the dry static stability of the tropics and the MJO's precipitation intensity. Previous work has shown that the MJO teleconnection is sensitive to its propagation speed (Bladé & Hartmann, 1995), its eastward extent (W. Zhou et al., 2020), and the strength and structure of the Pacific jet (Henderson et al., 2017; Tseng et al., 2019; Yun et al., 2011). Simulated future changes to the MJO are uncertain (Maloney et al., 2019). Not to mention, the MJO is poorly simulated in many models (Ahn et al., 2017). This makes trying to understand how the MJO teleconnection will change under increasing greenhouse gas concentrations a particular challenge. In Chapter 5⁴, I conduct simplified sensitivity experiments with a linear baroclinic model to probe the sensitivity of the MJO teleconnection to shifts in various features of the MJO and mean state. I do this in order to untangle the individual responses that climate changes to various mechanisms have on the MJO teleconnection over the northern Pacific and North America region. I show that the MJO teleconnection there is most sensitive to changes of the mean state, specifically of the dry static stability and winds, and less sensitive to changes in MJO intensity and propagation characteristics. Additionally, over many regions, changes in the winds compensate for increases in the dry static stability, resulting in stronger teleconnections over the North Pacific and North America.

⁴This study, titled "Mechanisms driving MJO teleconnection changes with warming," (Jenney, Randall, & Barnes, 2020, in prep) will be submitted to *Weather and Climate Dynamics*.

Results of the dissertation experiments and a discussion of the impact of this work are summarized in Chapter 6.

Chapter 2

STRIPES index

2.1 Introduction

Decision-makers who use weather and climate information can benefit tremendously from skillful forecasts in the 10-30 day range (White et al., 2017). For example, the serious human impacts of extreme weather events, such as heat waves, have prompted the agricultural, public health, and energy sectors to request and take advantage of extended-range forecasts of these events in order to save lives and money (Hudson et al., 2015). Ongoing efforts to improve weather forecasts at this timescale are motivated by growing evidence that improvements are indeed possible (Vitart et al., 2017; Mariotti et al., 2018)

Much of the potential for extended-range midlatitude weather prediction is linked to tropical deep convection (Hoskins, 2013; Zhang, 2013). The Madden-Julian oscillation (MJO, Madden & Julian, 1971, 1972) and other periodic weather events (PWEs) have repeatedly been shown to enable subseasonal-to-seasonal (S2S) prediction skill in midlatitudes (e.g., Lin, Brunet, & Fontecilla, 2010; Jones et al., 2011; Slade & Maloney, 2013; Johnson et al., 2014; Matsueda & Takaya, 2015; Black et al., 2017; DelSole et al., 2017; Mundhenk et al., 2018). Deep convection associated with the MJO excites Rossby waves that can travel poleward to both influence the immediate circulation (Hoskins & Karoly, 1981) and help maintain longer-lived climate modes such as the Pacific-North America or North Atlantic Oscillation patterns (Higgins & Mo, 1997; Mori & Watanabe, 2008; Cassou, 2008; Lin et al., 2009; Johnson & Feldstein, 2010; Moore et al., 2010), which themselves are important for extended-range weather prediction (Ferranti et al., 1990; Johansson, 2007).

As the forecasting community works towards skillfully applying the predictive power of PWEs (Hoskins, 2013), it will be important to quantify regional sensitivities to these events. Indeed, the results of various methods have already demonstrated regional variations in midlatitude sensitivity to tropical forcing. The strength and location of observed extreme temperature events and the

skill of their prediction appear to vary with MJO phase (Matsueda & Takaya, 2015; Diao et al., 2018). The frequency and intensity of precipitation over parts of North America are demonstrably sensitive to the intensity and location of tropical intraseasonal convection (S. Zhou et al., 2012; Moon et al., 2013; Jones & Carvalho, 2014). Furthermore, verifications of both statistical (Cassou, 2008; Slade & Maloney, 2013; Johnson et al., 2014; Zhu & Li, 2017; Mundhenk et al., 2018) and dynamical (Vitart & Molteni, 2010; Lin, Brunet, & Mo, 2010; Jones et al., 2011; Matsueda & Takaya, 2015) forecast models trained or conditioned on the MJO reveal regional variations in model skill, and thus hint at regional variations in teleconnection strength.

The MJO does not impact all mid- and high-latitude regions equally. The same is likely true for other PWEs with remote teleconnections. Identifying regional variations in climatological teleconnection signal strength is useful for application to subseasonal-to-seasonal predictability endeavors and for climate model evaluation. However, the results of methods heretofore used to identify these regions are difficult to present concisely. One commonly employed technique involves first subdividing a PWE into phases and then compositing a variable of interest after each phase. This method has been used extensively to evaluate the average state of the atmosphere following an MJO event (e.g., Bond & Vecchi, 2003; Jones et al., 2004; Donald et al., 2006; Cassou, 2008; Roundy et al., 2010; Lin, Brunet, & Fontecilla, 2010; He et al., 2011; Moon et al., 2011; Becker et al., 2011; Garfinkel et al., 2012; S. Zhou et al., 2012; Riddle et al., 2013; Matsueda & Takaya, 2015; Curtis & Gamble, 2016; Henderson et al., 2016). The results of such analyses are typically displayed using maps, each showing the composited variable at some lag after some specific time in the PWE's life cycle. Many maps are needed to show the composite response over the life cycle of the PWE, and even more are required to investigate how the response varies with lag. While overwhelmingly informative, this type of data presentation can be difficult to interpret, especially without a very specific question in mind.

Compositing methods can be presented much more succinctly if one dimension, such as space, is removed, as in Figure 2.1a. Here, the composited daily maximum temperature (TMAX) at a weather station in eastern North America is presented for all phases of the MJO for lags ranging

from 0 to 50 days after the occurrence of MJO events. This approach presents the composited behavior of a variable at a specific location, for a large number of lags, and over the entire life cycle of the PWE. Drawbacks of composites like Figure 2.1a include the need to specify a location before construction. Thus, in order to identify the large-scale mechanisms responsible for any apparent teleconnections, composites such as that shown in Figure 2.1a are insufficient, and maps are again required.

Here, I present the “Sensitivity to the Remote Influence of Periodic EventS (STRIPES)” index, which concisely quantifies the magnitude and consistency of a region’s response to the remote influence of PWEs. The STRIPES index offers an advantage over other types of compositing methods because it compiles the two dimensions of temporal information (PWE phase and lag after the PWE) into a single numerical value—something not possible with composite maps. As a demonstration and proof-of-concept, I apply the STRIPES index to surface weather observations in North America and global geopotential heights after the MJO.

2.2 Data and Methods

2.2.1 Data

To demonstrate the STRIPES method, I use daily surface observations of TMAX, minimum temperature (TMIN), and precipitation totals (PRCP) from the Global Historical Climatological Database-Daily (Menne et al., 2012). Only weather stations in North America that have at least 50% of data for at least 50% of winters (the entire months of December, January, February) are considered. This leaves 6580, 6589, and 8552 available stations for TMAX, TMIN, and PRCP, respectively. Most station data is in fact much more complete; for each variable at least 72% of stations are at least 70% complete for at least 70% of winters. Geopotential height and precipitable water data are from the NCEP/NCAR Reanalysis 1 (Kalnay et al., 1996). Data is from the years 1974 to 2017. The data are converted to anomalies by removing the long-term mean, the first three annual harmonics, and any linear trend.

2.2.2 MJO

The MJO is characterized using the Real-time Multivariate MJO index (RMM, defined by Wheeler and Hendon (2004)). MJO phases are defined by the angle between the first two principal components of the RMM index (RMM1, RMM2), which determines where a given day falls in a two-dimensional phase space that has been divided into eight equal sections.

For all composites, independent MJO phase days are used to ensure that composites do not give extra weight to slower-moving MJO events (i.e., MJO events that spend more consecutive days in a given phase). For a given phase, independent days are chosen by first grouping all occurrences of an MJO phase into events. An event is defined as any occurrence of consecutive days of an MJO phase. Disregarding all days below an amplitude threshold ($\sqrt{\text{RMM1}^2 + \text{RMM2}^2} < 1$), the first occurrence of the MJO phase in each event is then chosen to construct composites. This leaves a mean number of 121 independent days per phase (with a range of 98 to 139) that are used to construct composites. The results are qualitatively similar when all days within an MJO phase, instead of independent days, are used for composites (see Appendix A Figures A.1-A.3).

2.2.3 Composites

Two-dimensional lagged composites (henceforth, “2D composites”) of observations after active MJO days are constructed (see Johnson et al., 2014; Baggett et al., 2017; Mundhenk et al., 2018; Zheng et al., 2018). Composites are created for each station (grid point) for surface (reanalysis) data. All station and reanalysis anomalies have first been standardized by subtracting their individual winter means (over all winters) and dividing by their winter standard deviations, so that regions with different climatological variabilities are comparable. Standardization desensitizes the STRIPES index to the climatological variance of the variable at that station or grid point. Figure 2.1a shows an example 2D composite for TMAX at a station in eastern North America. The figure shows diagonal stripes of the same sign, which are oriented from bottom left to top right, and that have a slope of about 6 days per phase. These stripes are consistent with propagation of the MJO (Wheeler & Hendon, 2004). An organized response to the MJO is evident even when the MJO

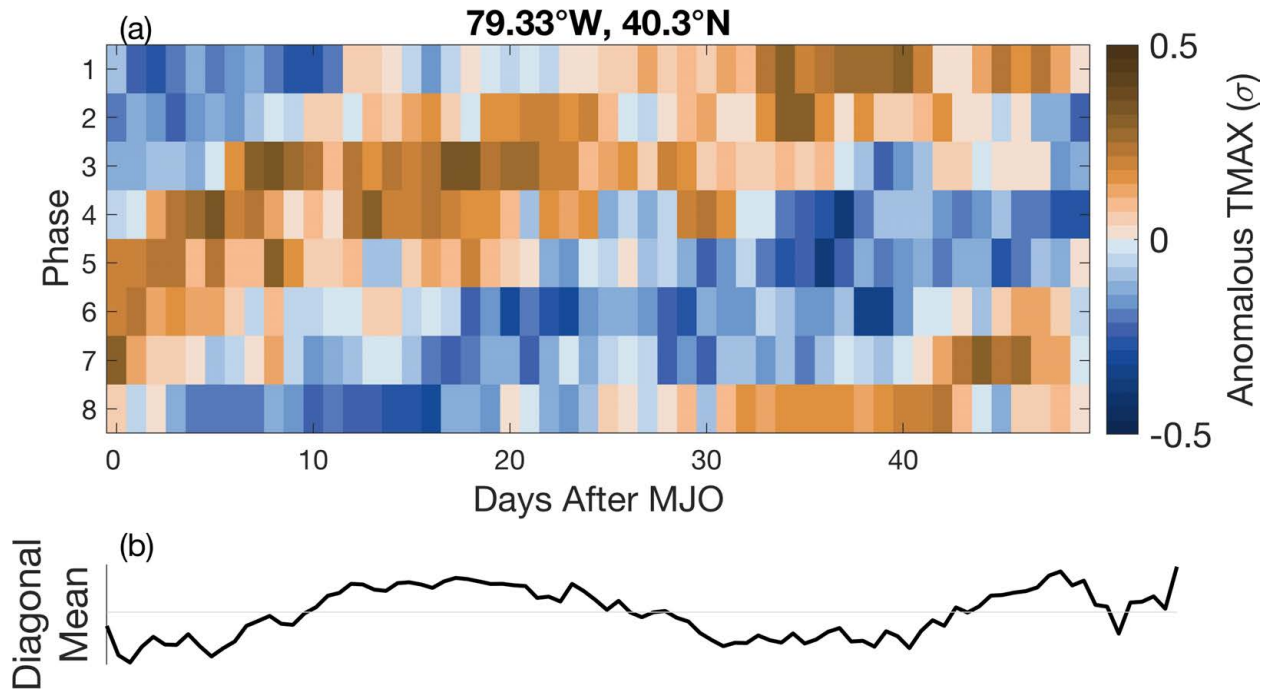


Figure 2.1: (a) Composited daily maximum temperature anomalies at a weather station indicated by the coordinates (in southwest Pennsylvania) after independent MJO days. The data has been standardized so that anomalies are in units of standard deviations. (b) Resultant vector when diagonal averages are taken of (a) along lines with a slope of 6 days per phase.

precedes the TMAX anomaly by as much as 50 days. This is quite remarkable: Although the magnitudes of the composites within the stripe are small, sensitivity of TMAX to the MJO is evident even at a single weather station, where no area or temporal smoothing has been applied. Additionally, diagonal stripes indicating sensitivity to the MJO are clearly discernible despite averaging over more than 40 years of MJO events. I choose to omit showing the significance of composites at a given lag and phase to emphasize the stripe patterns within these composites, not on the value or sign of the composite response to the PWE at a given point.

2.3 Calculation of the STRIPES Index

Two dimensional composites, such as those shown in Figure 2.1a and Figure 2.2a, present information about the time evolution of the local response to a remote forcing by a PWE. Of note is the appearance of diagonal stripes, oriented from bottom left to top right. When these stripes alternate sign from left to right, and have a slope consistent with the periodicity of the PWE, they

provide support for a physical link between the PWE and the composited variable. Compositing over many events helps to filter out variability not due to the PWE and isolates consistencies over many events. In these cases, the appearance of diagonal stripes provides even stronger evidence for a systematic, physical link between the PWE and the composited variable.

The calculation of the STRIPES index is based on these 2D composites, and aims to quantify the amplitude of the stripes. An area that is not sensitive to the PWE will have 2D composites that appear noisy, have weak overall amplitudes, and contain no systematic stripes. Conversely, areas that respond to the PWE with larger magnitudes and more consistency will have prominent, and sometimes multiple, stripes.

The STRIPES index can be technically understood as the variance of a one-dimensional vector of values obtained as averages taken along the diagonals of the 2D composites. Figure 2.2 is a synthetic example intended to aid in the interpretation of this algorithm. Here, a synthetic 2D composite has been drawn, with amplitudes reaching 0.25 standard deviations, which decrease by 30% at a lag of 50 days. I include this decrease in amplitude with lag to make the synthetic composite more realistic.

Diagonal averages are taken along lines with a slope consistent with the periodicity of the PWE. In the artificial example shown in Figure 2.2, a slope of 6 days per phase is shown because the MJO spends about 6 days in each RMM phase before transitioning to the next (Wheeler & Hendon, 2004). Four of these diagonal lines and their sums are visualized in Figure 2.2. Boxes of the same color lie along one of these diagonal lines, and each box indicates the point used in that line's diagonal average. These points are separated in time by 6 days. For each diagonal line, only one day per phase is used in averages. Figure 2.2b shows the one-dimensional vector that results when diagonal averages of Figure 2.2a are taken. The colored squares on the curve indicate the averages for the diagonal lines indicated by boxes of the same color in Figure 2.2a. The sinusoidal shape of the one-dimensional vector of diagonal averages is a result of robust stripes of alternating sign in the 2D composite.

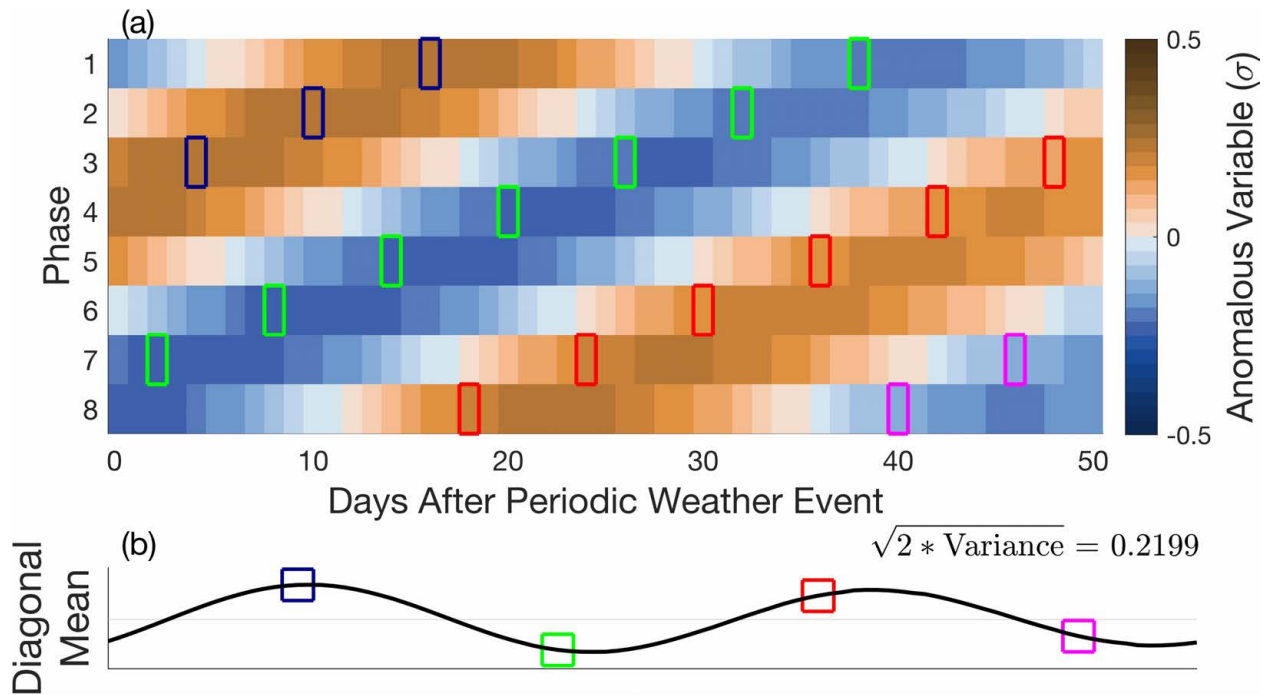


Figure 2.2: (a) Synthetic composited variable after many ostripeoccurrences of an active PWE. Maximum amplitude anomalies are 0.25 standard deviations, and decrease to 70% of that at 50 days. The STRIPES index is constructed by taking averages of composites along the diagonal along which the stripes occur, and using the value of each average to construct a vector. (b) The resultant vector for the synthetic data, with the average stripe amplitude ($\sqrt{2 * \text{variance}}$) shown in the top right. Colored boxes at specific points of the curve demonstrate the value of the average taken along the diagonal indicated by the line of similarly-colored boxes in (a). The slope along which the diagonal averages are taken is 6 days per phase.

After the diagonal averages are taken, the variance of the resulting one-dimensional vector is calculated. For a perfect sine or cosine function, the variance is one half the square of the amplitude. Thus, the variance of the curve can be transformed into an amplitude by taking the square root of twice its value. This transformation helps convert the index into a number that conveys the average magnitude of composites along its diagonal stripes. The number that results from this transformation is, in essence, the STRIPES index. For the synthetic composite shown in Figure 2.2, the amplitude that results is 0.2199. This is roughly the magnitude of the composites within the stripes (0.25), but is smaller because of the specified 30% decrease in amplitude with lag. If maximum amplitudes along stripe axes in Figure 2.2 were 0.25 everywhere, then the STRIPES index for this composite would also be 0.25. The STRIPES index for Figure 2.2 would be lower if one or multiple of its diagonal stripes was comprised of an equal number of positive and negative points, such that the diagonal average of that line was near zero. The STRIPES index has a single value at each geographical point, meaning it can be plotted on a map to show regional variations in apparent sensitivity to a PWE. This makes it particularly useful.

While the steps described above create the fundamental STRIPES index, I take additional steps to remove minor sensitivities. Nonetheless, the STRIPES index is robust as described, and gives qualitatively similar results to those with the following additional steps (see Appendix A Figures A.4-A.6). First, I repeat the calculation of the index N times, where N is the number of phases used to subdivide the PWE. In each iteration, the PWE's subdividing phases are shifted before computing the variance of diagonal averages. This gives N values for the final variance, which are then averaged together to get a single value for the variance. The shifting captures those stripes in the composites that are due to periodic behavior (i.e., returning to the beginning of the event after completing a cycle). For example, in one iteration, instead of the ordinate axis of the composite shown in the top panel of Figure 2.2 running from phase 1 to 8, it runs from phase 5 to 8, and then 1 to 4. Inspection of Figure 2.2a shows that stripes appear to extend beyond phase 8 or before phase 1. Each iteration of this calculation contributes a variance value. The STRIPES indices presented in Section 2.4 use the average of the 8 variances obtained with this shifting. Second,

I average together the four variances obtained using slopes between 4 and 7 days. This is done to account for the variability in MJO periodicity (e.g., Hendon & Salby, 1994). The final result is a single variance, which is then transformed into an amplitude that quantifies the magnitude and consistency of a region's response to the remote influence of PWEs. This number can be interpreted as the average value (in standard deviations) of composites along the stripes in the 2D composites.

The significance of the STRIPES index at each weather station is calculated using a one-tailed bootstrap test with 500 samples at $\alpha < 0.05$. To create the samples, MJO days are first separated into chunks of consecutive days with amplitudes greater than 0.5. I then randomly sample from fall and winter (all of winter plus the 50 days prior to winter) a distribution of days with the same distribution as the chunks. For example, if there are 10 MJO chunks each with a length of 5 days, I randomly sample 10 chunks of 5 consecutive days. I assign a phase value to each of these randomly selected days based on the phase value of the true events. For example, if the first of the true MJO events of length 5 are made up of three consecutive days in phase 3 and then two days in phase 4, then the randomly selected data will be given the same phase values. Selecting the random samples in this way ensures that the autocorrelations between and within phase values are retained. Next, only the indices of true MJO days whose amplitudes are greater than 1 are used to construct the composites making up the bootstrap samples. As in the composites of observed data, I use independent random days that have been selected in the same manner as described previously, and construct 500 2D bootstrap composites for each weather station and variable. Finally, I calculate the STRIPES index for each of the bootstrap composites to create a distribution of STRIPES indices that can arise due to random chance. Those stations with a STRIPE index larger than the 95th percentile of their respective distribution are considered significant.

The STRIPES index has a lower bound of zero and no upper bound. Diagonal stripes in the 2D composites that are not consistent with the periodicity of the PWE will not contribute positively to the index. The STRIPES index is insensitive to the location of a stripe in the 2D composites. For example, a 2D composite like the one shown in Figure 2.2a, but with stripes that are in quadrature

with those of Figure 2.2a, will have the same STRIPES index as Figure 2.2a. The STRIPES index will have a larger magnitude if, for a given PWE, there are multiple stripes (e.g., if a PWE excites an opposite-signed response every half cycle) or if stripes are particularly strong. Although multiple stripes can appear in the 2D composites for PWEs with a shorter period, the index is not sensitive to the periodicity of the PWE. Using the variance as a measure of stripe magnitude helps to amplify actual stripe signals while suppressing noise.

The STRIPES index can be applied to a variety of PWEs. While the specific values given in the methods described here and the application of the index in Section 2.4 are for the MJO, the same approach can be applied to any other PWE whose life cycle is smoothly periodic and can be subdivided into distinct phases, such that 2D composites like the one shown in Figure 2.1a and Figure 2.2a can be constructed. For example, consider a PWE that has a periodicity of 24 days. If 8 phases are still being used to subdivide the event, then a slope of about 3 days per phase should be used in diagonal averages rather than 6, as was shown here. Similarly, if a PWE with a period similar to that of the MJO is only being subdivided into 4 phases rather than 8, then a slope of about 12 days per phase should be used in diagonal averages.

2.4 Application of the STRIPES Index to the MJO

Next, the STRIPES index is applied to observations at North American weather stations and to global 500 hPa geopotential heights following MJO events to quantify the magnitude and consistency of local responses to the MJO.

2.4.1 Daily maximum temperature

Figure 2.3a shows the winter STRIPES index for daily TMAX. STRIPES for geopotential height at 500 hPa are overlaid as red contours. Units of the STRIPES index are in standard deviations, so that the variability of a region's temperature or geopotential height is not encoded in the magnitude of STRIPES. However, the STRIPES index can also be presented in variable units to get a sense of the magnitude of the variability associated with the MJO in measurable quantities.

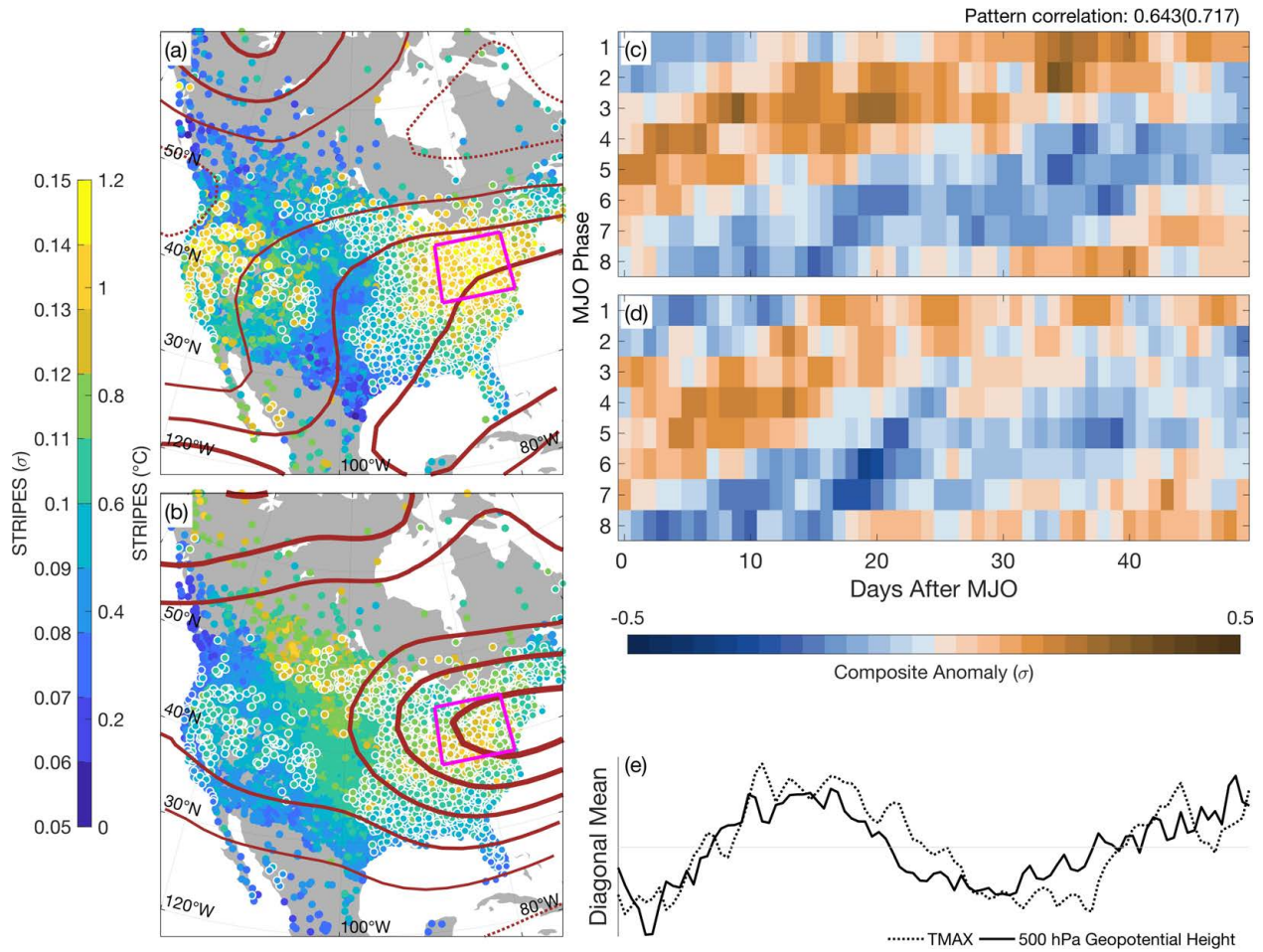


Figure 2.3: (a) STRIPES index for North American weather stations (each point on the map is a unique weather station) for TMAX (points) and 500 hPa geopotential height (contours) after the MJO for the years 1974-2017 in (a) standard deviations. Contours start at 0.06 (dotted) and increase in value with thickness by 0.02 (solid). (b) As in (a), but STRIPES is shown in $^{\circ}\text{C}$ for TMAX and m for geopotential height. Contours start at 2 m (dotted) and increase in value with thickness by 2 m (solid). (c) 2D composite of TMAX for the region enclosed by the magenta box (33° - 44.5°N , 75.5° - 86°W). (d) 2D composite of 500 hPa geopotential height for the region enclosed by the magenta box. (e) Diagonal means of the composites using a slope of 6 days per phase.

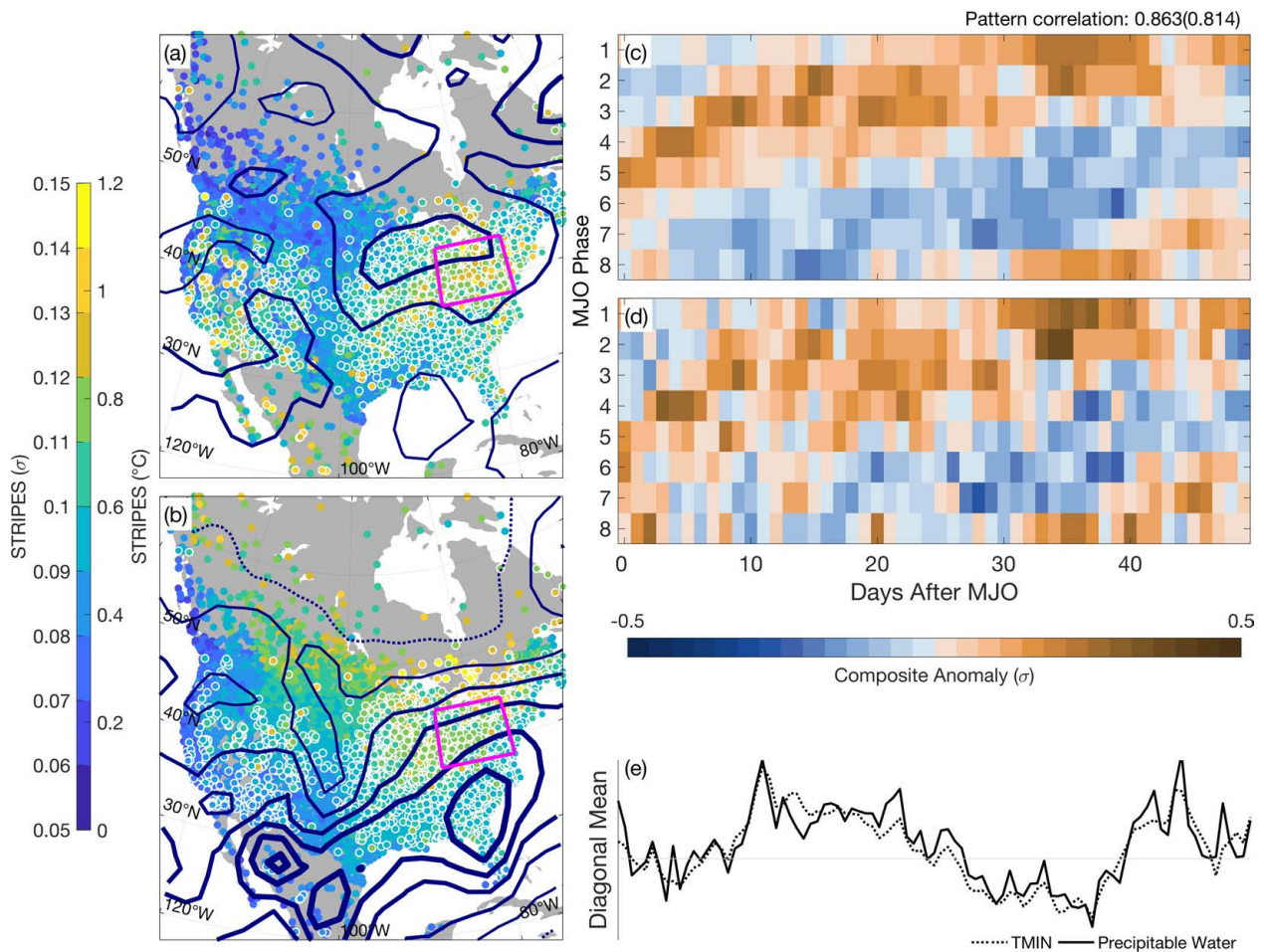
This is shown for TMAX and 500 hPa geopotential height in Figure 2.3b, where the STRIPES index at each point has been multiplied by the local standard deviation.

A strong hotspot for local modulation of TMAX by the MJO is over eastern North America, as shown by the large magnitudes of the STRIPES index over this region in Figure 2.3(a,b). This hotspot also appears in previous studies employing alternate methods. Zheng et al. (2018) also identified strong MJO covariability over eastern North America in winter. Additionally, composites of winter near-surface air temperature and geopotential height anomalies after RMM phases of the MJO have large magnitudes with strong significance over eastern North America relative to other North American regions (S. Zhou et al., 2012; Schreck et al., 2013; Baxter et al., 2014; Matsueda & Takaya, 2015). Finally, the MJO appears to be linked with the skill of temperature forecasts particularly over eastern North America (Johnson et al., 2014; Matsueda & Takaya, 2015).

Figure 2.3a indicates that the region of elevated surface TMAX sensitivities is collocated with a tongue of high sensitivities in 500 hPa geopotential height stretching westward from the Atlantic Ocean, suggesting that MJO-induced circulation anomalies over the East Coast play a key role in the MJO-coincident TMAX variations at the surface. This is expected: The remote MJO must communicate its signal to North America through a control on larger-scale circulations in order to influence weather at the surface. Seo et al. (2016) show that low-level horizontal advection is the dominant process through which the MJO influences temperatures over this region. Figure 2.3c shows the 2D composite for TMAX area-averaged (as in McKinnon et al. (2016)) over the region enclosed by the magenta box in Figure 2.3(a,b). Warm anomalies over this region occur around 10 days after MJO Phase 3. When this occurs, Seo et al. (2016) show that the circulation pattern characterized by an anomalous low over Alaska and high over the Atlantic encourages warm air advection over eastern North America, which is situated between the two circulation anomalies. Figure 2.3e, which shows the diagonal means of the 2D composites for TMAX and 500 hPa geopotential height (Figure 2.3d) for the boxed eastern North America region, shows this pattern. Anomalous warm temperatures tend to follow maxima in anomalous geopotential height. That is, warm (cold) air advection ramps up when the center of the anomalous high (low) associated with

the Rossby waves excited by the MJO propagate just east of the region. Thus, for a given point, there is some time in between maxima (minima) in geopotential height and subsequent near-surface temperature maxima (minima).

Figure 2.3(a,b) indicates that western North America, especially along coastal California, also displays significant sensitivity to the MJO. Although weaker in amplitude than eastern North America, this is a region that has been previously shown to covary with the MJO (S. Zhou et al., 2012; Schreck et al., 2013; Baxter et al., 2014; Johnson et al., 2014), and more significantly so when finer resolution temperature data are used (S. Zhou et al., 2012; Baxter et al., 2014).



2.4.2 Daily minimum temperature

The spatial pattern of TMIN sensitivity to the MJO closely resembles that for TMAX (Figure 2.4(a,b)). The strongest STRIPES indices are also located over eastern North America, but with weaker magnitudes than for TMAX.

Over land, daily minimum temperature is closely linked with atmospheric moisture (e.g., James, 1953; Hartmann, 1994). Boundary-layer temperature minima tend to occur at the end of the night after hours of longwave cooling and no solar energy input. Water vapor is the largest contributor to downwelling longwave radiation (Hartmann, 1994). On nights when column moisture is relatively low, there is less downwelling longwave radiation to counteract the efficient surface longwave emission, effectively permitting lower temperature minima. Conversely, on relatively humid nights increased downwelling radiation from water vapor acts to keep the nocturnal temperature from falling as low as it would otherwise. The STRIPES index contours for standardized precipitable water in Figure 2.4a show that the strongest sensitivities in precipitable water over North America are over and to the southwest of the Great Lakes region (see Appendix Figure A.7 for a global map of the STRIPES index for precipitable water). Figure 2.4 shows composited anomalies of both (c) TMIN and (d) precipitable water for the region enclosed by the magenta box in Figure 2.4(a,b). Higher (lower) anomalies in precipitable water are coincident with warmer (cooler) daily minimum temperatures. Here, pattern correlations (indicated by the number to the top right in Figures 2.3c and 2.4c) between TMIN and precipitable water are much stronger than between TMAX and 500 hPa geopotential height. This is likely due to the effect of moisture on TMIN: daily minimum temperatures respond to the amount of moisture present in the column, as discussed previously. Figure 2.4e confirms that stripes of local maxima and minima in TMIN and precipitable water occur at the same time.

Some of the correspondence between TMIN and precipitable water is likely also due to advection. As mentioned previously, the MJO primarily influences the thermodynamics of this region through low-level advection (Seo et al., 2016). Southerly (northerly) advection of mean state temperatures not only brings relatively warmer (cooler) air, but also more (less) humid air. Because of

the dynamical link between temperature and moisture, when temperatures are anomalously warm due to warm air advection from the south, absolute humidities are also likely to be elevated for the same reason.

There is an additional hotspot of sensitivity to the MJO for TMIN over the southwest. The significant weather stations are mostly located in the desert southwest, to the north and east of the Gulf of California, whereas for TMAX the significant weather stations in this part of the continent are located further west. This difference is likely due to the presence of the strong hotspot for column moisture near this region (see Figure 2.4c), to which TMIN is more sensitive. Sensitivity to the MJO over western North America was not detected in the recent analysis of Zheng et al. (2018). In their study, the authors analyzed $2.5^\circ \times 2.5^\circ$ resolution gridded daily means of surface air temperature data. They were likely unable to detect the signal over this region through some combination of the coarseness of the resolution of their data, and their use of daily mean temperature values. Note that only a few western weather stations show significant signals for both TMAX and TMIN.

2.4.3 Precipitation

Previous work indicates that the MJO strongly modulates winter moisture (Mo & Higgins, 1998), flooding (Bond & Vecchi, 2003) and atmospheric rivers (Ralph et al., 2010; Mundhenk et al., 2016) over the North American Pacific Coastline. Figure 2.5(a,b) shows that weather stations with significant signals in PRCP are clustered in this region, in addition to parts of the southeast. Here, weather stations with standard deviations less than 1 mm day^{-1} are plotted as grey points to ignore weather stations with small variability. The recent analysis of Zheng et al. (2018) also indicates strong co-variability with the MJO over these two regions, in addition to a peak over the central portion of the continent which was not detected with any significance in this analysis. This may be a consequence of the very noisy nature of precipitation data: Daily station rainfall time series are noisy, have highly asymmetric distributions, and contain a disproportionate number of zero values. Thus, I expect STRIPES results for this type of data to appear differently than

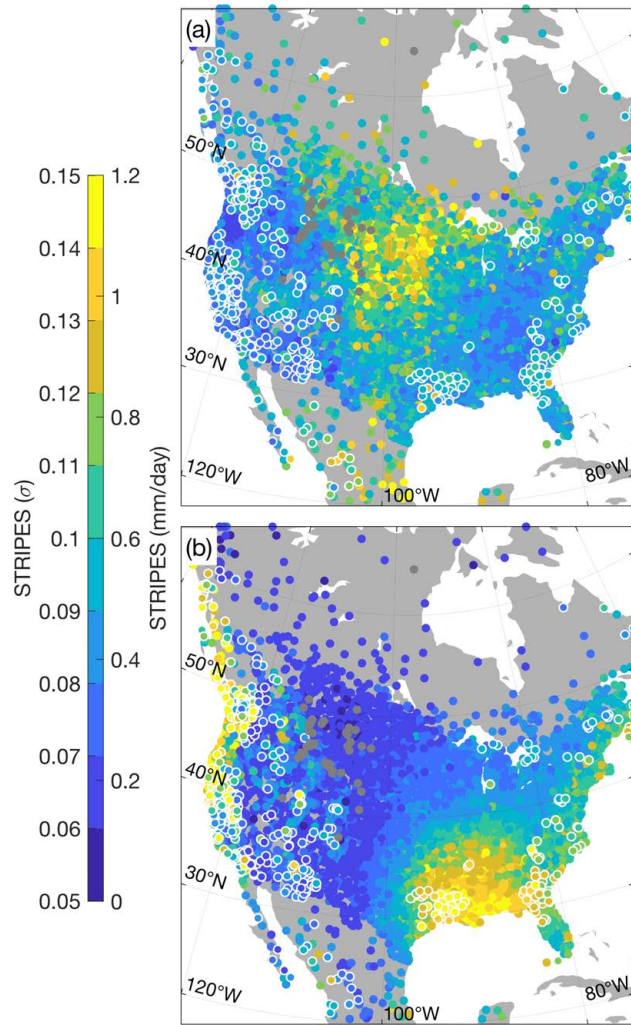


Figure 2.5: As in Figure 2.3(a,b) but for PRCP. Stations with standard deviations less than 1 mm day^{-1} are plotted as grey circles.

for data like TMAX, for example. Experimentation with a log or hyperbolic sine transformation indeed aided in reducing the skewness of daily rainfall data, but the overwhelming number of zero values is such that the STRIPES index analysis results for PRCP do not change much even with the transformation applied (not shown). Smoothing, for example by taking 10-day running means or bandpass filtering to retain only the intraseasonally varying component of the signal as in Zheng et al. (2018), or through spatial averaging, may increase the magnitude of the STRIPES index for this type of data.

In standardized values (Figure 2.5a), the magnitude of the STRIPES index appears to be largest over central North America. However, this central cluster of points is not significant, even when using a relaxed confidence threshold of $\alpha \leq 0.20$ (not shown). Note that when viewed in mm day^{-1} (Figure 2.5b), rather than in standard deviations, this region disappears, and the regions shown to be significant now show the largest magnitudes.

2.4.4 Geopotential Height

I include the STRIPES index for global 500 hPa geopotential heights to give some indication of the global effects of the MJO. As expected, Figure 2.6a shows that the strongest sensitivities for 500 hPa geopotential height for winter are over the equatorial Indian and Pacific Oceans, where MJO variability is most pronounced. Notable is the pattern of higher STRIPES values in the extratropics. There is strong regionality in the co-variability of extratropical geopotential heights with the MJO. For example, the couplet comprised of the center just south of the Aleutian Islands and the center over northwest North America is reminiscent of the Pacific-North America pattern, a teleconnection pattern associated with the MJO (Mori & Watanabe, 2008; Goss & Feldstein, 2015; Seo & Lee, 2017). There are many regions whose local circulations show strong co-variability with the MJO. While our analysis mainly focused on North America, the circulations of much of Africa, southeast Asia, eastern Australia, and eastern equatorial South America show stronger sensitivities to the MJO than that over North America. In short, the effects of the MJO are widespread.

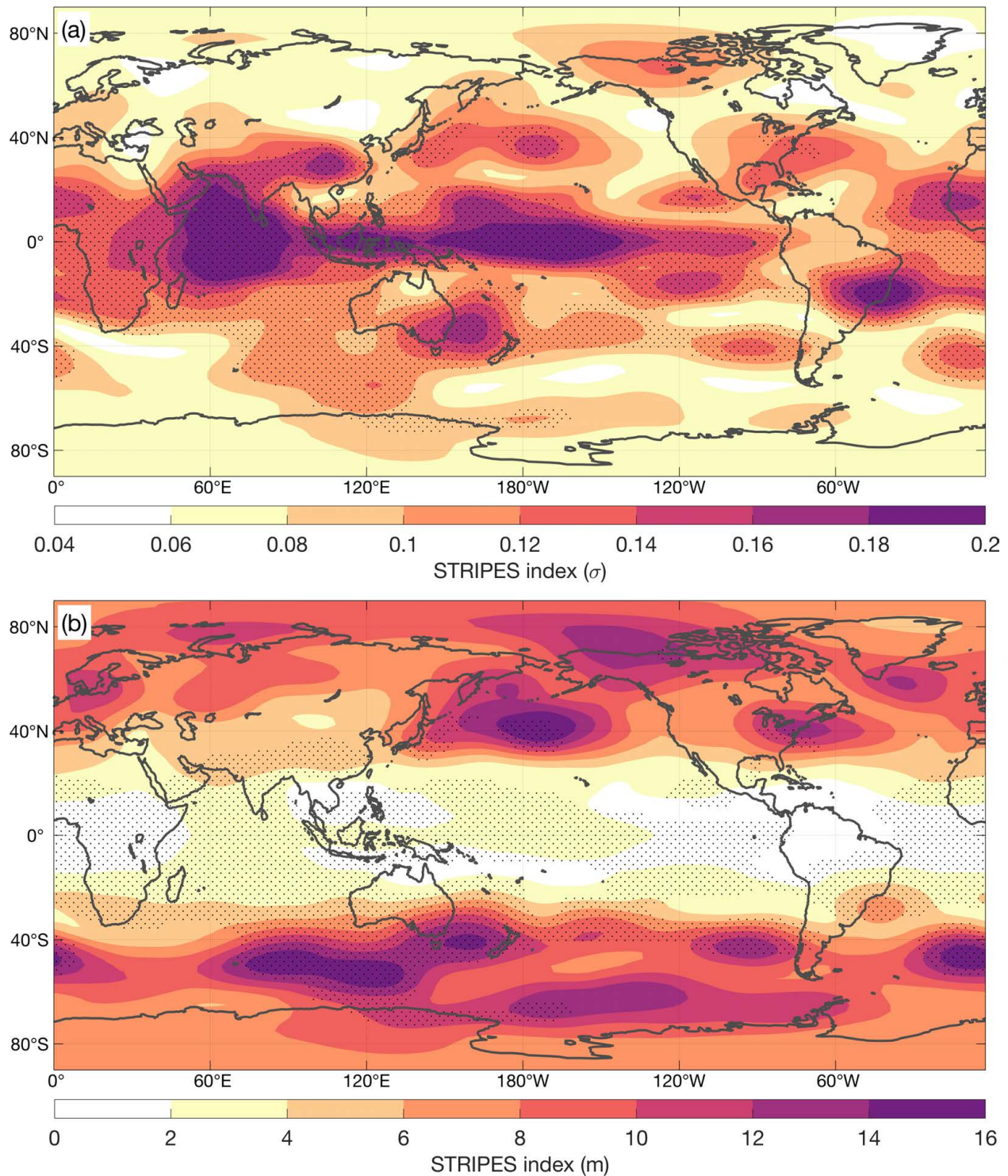


Figure 2.6: (a) STRIPES index for 500 hPa geopotential height after winter (DJF) MJO events for the years 1974-2017. (b) STRIPES index at each point has been multiplied by its local standard deviation. Stippling denotes significance at $\alpha < 0.05$.

Figure 2.6b shows STRIPES indices multiplied by local standard deviations. This translates the STRIPES quantities from units of standard deviation into measurable quantities. Low geopotential height variability in the tropics causes the high sensitivities there to disappear (although they remain significant). Conversely, regions along the Pacific and Atlantic storm tracks are amplified. Maps such as Figure 2.6 indicate which regions of the globe respond with greater magnitude and consistency to an MJO event.

2.5 Discussion

I present the STRIPES index as a concise way to quantify the magnitude and consistency of a region's response to the remote influence of PWEs. Its units are in standard deviations, and signify the average amplitude of the stripes within a region's 2D composite. However, the interpretation of the STRIPES index *as an amplitude* relies on the assumption that the one-dimensional vector of diagonal averages assumes a sinusoidal shape. This will only occur when the 2D composites have stripes of alternating sign; i.e., when the PWE excites opposite-signed responses every half cycle. Thus, some caution is advised in the interpretation of the STRIPES index as an amplitude. For example, the STRIPES index amplitude for 2D composites characterized by one very strong stripe, but near-zero composites everywhere else will be much lower than the average magnitude of composite quantities within the stripe. Nonetheless, the STRIPES index for such a region will still have a larger value than a similar composite that contains no stripes.

STRIPES indices can be converted back into variable units by multiplying by the standard deviation at each point, as in Figure 2.3b and Figure 2.4b. Such a transformation shows how the teleconnection strength over a region translates to measurable quantities. For example, Figure 2.3a shows that the average magnitude of anomalies in stripes of the 2D composites of TMAX after the MJO over eastern North America are about 1°C. Note how the central North American hotspot for PRCP in Figure 2.5a disappears when this transformation is applied in Figure 2.5b, while new hotspots over regions with larger climatological variabilities, such as the previously discussed North American Pacific coastline, pop out.

As constructed, the STRIPES index is better suited to data that is symmetrically distributed. Additionally, while there are a number of periodic weather phenomena (e.g., the El Niño Southern Oscillation, the North Atlantic Oscillation, and the Quasi-Biennial Oscillation) the index requires that the event be somewhat smoothly varying. For example, climate phenomena characterized by irregular or sudden transitions between regime states, such as sudden stratospheric warmings (e.g., Limpasuvan et al., 2004), don't produce diagonal stripes when composites such as the ones shown in Figure 2.1 and Figure 2.2 are constructed, and thus, the STRIPES index would not be useful for these phenomena. Instead, the index is designed to work with PWE that somewhat smoothly and consistently evolve through their life cycles. For example, the STRIPES index can be successfully applied to the Quasi-Biennial Oscillation.

Because the STRIPES index allows the concise quantification of the magnitude and consistency of a region's response to a remote PWE, it has strong potential for use in future studies. For example, the STRIPES index could be used in the evaluation of numerical weather or climate models. Comparisons of maps of the STRIPES index constructed using observations to those using global climate models could help in the evaluation of these models. Similarly, comparisons of maps of the STRIPES index to maps of predictability using a forecast model could help identify regions where models are not simulating teleconnections with fidelity. Furthermore, this index could be used to help motivate the development of statistical forecast models for regions where numerical forecast models struggle to simulate observed teleconnections. The STRIPES index may also be applied to quantify seasonal differences in teleconnectivity between PWE and remote regions, or differences due to the influence of other longer-scale PWEs. For example, it has been shown that MJO teleconnections are modulated by El Niño phase (e.g., Moon et al., 2011; Henderson & Maloney, 2018) and the Quasi-Biennial Oscillation (e.g., Son et al., 2017; Mundhenk et al., 2018).

In the application of the STRIPES index to the MJO, I average using diagonal "slopes" of 4 to 7 days per phase. This decision is made to ensure that the diagonal stripes used in the calculation of the index are of MJO periodicity—the MJO is not perfectly periodic, its return time can vary between 20-90 days. However, one could conceivably choose a different slope or allow the

data to choose the slope that maximizes the variance of the one-dimensional vector of diagonal averages. For PWEs with variable periodicities, this type of analysis could, for example, be used to investigate how PWE propagation speed influences teleconnection signal strength.

The STRIPES index is related to a method devised by Zheng et al. (2018). In that study, the authors create 2D composites with intraseasonally filtered anomalies, and then compute the variance of the result to obtain an index that is qualitatively similar to STRIPES. Their method gives generally similar results to those presented here, although with some differences, particularly for precipitation. The STRIPES index differs from that presented in Zheng et al. (2018) by using unfiltered data, and by targeting propagating anomalies in the 2D composite (stripes) that are consistent with MJO periodicity through the calculation of diagonal means. The STRIPES index thus selectively amplifies signals in the data that are co-variable with the PWE in question, while the method presented in Zheng et al. (2018) attempts to do the same through the use of filtering.

2.6 Summary and Conclusions

I present the “Sensitivity to the Remote Influence of Periodic Events” (STRIPES) index to quantify the observed magnitude and consistency of a region’s response to a periodic weather event (PWE). The index was designed so that regional variations in teleconnection strength excited by remote PWEs can be quickly and easily quantified.

In the present study, the STRIPES index was applied to investigate the apparent response of 500 hPa global geopotential heights and North American surface weather to MJO forcing. Results for geopotential height show strong sensitivities in the extratropics, indicative of the MJO’s remote teleconnections. Results for surface stations indicate an observable link with the MJO over eastern North America, and parts of western North America, that is consistent with previous studies. I additionally show that this link is robust as it both covers a large geographic area and is significant even at the level of individual weather stations (i.e., no temporal or area smoothing is required to detect this link). Furthermore, I show that sensitivities to the MJO not only vary regionally, but also with variable. The magnitude of TMIN sensitivities to the MJO are somewhat weaker

than TMAX. The STRIPES index shows promise for use in future studies seeking to apply the predictive power of PWEs. For example, in the subsequent chapter, I use the STRIPES index to investigate the seasonality of MJO teleconnections over North America, which was published as part of a study also looking at the seasonality of the predictive skill of the MJO (Jenney, Nardi, et al., 2019).

Chapter 3

The Seasonality and Regionality of MJO Impacts over North America

3.1 Introduction

Forecasts of weather at subseasonal to seasonal (S2S) time scales are useful to a wide range of societal sectors (White et al., 2017). Skillful S2S forecasts have the potential to save lives and money. However, the chaotic nature of the atmosphere makes deterministic forecasts beyond about 10 days a challenge. Skill at extended lead times comes from slowly-varying systems such as the ocean, land surface, and low-frequency atmospheric phenomena such as the Madden-Julian Oscillation (MJO) and the stratospheric Quasi-Biennial Oscillation. Efforts are underway to utilize these slowly-varying weather systems to improve forecasts. While S2S forecasts remain a challenge, there is evidence that improvements to extended-range forecasts are possible (e.g., Johnson et al., 2014; Mundhenk et al., 2018; Rodney et al., 2013).

The MJO, a large eastward-propagating tropical convective system, is considered to be one of the most important sources of predictive skill at S2S time scales (Zhang, 2013). The dipole of anomalous divergence and convergence at the level of convective outflow associated with the MJO makes it a very efficient source of tropical Rossby waves (Sardeshmukh & Hoskins, 1988; Lin, 2009; Seo & Son, 2012; Seo & Lee, 2017; Tseng et al., 2019). MJO-excited Rossby waves have been linked to variability and predictability of the extratropical circulation (e.g., Black et al., 2017; Cassou, 2008; Guo et al., 2017; Henderson et al., 2016; Higgins & Mo, 1997; Kang & Tziperman, 2018; Lin, Brunet, & Fontecilla, 2010; Mori & Watanabe, 2008; Moore et al., 2010; Seo & Son, 2012; Zheng et al., 2018), precipitation (e.g., Curtis, 2017; DelSole et al., 2017; Jones et al., 2011; Lin, Brunet, & Mo, 2010; Zheng et al., 2018), atmospheric rivers (Baggett et al., 2017; Mundhenk

et al., 2018), and temperature (e.g., Barrett, 2019; Johnson et al., 2014; Lee & Grotjahn, 2019; Matsueda & Takaya, 2015; Rodney et al., 2013; Zheng et al., 2018).

The influence of the MJO on extratropical weather is best established for the boreal winter season (Stan et al., 2017). The results from winter studies do not necessarily extend to other seasons because Rossby wave generation and propagation are very sensitive to the background-state winds (Bladé & Hartmann, 1995; Henderson et al., 2017; Hoskins & Ambrizzi, 1993; Newman & Sardeshmukh, 1998; Sardeshmukh & Hoskins, 1988; Simmons et al., 1983; Ting & Sardeshmukh, 1993). In the Northern Hemisphere, stronger background winds support stationary waves with longer wavelengths, and allow a wider range of Rossby wavelengths to propagate poleward before being absorbed or reflected. In addition, the MJO's propagation changes with the seasonal cycle, exhibiting a northward component during boreal summer (e.g., B. Wang & Rui, 1990).

Better non-winter forecasts on S2S time scales can be useful to decision-makers because many high-impact extreme events such as floods and heat waves can occur during the warm season. For example, the agricultural sector is one of the largest consumers of meteorological information, and many important agricultural applications of weather forecasts occur during spring and summer (White et al., 2017).

There is increasing evidence that the MJO influences the extratropical circulation outside of boreal winter. L. Wang et al. (2013) estimate that at least 20% of extratropical intraseasonal variability over the North Pacific in summer is excited in the tropics. Moon et al. (2013) locate hot spots along the Northern Hemisphere jet stream where summer variability is linked to the MJO. The MJO has been linked with summer precipitation over Mexico (Mo, 2000) and that associated with the North American monsoon (Lorenz & Hartmann, 2006; Mo, 2000). Additionally, the state of the spring and early summer MJO has been shown to offer predictive skill for severe weather over parts of North America (Baggett et al., 2018).

Given the desire for improved forecasts of weather at S2S timescales, and their potential to save lives and money, it is important to understand more completely how the MJO affects the extratropical circulation and surface weather in seasons other than boreal winter. Studies designed

to look deeper into this question have typically relied on the use of lagged composite maps (e.g., Bond & Vecchi, 2003; Curtis & Gamble, 2016; Donald et al., 2006; Moon et al., 2013; Matsueda & Takaya, 2015; S. Zhou et al., 2012). Many such maps are needed because of the many phase and lag combinations, which ultimately restricts their utility for understanding the regionality and seasonality of MJO teleconnections over many lead times and MJO phases. Here, I utilize the STRIPES index as an alternative method to investigate the seasonality and regionality of MJO impacts on temperature over North America. This can guide the search for predictive skill at S2S timescales.

3.2 Data and Methods

3.2.1 Observed MJO impacts

Daily data from January 1980 through August 2018 is used. The position and strength of the MJO is quantified using the outgoing longwave radiation MJO Index (OMI) (Kiladis et al., 2014). This index is chosen because its definition varies smoothly with the calendar year and can thus capture the seasonality of the MJO teleconnection while also taking into account the seasonality of the MJO itself. The OMI has been shown to accurately represent the propagation of the MJO both in summer and winter (S. Wang et al., 2018). In composites, and in the calculation of the STRIPES index, only MJO days with an OMI amplitude ($\sqrt{PC_1^2 + PC_2^2}$) greater than 1.0 are considered.

Temperature data are daily maxima from the Global Historical Climatology Network-Daily database (Menne et al., 2012). Only North American stations with daily maximum temperature time series that are at least 50% complete for at least 50% of the years in the time period are used, leaving 8356 weather stations (Figure 3.1a). Data are converted to anomalies by removing the first three annual harmonics and long term mean.

The observed sensitivity of temperature to the MJO is quantified using the STRIPES index (see Chapter 2), which condenses the information contained in a lagged composite of a variable across a range of lags and phases. The STRIPES index itself does not directly communicate information about the phase-dependency of MJO teleconnections, but captures this dependency through explicit

quantification of the magnitude of the component of the lagged composite that is consistent with MJO propagation. Hence, the STRIPES index is large when the co-variability of the variable with the MJO is strong and there is consistency between MJO events. Its value can be understood as the average magnitude of the composite response of that variable conditioned on the MJO. I assume that the MJO spends between 5 and 7 days in each of the 8 phases, reorder the phases, and consider lags 0 to 42 days after each phase. For the calculation of the average STRIPES index over multiple weather stations, I first apply an area-weighting as in McKinnon et al. (2016) to construct a single time series for the region, so that areas with higher densities of weather stations are not over-weighted.

The significance of the STRIPES index is calculated using a bootstrap method with 500 samples. For each bootstrap sample, the STRIPES index is calculated using a distribution of MJO days that have the same month and day as the MJO days used in the analysis, but with a randomly sampled (with replacement) year. This allows the time of year and memory between MJO phases, which occur as sequences of consecutive days, to be retained. Significance at $\alpha < 0.10$ and $\alpha < 0.05$ are taken to be the 90th and 95th percentiles of the distribution of STRIPES indices created by the bootstrapping method.

3.3 Results

3.3.1 Observed MJO Links

Because the STRIPES index is a single number for a region or point, it is easy to plot its variations over time and space. Figure 3.1 shows the annual variation of the STRIPES index for weather-station daily maximum temperature for various North American regions (colored boxes). Each region was selected for one or more of the following reasons: the region has previously been linked with the MJO; inclusion of the region will help to create a geographically diverse set of regions that cover areas with societal importance; and/or because the weather stations within the region agree in their timing and magnitude of their sensitivity to the MJO (Figure 3.2). To investigate the seasonality of the apparent MJO teleconnections at weather stations, I calculate the

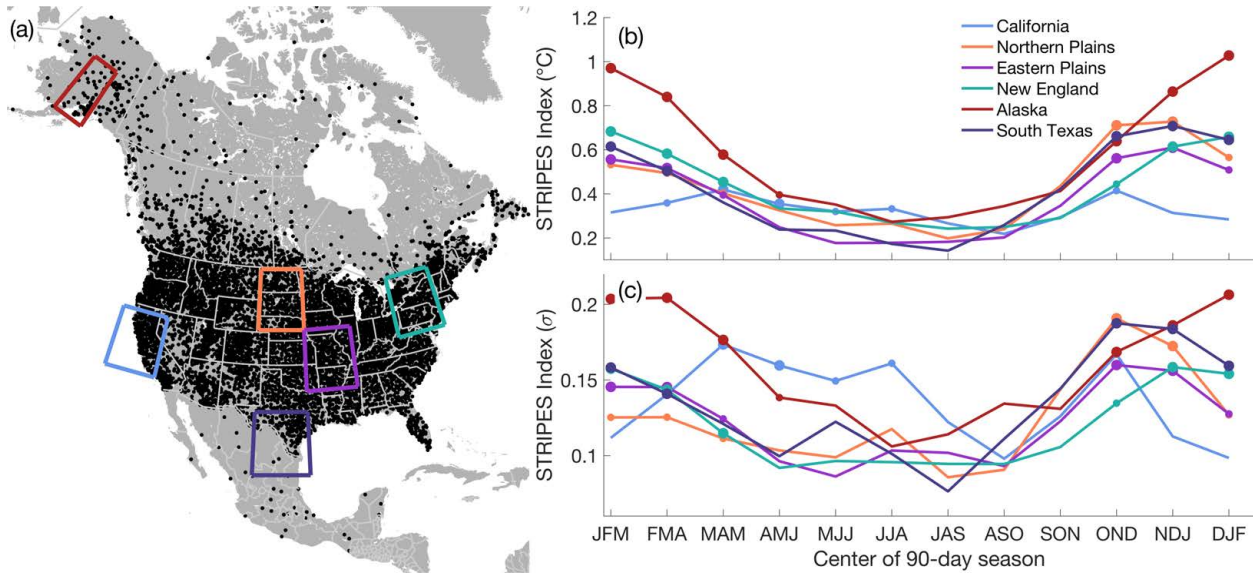


Figure 3.1: Seasonality of the MJO teleconnection for daily maximum temperature at weather stations between January 1980 and August 2018. (a) Black points show the location of weather stations that meet our data-completeness requirements (see text). Colored boxes enclose regions for which the STRIPES index is calculated. (b) The STRIPES index for each region in units of $^{\circ}\text{C}$ and (c) standard deviations. Large (small) circles indicate significance at $\alpha < 0.05$ ($\alpha < 0.10$). Seasons are indicated by the three-letter acronym of the three consecutive constituent months (e.g., January, February, March is JFM.)

STRIPES index for overlapping three-month seasons using the time series for each area-averaged region. Figure 3.1b shows that for the selected regions the average magnitude of the apparent significant winter MJO impact on temperature is between about 0.6°C and 1°C (i.e., the STRIPES index). The apparent MJO teleconnection during summer appears to be weaker for all six regions, with most regions showing STRIPES indices around 0.2°C , and not indicating any significance. This is consistent with previous results that indicate stronger MJO impacts on North American temperature in boreal winter (S. Zhou et al., 2012).

Figure 3.1b shows that MJO teleconnections to the extratropics are strongest in the winter (DJF) for Alaska and New England. This is consistent with previous work; these are both centers of action of the Pacific-North America pattern, a quasi-stationary feature of the local large-scale circulation that is tied to the MJO (Goss & Feldstein, 2015; Mori & Watanabe, 2008; Seo & Lee, 2017), and most active during the winter months (Barnston & Livezey, 1987). However, other regions show significant peaks in MJO co-variability outside of DJF. Temperature over the northern plains, eastern plains, and south Texas regions display peaks in MJO co-variability during

the three-month seasons centered on November and December (OND, NDJ), 30-60 days prior to DJF. The California region has a weaker but significant peak during OND, with comparable peaks in late spring and early summer.

Figure 3.1c shows the STRIPES index normalized so that it is in units of standard deviations, σ . Each region and season is standardized independently. This standardized STRIPES index shows the magnitude of the co-variability of station-based surface temperatures with the MJO relative to the local seasonal variance of temperature, which is relatively high (low) over land in the extratropical winter (summer). From here on, I discuss the STRIPES index in “standardized” units of σ , because the focus is on the seasonality and regionality of the MJO teleconnection from a weather prediction perspective—a 1 °C departure from climatology is less common in seasons and regions where the variability of temperature is small. There is little change in the timing of maxima and minima of the STRIPES index from °C to σ units. Although there are slight (not more than one month) shifts in the exact three-month season when the peak MJO signal occurs for some regions, the general shape of the seasonality of the MJO signal for each region is preserved. For example, the northern plains maintains the strongest signal in late fall, with a minimum in summer, despite the peak signal moving from the November through January season to the October through December season.

However, non-DJF peaks for some regions now appear to scale with other regions’ winter peaks. In σ units, the magnitude of the influence of the MJO on the three regions for which impacts peak in November/December is comparable to that for winter over Alaska and New England, which are two regions understood to be strongly influenced by the MJO (Zheng et al., 2018; S. Zhou et al., 2012). The seasonality of the strength of MJO impacts on temperature for the California region are particularly interesting. While spring and summer peaks are apparent in Figure 3.1b, they appear small relative to the winter peaks of Alaska because of the relatively small local temperature variance over this region in summer. However, Figure 3.1c shows that in σ units California’s spring and summer sensitivity of temperature to the MJO scales with that for fall and winter in other regions. In earlier work, the MJO has been shown to be linked with summer heat waves over the

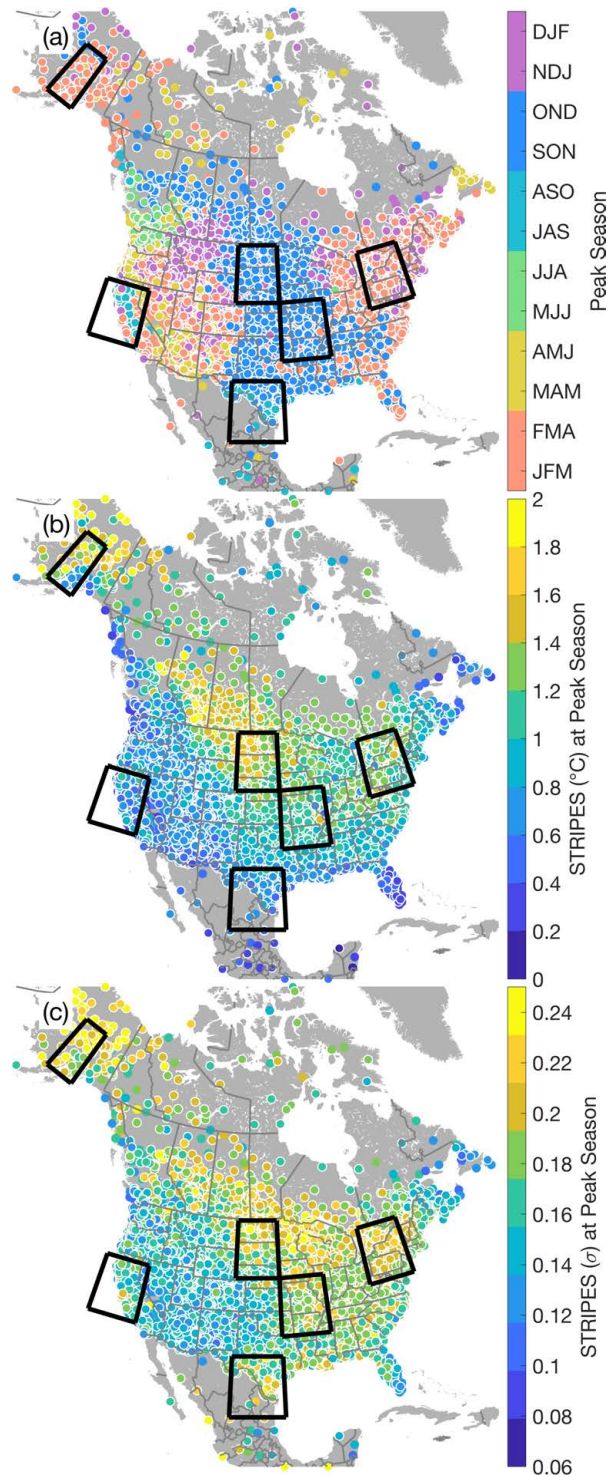


Figure 3.2: (a) Season of the peak significant value of the STRIPES index (in standard deviations, σ) for daily temperature maxima at weather stations and (b) the magnitude of that maximum in $^{\circ}\text{C}$ and (c) σ . Regions highlighted in Figure 3.1 are enclosed with black boxes. Only weather stations with significant peaks at $\alpha < 0.10$ are plotted. Weather stations whose peaks are significant at $\alpha < 0.05$ are enclosed with white circles.

California central valley (Lee & Grotjahn, 2019). Here I show that the peak influence of the MJO on daily temperature maxima over this region occurs during spring and summer.

To investigate the seasonal sensitivity of local temperature—that is, temperature at points, rather than the mean temperature over a large region—to the MJO, I apply the STRIPES index to individual weather stations for each overlapping season. Figure 3.2a shows the season where the peak STRIPES index occurs (in σ) for daily temperature maxima. Only weather stations with a significant (at $\alpha < 0.10$) STRIPES index during the peak season are plotted, and weather stations for which $\alpha < 0.05$ are marked by white circles. Despite some inhomogeneity, there is generally good spatial agreement in the peak sensitivity of temperature to the MJO, with coherent regions emerging. Much of Alaska and New England display the strongest MJO signal during the latter half of boreal winter. A large region over the Great Plains experiences peak MJO impacts during fall. There are even some areas with summer peaks, such as northern Washington and southern British Columbia, the California central valley, and the southern tip of Texas.

At this station-based spatial scale, Alaska and eastern North America (excluding the easternmost portion of Canada) show the strongest sensitivities (in σ , Figure 3.2c) of temperature to the MJO, consistent with previous work (Baxter et al., 2014; Matsueda & Takaya, 2015; Schreck et al., 2013; Johnson et al., 2014; Zheng et al., 2018; S. Zhou et al., 2012). These regions display their peaks in fall and winter.

3.4 Discussion and Conclusions

The influence of the MJO on extratropical weather is best established for the boreal winter season (Stan et al., 2017). However, a growing body of literature demonstrates that the MJO influences weather in other seasons (Baggett et al., 2018; Curtis, 2017; Lorenz & Hartmann, 2006; Mo, 2000; Moon et al., 2013; L. Wang et al., 2013). Here I show that, for near-surface air temperature over North America, the MJO's impacts on observed variability displays substantial seasonality and regionality.

I have also shown sensitivity of the apparent MJO signal in surface air temperature to standardization by local and seasonal variance. Standardization does not strongly influence the timing of peak MJO impacts. Many previous studies quantify MJO impacts through composite methods in which standardization is not used. Because of the strong cold-season variability of extratropical geopotential heights and temperatures, composites made for winter will generally have stronger magnitudes than those made for summer. However, my interest in the MJO's impacts on North American temperature are rooted in a desire to improve forecasts on subseasonal-to-seasonal leads. A 1°C departure in temperature is more abnormal and may have a higher impact over a region and/or during a season for which the temperature variance is very low. In other words, a 1°C departure from average over a region or during a season where the standard deviation of temperature is very small is more extreme than a similar departure of temperature for a region or season where the standard deviation of temperature may be multiple °C, and for which such a temperature anomaly is more common. I am interested in departures of the temperature from what is considered normal for that season or region. This allows seasons and regions to be compared.

Chapter 4

Climate change and the tropical mean circulation

The mean tropical circulation is closely coupled to convection. Mean rising motion occurs in relatively warm and moist regions, in association with active deep cumulus convection. This upward motion is balanced by slow, radiatively driven subsidence that occurs in drier regions, where cumulus convection is suppressed.

For reasons discussed below, both the tropical mean circulation and the low-level convective mass flux are expected to weaken in a future, warmer climate (Betts & Ridgway, 1989; Chou & Chen, 2010; Knutson & Manabe, 1995; Held & Soden, 2006; Schneider et al., 2010; Seager et al., 2010; Vecchi & Soden, 2007). The mean circulation is the net vertical mass flux over an area large enough to contain many convective clouds, and is the sum of the mass fluxes of narrow convective updrafts and downdrafts and the vertical mass flux of their broad, quiescent environment.

Betts and Ridgway (1989) were the first to suggest that the tropical mean circulation would weaken with warming. Using a simple model of the tropical boundary layer, they found that the subsidence required for thermodynamic equilibrium weakened as sea surface temperatures warmed. Their conclusions were supported by the results of Knutson and Manabe (1995), who found that a global circulation model (GCM) simulated a weakening of the mean circulation with warming.

The response of the mean circulation can be understood in terms of the area-averaged dry static energy budget:

$$\frac{\partial \bar{s}}{\partial t} = -\overline{\mathbf{v}_h \cdot \nabla s} - \bar{w} \frac{\partial \bar{s}}{\partial z} + \overline{Q_R} + \overline{Q_c}. \quad (4.1)$$

Here s is dry static energy, \mathbf{v}_h is the horizontal wind vector, w is the vertical velocity, Q_R is the radiative heating rate, Q_c is the non-radiative heating rate due to cloud processes and turbulence,

and an overbar represents an area average. In a dry-statically stable atmosphere, $\partial s/\partial z > 0$. In the tropics, and for time scales longer than a few hours or a day at most, equation (4.1) can be approximated by the “weak temperature gradient” (WTG) balance (Charney, 1963; Sobel & Bretherton, 2000; Sobel et al., 2001):

$$\bar{w} \frac{\partial \bar{s}}{\partial z} = \bar{Q}_R + \bar{Q}_c. \quad (4.2)$$

In the absence of non-radiative heating (i.e., for $\bar{Q}_c = 0$), (4.2) reduces to a balance between radiative cooling ($\bar{Q}_R < 0$) and the warming due to downward advection of dry static energy (i.e., $\bar{w} < 0$). Many studies have shown that in a warming climate the tropical static stability increases, roughly following the more stable moist adiabat associated with warmer surface temperatures. The fractional change in the static stability is larger than the fractional change in the radiative cooling rate, so that (4.2) implies slower subsidence in non-convective regions.

Held and Soden (2006) proposed that the globally averaged convective mass flux will also decrease with warming. This is the vertical mass flux associated with convective updrafts (and downdrafts). The mass flux associated with convective updrafts is given by

$$M_u = \rho \sigma_u w_u, \quad (4.3)$$

where ρ is the density of the air, σ_u is the fractional area covered by the convective updrafts, and w_u is the vertical velocity of the convective updrafts. A similar formula gives M_d , the mass flux associated with convective downdrafts. Held and Soden (2006) expressed the globally averaged moisture budget in the form

$$P = (M_u)_B q_B. \quad (4.4)$$

Here P is the surface precipitation rate, $(M_u)_B$ is the lower-tropospheric value of M_u , and q_B is the lower-tropospheric water vapor mixing ratio. Changes in the globally averaged latent heat release associated with precipitation are mainly balanced by changes in atmospheric radiative cooling (e.g., Riehl & Malkus, 1958). Allen and Ingram (2002) argued that, as the climate warms, the fractional increase in P will be much smaller than the fractional change of q_B , which increases following Clausius-Clapeyron scaling. Based on this idea, Held and Soden (2006) concluded from (4.4) that M_B must decrease with warming. Vecchi and Soden (2007) provided support for this conclusion, based on an analysis of results from a suite of GCMs.

In summary, energy balance suggests that the subsidence *velocity* will weaken with warming, and moisture balance suggests that the lower-tropospheric convective mass flux will also weaken with warming. Caution is needed before concluding that these changes imply a weakening of the circulation as measured by the total upward (or downward) mass flux. For example, slower subsidence over a broader region can give the same downward mass flux. In fact, an expansion of subsiding regions and a contraction of ascending regions have been observed in the historical record and produced in simulations of warming (e.g., Byrne & Schneider, 2016a, 2016b; Byrne et al., 2018; Hu & Fu, 2007; Lau & Kim, 2015; J. Lu et al., 2007; Su et al., 2017, 2019; Wodzicki & Rapp, 2016).

Additionally, although the mass flux of the large-scale mean circulation is expected to be upward when and where the mass flux of deep convective clouds is upward, there are important differences between the two (Arakawa & Schubert, 1974; Betts, 1998). The mean mass flux includes partially cancelling contributions from much stronger local convective updrafts and downdrafts, as well as vertical motions in the broad environment between the convective drafts. For example, Schneider et al. (2010) estimated that the rate at which mass ascends in convective updrafts may be up to five times larger than the mean upward motion, simply because of compensating downward motions in the same region. A more detailed discussion is given later.

For the reasons outlined above, the current paradigm of warming-induced weakening of both the tropical mean circulation and the tropical convective mass flux needs further study, in part

because a weakening of the tropical circulation and/or convective mass flux may contribute to a weakening of teleconnections between the tropics and middle latitudes (Bui & Maloney, 2018; ?, ?; Wolding et al., 2017). In this chapter I use idealized simulations of global radiative-convective equilibrium (RCE) to investigate warming-induced changes to the mean circulation and convective mass flux.

4.1 Methods

4.1.1 Model

Simulations of the future climate are sensitive to convective parameterizations (e.g., Maher et al., 2018). Models participating in the Coupled Model Intercomparison Project Phase 5 vary widely in their projections of the strength of the mean tropical circulation (Byrne et al., 2018), mostly due to differences in convective parameterizations between the models (Schiro et al., 2019). The resulting uncertainties can be avoided by using global convection-resolving models (CRMs; e.g., Stevens et al., 2019), but for now the high computational cost of such models limits their use in global climate change simulations. Superparameterization offers an intermediate option, in which the conventional parameterizations of cloud and boundary-layer processes are replaced by a simplified CRM embedded within each GCM grid cell (Grabowski, 2001; Khairoutdinov & Randall, 2001; Khairoutdinov et al., 2005; Randall et al., 2003). The CRM explicitly simulates the cloud-scale dynamics by solving the equation of motion. Cloud microphysics, radiative transfer, and turbulent mixing are parameterized on the CRM's fine grid. Despite the two-dimensionality of the embedded CRMs, which is needed to reduce the high computational cost of simulations, superparameterization enables more realistic simulations of a number of convectively coupled global processes (summarized by Randall et al., 2016). Key for the present study is that superparameterization makes it possible to directly diagnose changes in the convective mass flux and heating associated with cloud systems that are explicitly simulated by the CRM.

Here I present results from a superparameterized (SP) version of the Community Atmosphere Model 4 (CAM4), using the finite-volume dynamical core and a $0.9^\circ \times 1.25^\circ$ horizontal grid. Each

GCM grid column hosts an embedded two-dimensional CRM, which has a horizontal grid spacing of 4 km with 32 columns. The CRMs share the bottom 24 of CAM4’s 26 layers. Microphysics are computed by the CRM using a single-moment microphysics scheme, described in detail by Khairoutdinov and Randall (2003). For more details on SPCAM4 see Kooperman et al. (2016).

Following the experimental design of the RCE model intercomparison project (RCEMIP; Wing et al., 2018), RCE is simulated using uniform solar insolation and uniform sea surface temperatures (SSTs) on a non-rotating planet. Using SSTs of 295 K, 300 K, and 305 K, the model was run for three simulated years. These simulations are among those analyzed by Wing et al. (2020). The present results are based on analysis of hourly and daily mean output for a 15-day extension at the end of year 3. Data were saved on the native CAM4 $0.9^\circ \times 1.25^\circ$ horizontal grid, and for 26 hybrid-sigma model levels, with hybrid sigma vertical coordinate σ_h .

4.1.2 Diagnostics

For both the RCE and earth simulations, I make use of a diagnostic quantity computed by the CRM and saved on the GCM grid. This is the non-radiative temperature tendency due to the embedded CRM (model variable name “SPDT”), horizontally averaged over the CRM’s grid.

The model also provides convective mass flux diagnostics, which are computed using vertical velocities on the CRM’s grid. The mass fluxes are computed on each CRM time step, then time-averaged for output at a specified interval. Following (4.3), the convective mass flux is the sum of the air density times the vertical velocity times the fractional area over CRM grid cells for which the average of the vertical velocities at the model level top and bottom is greater than (for updrafts) or less than (for downdrafts) a specified vertical velocity threshold. CRM cells with weaker vertical velocities do not contribute to the average. The specified threshold vertical velocity is used to distinguish convection from non-convective processes, such as turbulence and gravity waves.

The threshold is of course somewhat arbitrary. To explore the sensitivity to the threshold, and also to obtain some information about the range of convective intensity, I computed convective mass fluxes using hourly vertical velocities in the same way as described above, but with three

different vertical-velocity thresholds (0.5 m s^{-1} , 1 m s^{-1} , and 2 m s^{-1}). A test comparing the global mean convective mass fluxes computed using hourly versus instantaneous vertical velocities, both using the 2 m s^{-1} threshold, showed good agreement. In the plots shown later, I use the lowest threshold, 0.5 m s^{-1} , to diagnose the total convective mass flux. I categorize mass fluxes using vertical velocities between 0.5 m s^{-1} and 1 m s^{-1} as “weak” convection, between 1 m s^{-1} and 2 m s^{-1} as “moderate” convection, and greater than 2 m s^{-1} as “intense” convection.

4.2 Results

4.2.1 Mean circulation

The global-mean precipitation rate increases from 2.6 mm day^{-1} in the 295 K RCE simulation to 3.2 mm day^{-1} (a $4\% \text{ K}^{-1}$ increase) and 3.8 mm day^{-1} ($3.5\% \text{ K}^{-1}$) in the 300 K and 305 simulations, respectively. As expected for a boundary layer that is warming but maintaining a roughly constant relative humidity, the simulated increase in the water vapor mixing ratio of the lowest model level is about $6.8 \% \text{ K}^{-1}$.

Figure 4.1 shows the domain-mean dry static stability profiles for these simulations. The dry static stability increases with warming, particularly at upper-levels, as expected for a nearly moist-adiabatic lapse rate adjusting to warmer surface temperatures.

As discussed earlier, a weakening of the mean subsidence velocity is an expected response to warming. However, this does not directly imply a weakening of the mean circulation as measured by the rate that mass circulates. In order to say something about potential changes to the mean circulation with warming, it is necessary to take into account any changes in the fractional areas covered by mean ascent and descent.

I define regions of ascent and descent at each level based on their daily mean vertical velocity. Mass balance requires that the mass fluxes of the ascending and descending regions are equal. This can be written as

$$\overline{M_{up}} = -\overline{M_{dn}} \equiv \overline{M}, \quad (4.5)$$

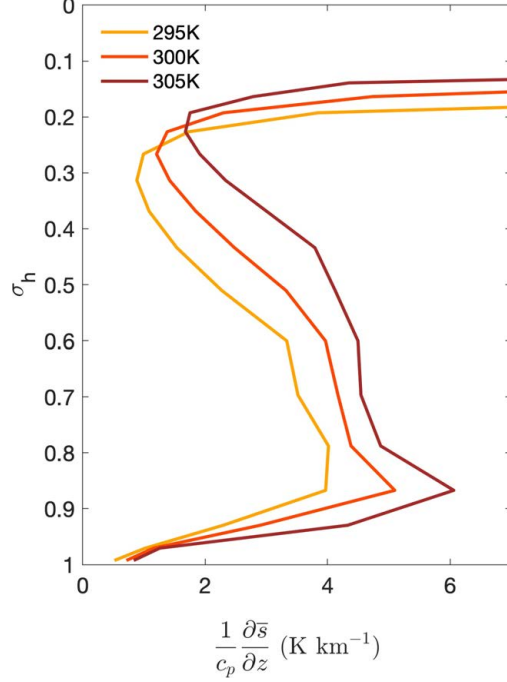


Figure 4.1: Mean static stability profiles for simulations. The vertical axis is the hybrid-sigma vertical coordinate, σ_h . We have divided by c_p , the specific heat of air at constant pressure, so the units are K km^{-1} .

or as

$$\overline{w_{up}} \rho_{up} \alpha_{up} = -\overline{w_{dn}} \rho_{dn} \alpha_{dn}. \quad (4.6)$$

In these equations, the subscripts “up” and “dn” refer to regions of ascent ($\overline{w} > 0$) and descent ($\overline{w} < 0$), respectively. In (4.5), I have taken advantage of the fact that $\overline{M_{up}} = -\overline{M_{dn}}$ to define the symbol \overline{M} (no subscript), which can be called the mass flux of the “overturning circulation.” For our simulations of global RCE without rotation, weak horizontal temperature gradients allow me to apply equation (4.2) to substitute for the vertical velocities in equation (4.5) in terms of the area-averaged heating rates. Assuming that $\rho_{up} \approx \rho_{dn}$, and making the substitution $\alpha_{dn} = 1 - \alpha_{up}$, I find that

$$\alpha_{up} \approx \frac{1}{1 - \gamma \frac{\overline{Q_{up}}}{\overline{Q_{dn}}}}, \quad (4.7)$$

where I define

$$\gamma \equiv \frac{(\partial \bar{s} / \partial z)_{dn}}{(\partial \bar{s} / \partial z)_{up}}, \quad (4.8)$$

and \bar{Q} is the mean total heating (i.e., $\bar{Q}_R + \bar{Q}_c$). Neglecting the effects of differences in the dry static stability between the ascending and descending regions (i.e., for $\gamma \approx 1$), equation (4.7) says that the fractional area covered by mean ascent decreases as the ratio of mean total heating between the ascending and descending regions increases. The ratio $\bar{Q}_{up} / \bar{Q}_{dn}$ is always ≤ 0 . In fact, I can use equation (4.7) to show that for, $\gamma = 1$, the area-averaged heating rate (across both ascending and descending regions) is zero. When the mean (absolute) heating rates of the two regions are equal, $\bar{Q}_{up} = \bar{Q}_{dn}$ and (4.7) gives $\alpha_{up} = 0.5$. Larger heating rates in the ascending region, relative to the cooling rates in the descending region, imply stronger rising vertical velocities in the ascending region than sinking vertical velocities in the descending region (equation 4.2). The descending region must therefore cover a larger fractional area than the ascending region. This is what I see in the simulations. Figure 4.2a shows the difference between α_{up} calculated using equation (4.7) and the true α_{up} . Throughout the mid-troposphere, roughly between levels $\sigma_h = 0.7$ to $\sigma_h = 0.3$, the approximate α_{up} given by equation (4.7) is nearly equal to the true α_{up} , shown in Figure 4.2b. That is, between these levels, the error of the approximation is small. The approximation slightly overestimates α_{up} between $\sigma_h = 0.9$ and $\sigma_h = 0.7$, and is very poor in the boundary layer and stratosphere. At low levels, while some of the disagreement between the approximation and α_{up} may be due to differences in density between the humid ascending and dry descending regions, it is more likely driven by the weaker applicability of the WTG approximation at those levels.

Figure 4.2c shows the percentile of the column relative humidity (CRH; column precipitable water divided by the precipitable water of a saturated column with the same temperature profile) where these regions tend to be located. Regions of ascent in the upper troposphere have CRH values larger than about 0.75, while ascending air can occur in the lower troposphere even for CRH values less than 0.5.

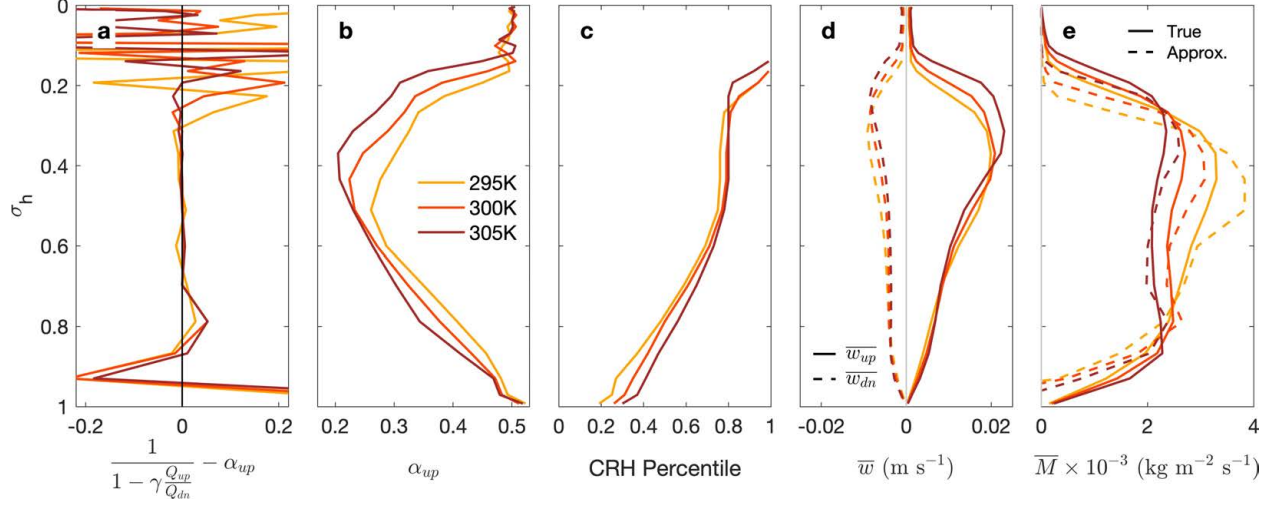


Figure 4.2: a, The difference between the approximate fractional ascent area, α_{up} , given by equation (4.7) and the true α_{up} . b, α_{up} . c, The column relative humidity (CRH) percentile that separates regions of mean ascent (right of the line) from regions of mean descent (left of the line). d, The mean vertical velocity, \bar{w} , for the ascending (solid line) and descending (dashed line) regions. e, The true (solid) and approximated, using equation (4.9) (dashed) mass flux of the mean circulation, \bar{M} .

Figure 4.2d shows the mean vertical velocity in the ascending and descending regions. Mean rising motions are stronger than sinking motions throughout most of the troposphere. Again, ignoring the small differences in static stability between the ascending and descending regions, 4.2d together with equation (4.2) implies that the heating in the ascending region is stronger than the cooling in the descending region. This is reflected in the values of α_{up} , which are less than 0.5 at almost all levels.

In addition to a weakening of the mean subsidence velocity, I find that the fractional area covered by the ascending region decreases with SST. This decrease is stronger in the upper troposphere, above $\sigma_h = 0.5$. At those same levels the fractional area covered by subsidence increases with SST. Figure 4.2e shows that the overturning mass flux (which is equal and opposite between the ascending and descending regions) weakens with warming throughout most of the troposphere (between about $\sigma_h = 0.9$ and $\sigma_h = 0.25$). This is consistent with previous work, and reflects the fact that both the fractional area of the ascending region and the mean vertical velocity in the ascending region decrease with increasing SST.

Using the approximation for α_{up} with equation (4.2), it is possible to approximate the strength of the overturning circulation by

$$\overline{M} \approx \frac{\rho}{(\partial \overline{s} / \partial z)_{up}} \left(\frac{\overline{Q}_{up} \overline{Q}_{dn}}{\overline{Q}_{dn} - \overline{Q}_{up}} \right). \quad (4.9)$$

The approximate values are shown as the dashed line in Figure 4.2e. At most levels, the approximation accurately diagnoses the vertical profile of \overline{M} and its decrease with SST, although there are some larger errors in the upper troposphere (between $\sigma_h = 0.6$ and $\sigma_h = 0.3$). Equation (4.9) directly shows how the strength of the mean circulation is inversely proportional to the dry static stability in the ascending region. For $\gamma \approx 1$, this means that the strength of the mean circulation is inversely proportional to the mean tropical dry static stability. Equation (4.9) shows that increases in \overline{M} may be possible given larger fractional increases in the term, $\frac{\overline{Q}_{up} \overline{Q}_{dn}}{\overline{Q}_{dn} - \overline{Q}_{up}}$, than in dry static stability.

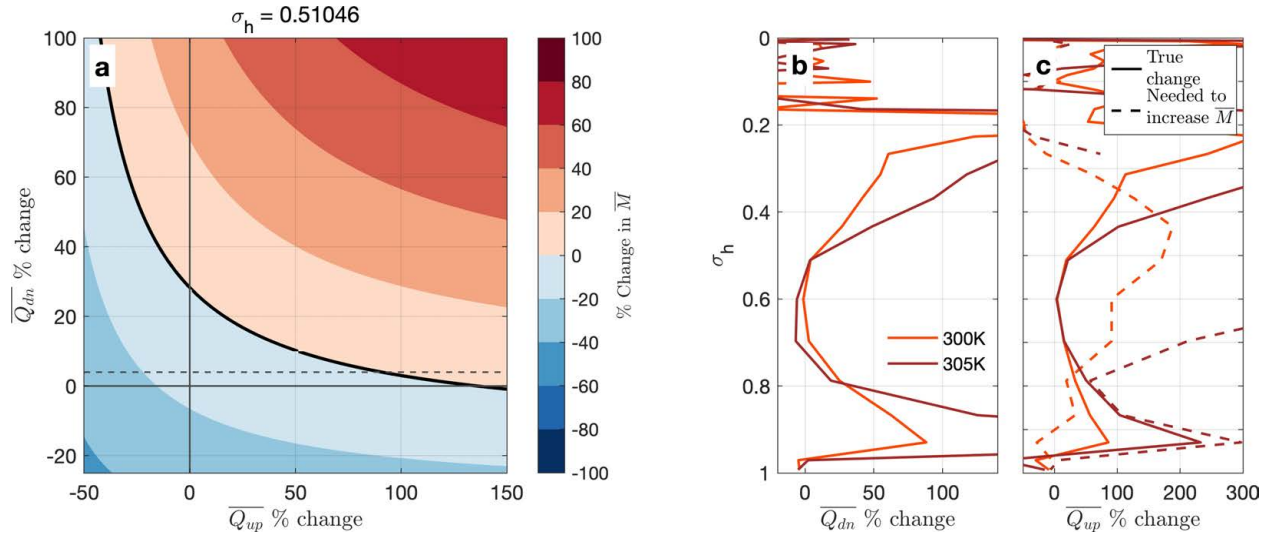


Figure 4.3: a, At $\sigma_h = 0.51$, the percent change in the strength of the mean circulation, \overline{M} , that results from prescribed fractional changes in \overline{Q}_{up} and \overline{Q}_{dn} of the 295 K simulation, given the change in the dry static stability between the 295 K and 300 K simulations. The dashed line shows the percent change in \overline{Q}_{dn} between the 295 K and 300 K simulations. b, The simulated percent change in \overline{Q}_{dn} between the 295 K and 300 K simulations (orange) and between the 300 K and 305 K simulations (brown). c, The simulated percent change in \overline{Q}_{up} (solid), and the percent change in \overline{Q}_{up} needed to strengthen \overline{M} (dashed).

It is possible to use equation (4.9) to explore the magnitude of changes in $\overline{Q_{up}}$ and $\overline{Q_{dn}}$ required to strengthen \overline{M} . Figure 4.3a shows, for $\sigma_h = 0.51$, the percent change in \overline{M} that results from prescribed fractional changes in the $\overline{Q_{up}}$ and $\overline{Q_{dn}}$ of the 295 K simulation, given the change in the dry static stability between the 295 K and 300 K simulations. In the descending region, a positive change indicates an intensification of the cooling. I include lines showing the zero percent change in heating. At their intersection, between the 295 K and 300 K simulations, \overline{M} would weaken due to the increased dry static stability alone. The horizontal dashed line shows the simulated percent change of $\overline{Q_{dn}}$ between 295 K and 300 K. Given the simulated strengthening of cooling in the descending region ($\approx +4\%$ between the 295 K and 300 K simulations) at this level, an increase in the strength of the circulation would start to occur around a doubling of the heating in the ascending region.

Figure 4.3b shows the simulated percent change in $\overline{Q_{dn}}$ between the 295 K and 300 K simulations (orange line) and between the 295 K and 305 K simulations (brown line) at each model level. Panel c of the same figure shows the simulated change in $\overline{Q_{up}}$ (solid lines) and the change in $\overline{Q_{up}}$ that would be required to get a strengthening of \overline{M} at that level, given the simulated changes in $\overline{Q_{dn}}$ and dry static stability (dashed line). Throughout the mid-troposphere (between $\sigma_h = 0.8$ and about $\sigma_h = 0.4$), the simulated increase in $\overline{Q_{up}}$ is smaller than the change in $\overline{Q_{up}}$ needed to strengthen the mean circulation. Between the 295 K and 300 K simulations, and for σ_h in the range 0.95 to 0.8, the opposite occurs: the increase in $\overline{Q_{up}}$ exceeds that needed to strengthen \overline{M} . This is consistent with the pattern of \overline{M} change that is simulated by the numerical model (see the solid curves in Figure 4.2e).

In the quiescent descending region, mid-tropospheric changes in cooling with surface warming are dominated by small increases in radiative cooling. As the surface warms, the fractional rate of increase in radiative cooling is smaller than that of the dry static stability. Increases in the strength of the mean circulation would be possible only with very large and implausible increases in heating in the ascending region. This is another way of understanding why the overturning circulation weakens with warming.

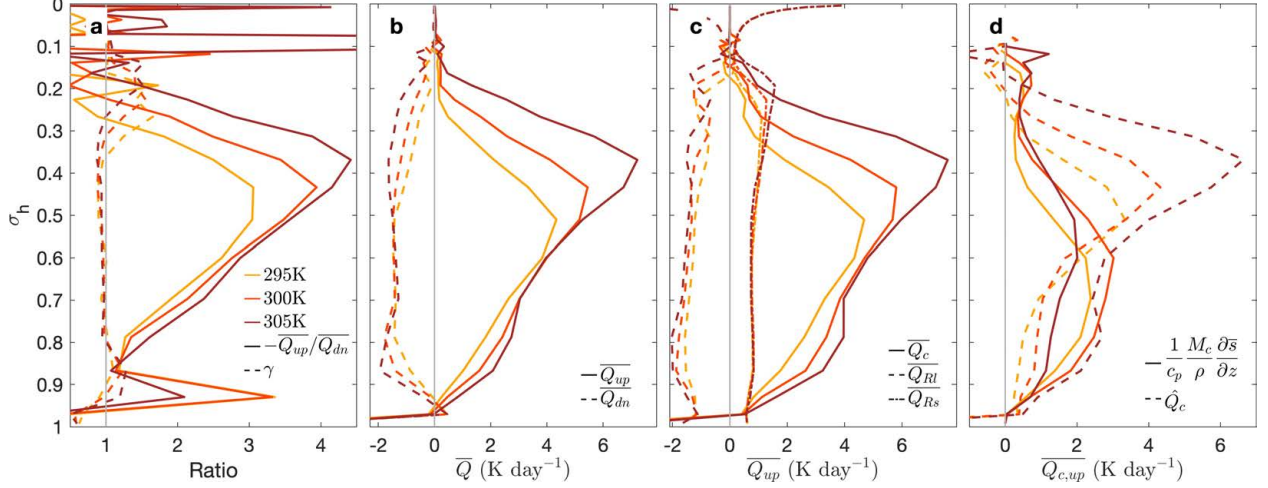


Figure 4.4: a, Minus the ratio of total heating between the ascending and descending regions (solid), and γ from equation (4.7). b, Total heating for the ascending (solid) and descending (dashed) regions. c, For the ascending region only, non-radiative (solid), longwave radiative (dashed), and shortwave radiative (dot-dashed) heating. d, For the ascending region only, heating associated with the convective mass flux ($\frac{1}{c_p} \frac{M_c}{\rho} \frac{\partial \bar{s}}{\partial z}$; solid) and stratiform heating ($\overline{Q_c}$; dashed).

Equation (4.7) can be used to gain insight into the physical processes involved with the decrease of α_{up} with increasing SST. Figure 4.4a shows γ and $-\overline{Q_{up}}/\overline{Q_{dn}}$. Throughout most of the troposphere ($\sigma = 0.8$ through $\sigma = 0.4$), $\gamma \approx 1$ and is not sensitive to the SST. From Figure 4.4a, increases in $-\overline{Q_{up}}/\overline{Q_{dn}}$ are associated with the decrease in α_{up} with SST. Figure 4.4b shows $\overline{Q_{up}}$ and $\overline{Q_{dn}}$ for each SST. In the descending region, cooling intensifies as the SST increases, throughout most of the column. This is due to increased longwave emission to space from a warmer, wetter atmosphere (e.g., Pendergrass & Hartmann, 2014). With no change in $\overline{Q_{up}}$, the stronger radiative cooling rate in the descending region would lead to an *increase* in α_{up} . But what is actually simulated is a decrease in α_{up} , because the mean heating rate in the ascending region is also intensifying, and at a faster rate than the cooling over the descending region (i.e., $-\overline{Q_{up}}/\overline{Q_{dn}}$ increases). This provides support for the suggestion of Schiro et al. (2019) that changes to convection in the ascending region are closely linked to changes in ascent area with warming.

Figure 4.4c shows the contributions to $\overline{Q_{up}}$ from both non-radiative processes ($\overline{Q_c}$), and radiation. The radiative portion is further subdivided into its longwave $\overline{Q_{RL}}$ and shortwave $\overline{Q_{RS}}$ parts. Longwave cooling intensifies in the ascending region (just as it does in the descending region), but

there is very little change in shortwave heating of the ascending region. The main message of panel c is that the increases in $\overline{Q_{up}}$ with SST in the ascending region are due to increases in non-radiative heating.

For a GCM grid cell, the mass flux of the mean circulation, \overline{M} , can be written as the sum of the net convective mass flux M_c and the “environmental” mass flux \widetilde{M} (Arakawa & Schubert, 1974):

$$\overline{M} = M_c + \widetilde{M}. \quad (4.10)$$

The environmental mass flux is associated with weak vertical motion in the broad regions between the convective updrafts and downdrafts. It is typically but not always downward. Eq. (4.10) shows that when convection is not active the mean mass flux is equal to the environmental mass flux; without convection, the domain is “all environment.”

For averages over areas large enough so that the fractional area occupied by convective updrafts is $\ll 1$ (such as a GCM grid cell), $\overline{Q_c}$ may be written as

$$\overline{Q_c} = \frac{M_c}{\rho} \frac{\partial \overline{s}}{\partial z} + L\widetilde{C} + \overline{D}(s_c - \overline{s}) + \overline{Q_{turb}}, \quad (4.11)$$

where $\frac{M_c}{\rho} \frac{\partial \overline{s}}{\partial z}$ is the warming due to the net convective mass flux, L is the latent heat of condensation and/or freezing, \widetilde{C} is the environmental condensation rate, \overline{D} is the detrainment mass flux, and $\overline{Q_{turb}}$ is the dry static energy transport due to turbulence (Arakawa & Schubert, 1974). It is possible to isolate the (non-radiative) cloud and turbulent heating apart from (i.e., not including) the contribution from $\frac{M_c}{\rho} \frac{\partial \overline{s}}{\partial z}$ using Equation (4.11) as

$$\widehat{Q_c} = \overline{Q_c} - \frac{M_c}{\rho} \frac{\partial \overline{s}}{\partial z}, \quad (4.12)$$

where

$$\widehat{Q}_c \equiv L\tilde{C} + \overline{D}(s_c - \bar{s}) + \overline{Q_{turb}}. \quad (4.13)$$

I use (4.12) to diagnose \widehat{Q}_c from the model output. Eq.(4.13) shows that contributions to \widehat{Q}_c come from environmental (non-convective) condensation $L\tilde{C}$, convective detrainment of dry static energy $\overline{D}(s_c - \bar{s})$, and turbulent transport of dry static energy, but for simplicity I refer to \widehat{Q}_c as the “stratiform heating.” A large fraction of \widehat{Q}_c comes from phase changes that occur outside of convective updrafts. Houze (1977) used radar data with other observations to show that such stratiform condensation is a major component of the heating in tropical convective systems. It is expected that $L\tilde{C} > 0$ where there is environmental rising motion in near-saturated environments (e.g., in stratiform anvil clouds), and $L\tilde{C} < 0$ where condensed water/ice is evaporating/melting as it interacts with an unsaturated portion of the environment.

Figure 4.4d shows the non-radiative heating, $\overline{Q_{c,up}}$, in the ascending region. The solid curves show $\frac{M_c}{\rho} \frac{\partial \bar{s}}{\partial z}$ and the dashed curves show \widehat{Q}_c . The increase in \widehat{Q}_c with SST is roughly monotonic, except between the 295 K and 300 K simulations where a small decrease between $\sigma_h = 0.7$ and $\sigma_h = 0.55$ may be due to the deepening of the troposphere. Interestingly, below $\sigma = 0.4$ the change in $\frac{M_c}{\rho} \frac{\partial \bar{s}}{\partial z}$ with SST is not monotonic. For the 295 K and 300 K simulations, heating associated with M_c is larger than \widehat{Q}_c below $\sigma_h = 0.6$. This is reversed in the 305 K simulation, for which \widehat{Q}_c larger than $\frac{M_c}{\rho} \frac{\partial \bar{s}}{\partial z}$ throughout the troposphere. Above $\sigma_h = 0.5$ for all simulations, and throughout the troposphere for the 305 K simulation, most of the increase in the total \overline{Q}_c of ascending regions comes from an increase in \widehat{Q}_c with SST. Between the 295 K and 300 K simulations, the increase in $\frac{M_c}{\rho} \frac{\partial \bar{s}}{\partial z}$ roughly equals that of \widehat{Q}_c .

4.2.2 Stratiform heating

What accounts for the large increase of \widehat{Q}_c with warming in the ascending regions? In the upper troposphere, the increase is directly related to the decrease in the fractional area of the ascending region with warming. Through its contribution to the increase in $\overline{Q_{up}}$, it plays a role in determining

the response of the mean circulation to warming. That is, increases in \widehat{Q}_c in the ascending region with SST keep the mean circulation from weakening as much as it would given no change in heating in the ascending region. In places where \widetilde{M} is upwards the environmental latent heating, $L\widetilde{C}$, can be written in terms of the advection of environmental moisture by \widetilde{M} as,

$$L\widetilde{C} \approx -L\frac{\widetilde{M}}{\rho}\frac{\partial\widetilde{q}}{\partial z}, \quad (\widetilde{M} > 0), \quad (4.14)$$

where \widetilde{q} is the water vapor mixing ratio of the environment. Equation (4.14) can be used to estimate the fraction of \widehat{Q}_c due to environmental condensation. The dashed lines in Figure 4.5 are the heating from $-L\frac{\widetilde{M}}{\rho}\frac{\partial\widetilde{q}}{\partial z}$ in ascending regions only. I compute this term for grid cells where \widetilde{M} is upwards, and then multiply the result by the fraction of the ascending region where $\widetilde{M} > 0$. I use the grid cell mean water vapor mixing ratio, \bar{q} , rather than the environmental \widetilde{q} , and account for the ice phase using the temperature-dependent partitioning between the liquid and ice phases used in the model. The solid lines are the remainder when environmental condensation is subtracted from \widehat{Q}_c .

In ascending regions, heating due to environmental condensation increases with SST, particularly between the 300 K and 305 K simulations. Figure 4.5b shows that most of this increase is from the stronger vertical moisture gradient, which increases following the increase in the slope of the saturation mixing ratio curve with temperature. Between the 300 K and 305 K simulations, panel c shows that below $\sigma_h = 0.6$ and above $\sigma_h = 0.4$ there is an additional contribution from a stronger upward \widetilde{M} (computed as the average \widetilde{M} where $\widetilde{M} > 0$ multiplied by the fraction of the ascending region where $\widetilde{M} > 0$).

Environmental air moving *upwards* is interesting and contrary to how it is typically conceptualized. The environmental mass flux, as defined presently, is sensitive to the choice of the vertical velocity threshold used to define convection, because I calculate \widetilde{M} using equation (4.10). It is possible that I have underestimated the convective mass flux; if so, this would favor upward values of \widetilde{M} . However, rising air in the environment is physically interpretable: Positive values of

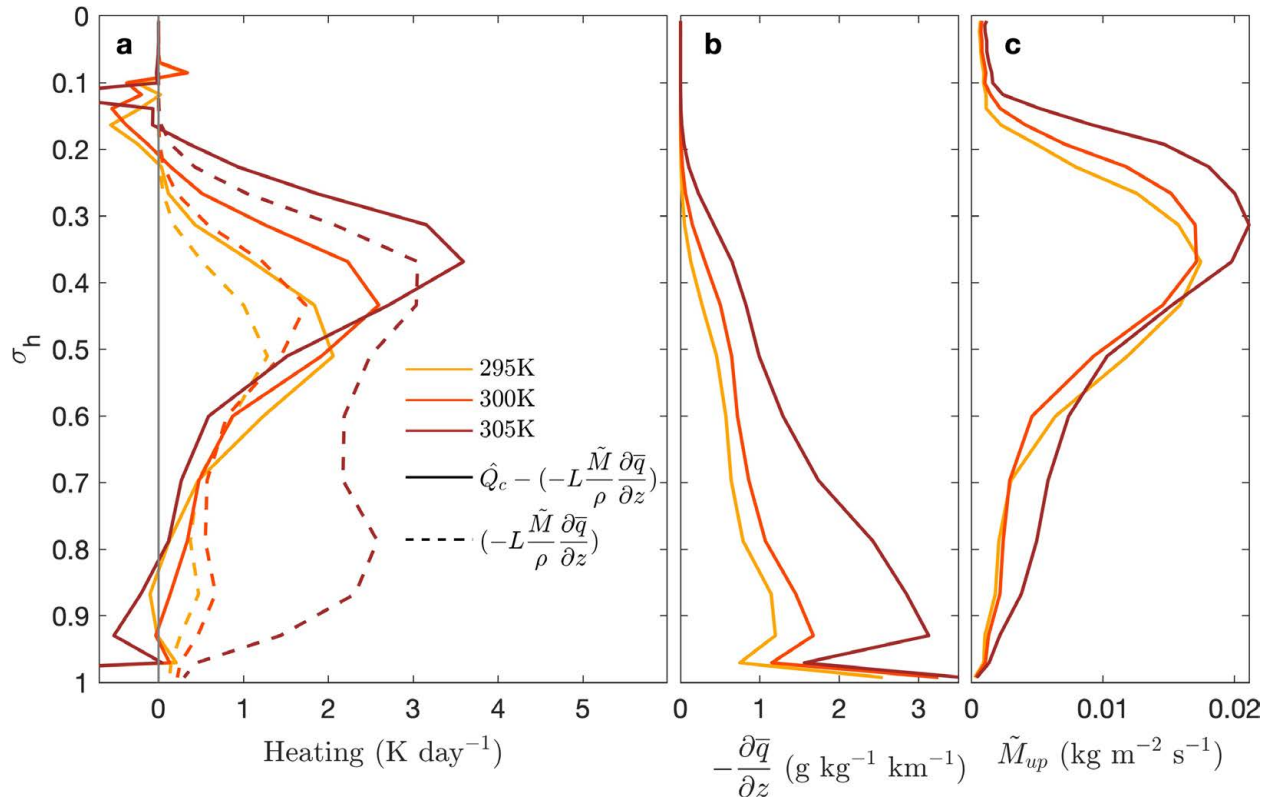


Figure 4.5: For ascending regions: a, Contributions to \widehat{Q}_c from environmental condensation, estimated as $-L \frac{\widetilde{M}}{\rho} \frac{\partial \bar{q}}{\partial z}$, and the remainder $\widehat{Q}_c - \left(-L \frac{\widetilde{M}}{\rho} \frac{\partial \bar{q}}{\partial z}\right)$. b, Negative vertical water vapor mixing ratio gradient. c, Mean upwards \widetilde{M} .

\widetilde{M} in the middle and upper troposphere favor the formation of stratiform anvil clouds, which are well-understood to be important for the heating associated with mesoscale convective systems.

Equations (4.10) and (4.11) allow Equation (4.2) to be rewritten as

$$\frac{\widetilde{M}}{\rho} \frac{\partial \bar{s}}{\partial z} = \overline{Q_R} + \widehat{Q_c}. \quad (4.15)$$

Writing WTG balance in terms of \widetilde{M} , as in equation (4.15), permits the diagnosis of the relevant terms in the heating balance important for the environmental mass flux of a large area, regardless of whether or not the area contains convection (Arakawa & Schubert, 1974; Chikira, 2014). For grid cells containing active convection, equation (4.15) says that the dry static energy advection by the environmental mass flux, $\frac{\widetilde{M}}{\rho} \frac{\partial \bar{s}}{\partial z} = \frac{1}{\rho} (\overline{M} - M_c) \frac{\partial \bar{s}}{\partial z}$, balances the combination of stratiform heating and radiative cooling. For grid cells that don't contain active convection, $M_c = 0$, $\widetilde{M} = \overline{M}$, $\widehat{Q_c}$ is typically negligible, and equation (4.15) reduces to a balance between radiative cooling and advection of dry static energy by the mean vertical motion. Equation (4.15) shows that the environmental mass flux of an area is upwards when the net heating $\overline{Q_R} + \widehat{Q_c}$ is positive. Part of the heating that the upwards \widetilde{M} balances is due to \widetilde{M} being upwards. That is, heating from environmental condensation associated with upwards \widetilde{M} , in part balances the advective cooling due to the upwards \widetilde{M} . This is a way to understand why \widetilde{M} is upward.

In ascending regions, where an upwards \widetilde{M} contributes to $\widehat{Q_c}$, the environmental condensation term, approximated using equation (4.14), can be subtracted from $\widehat{Q_c}$ to roughly estimate the magnitude of heating from detrainment and turbulent fluxes. Figure 4.5a shows that this heating is large in the upper troposphere. Some of this it may be from a covariance between \widetilde{M} and $\partial \widetilde{q} / \partial z$ on time scales faster than a day; these would be missed in the calculation of $L\widetilde{C}$ using daily mean values. The apparent importance of detrainment and turbulence in the heating budget in ascending regions requires further investigation. This is an important question because the increase of $\widehat{Q_c}$ with warming, which is largely contributed to by an increase in this residual heating term in the

upper troposphere, is directly linked to the decrease of α_{up} with warming, and hence how the mean circulation responds to warming.

4.2.3 Response of the convective mass flux to warming

In the simulations of global RCE, the decrease of α_{up} with SST is directly related to fact that the net non-radiative heating in ascending regions intensifies faster than the radiative cooling in descending regions. In the upper troposphere, an increase in \widehat{Q}_c explains most of the increase in the total \overline{Q}_c in ascending regions, between the 300 K and 305 K simulations. Much of the increase is due to the intensification of the vertical moisture gradient with warming. Between the 295 K and 300 K simulations, there is an additional contribution to the increase in \overline{Q}_c from $\frac{M_c}{\rho} \frac{\partial \bar{s}}{\partial z}$. Interestingly, this is not the case between the 300 K and 305 K simulations, where $\frac{M_c}{\rho} \frac{\partial \bar{s}}{\partial z}$ in the ascending region *decreases* throughout the lower- and mid-troposphere. I am thus motivated to more closely investigate how the heating associated with the convective mass flux changes with increasing SST.

The non-monotonic changes in $\frac{M_c}{\rho} \frac{\partial \bar{s}}{\partial z}$ in ascending regions are due to non-monotonic changes in M_c with warming rather than changes in $\frac{\partial \bar{s}}{\partial z}$, which increases monotonically with SST. For the remainder of this section, I will thus focus on changes of the convective mass flux with SST.

I will extend this analysis to the entire domain, rather than just focusing on the ascending region alone, to get a more complete understanding of how M_c changes with SST. Figure 4.6a shows the vertical profiles of the global mean M_c . Consistent with previous work suggesting a decrease in M_c with warming (Held & Soden, 2006; Vecchi & Soden, 2007), I find that M_c weakens throughout the troposphere.

The decrease in the global mean M_c with SST is monotonic, with the largest decrease occurring between the 300 K and 305 K simulations between about $\sigma_h = 0.9$ and $\sigma_h = 0.4$. When the ascending and descending regions are separately considered, I find that the change of M_c with SST is not monotonic with SST and opposite between the regions. Figure 4.6e shows the total M_c in the ascending and descending regions. Below $\sigma_h = 0.35$, there is a very small increase (decrease)

in M_c in ascending (descending) regions between the 295 K and 300 K simulations. The change is opposite between the 300 K and 305 K simulations, with M_c decreasing (increasing) in ascending (descending) regions. While the combination of the changes produces a monotonic decrease in the global mean M_c with SST, the region-specific patterns of change have unique effects on the heating budgets of the ascending and descending regions (and hence α_{up}). For example, the decrease of M_c in descending regions and increase in ascending regions between the 295 K and 300 K simulations, neglecting how heating from other processes changes, increases the ratio $\overline{Q_{up}}/\overline{Q_{dn}}$, and hence contributes to a decrease in α_{up} . Conversely, the increase of M_c in descending regions and decrease in ascending regions between the 300 K and 305 K simulations is related to the opposite change in α_{up} .

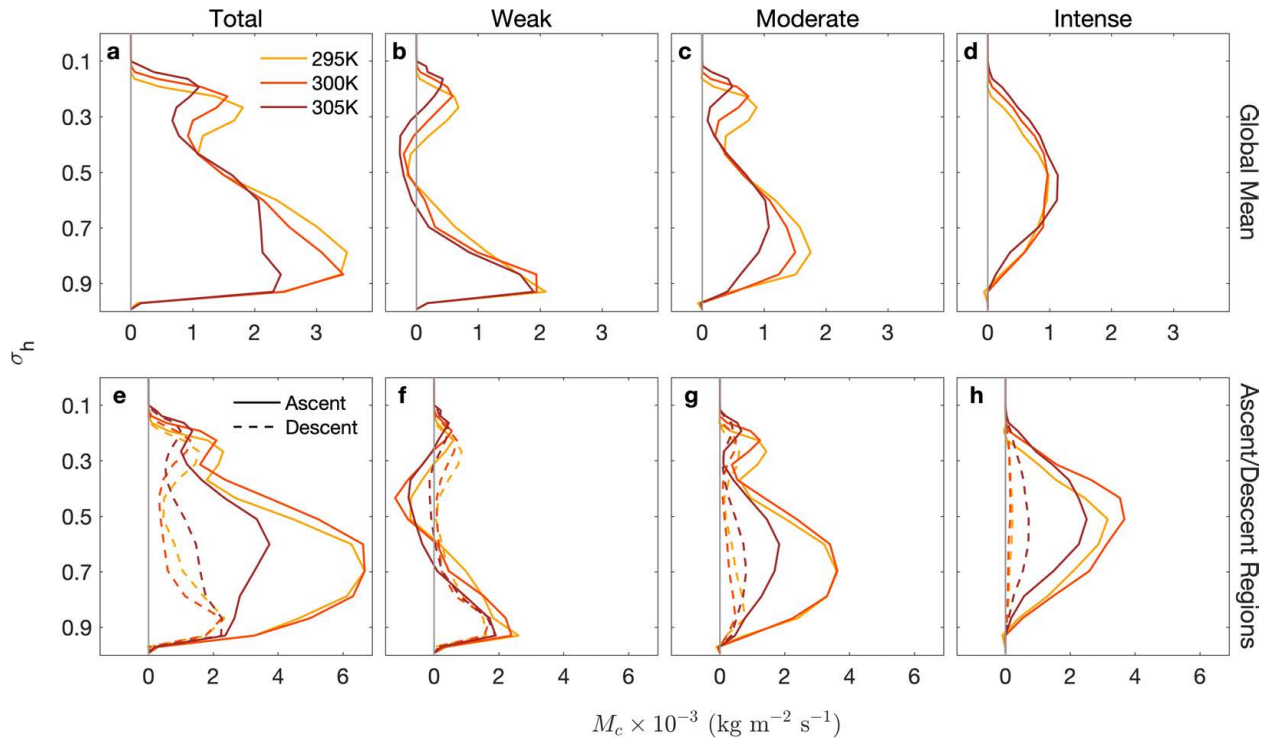


Figure 4.6: (Top row) Global mean profiles of simulated M_c for different intensity bins. a, Total convective mass flux. b, Convective mass flux from weak convection; c, moderate convection; d, intense convection. (Bottom row) Mean convective mass flux for the ascending (solid) and descending (dashed) regions: e, total; f, weak convection; g, moderate convection; h, intense convection.

I now subdivide M_c into contributions from weak, moderate, and intense convection following the definitions given in section 4.1.2. Panels b-d of Figure 4.6 show the global mean total M_c for convection in these intensity classifications and for each simulation. Convective mass fluxes from weak and moderate convection decrease with SST throughout the troposphere. Panel c shows that the large decrease in the global mean total M_c between $\sigma_h = 0.9$ and $\sigma_h = 0.6$ is mainly due to a decrease in M_c from moderate convection. Below $\sigma_h = 0.7$ there is very little change in M_c from intense convection between the 295 K and 300 K simulations, and a decrease between the 300 K and 305 K simulations. Conversely, above $\sigma_h = 0.7$, there is an increase in M_c from intense convection between the 300 K and 305 K simulation.

Panels f-h of Figure 4.6 show M_c from weak, moderate, and intense convection in the ascending and descending regions. The magnitude of M_c from weak convection is comparable between the regions, except between $\sigma_h = 0.6$ and $\sigma_h = 0.3$ where M_c in the ascending region is negative and about zero in the descending region. As in the pattern of change of the total M_c in ascending and descending regions with SST, the change of M_c from intense and moderate convection is non-monotonic and opposite between the regions. Panel g shows that the decrease of M_c from moderate convection below $\sigma_h = 0.5$ in the global mean profile comes from a decrease in M_c in descending regions between the 295 K and 300 K simulations, with little change over the ascending region; and a large decrease between the 300 K and 305 K simulations over the ascending region, while M_c in the descending region strengthens. For M_c from intense convection, the global mean increase above $\sigma_h = 0.65$ comes not from an intensification of M_c over ascending regions but from an intensification in *descending* regions (which is amplified in the global mean profile because of an increase in α_{dn}).

Changes to the mean convective mass flux can be due to changes in the frequency of convective updrafts, the vertical velocity of convective updrafts, and/or updraft fractional area.

In a warmer climate, updraft speeds are expected to intensify, with the largest increases occurring for the most intense updrafts (Singh & O’Gorman, 2015). This, in part, explains a similar shift with warming in both modeled and observed precipitation (e.g., Chou et al., 2012; Del Genio

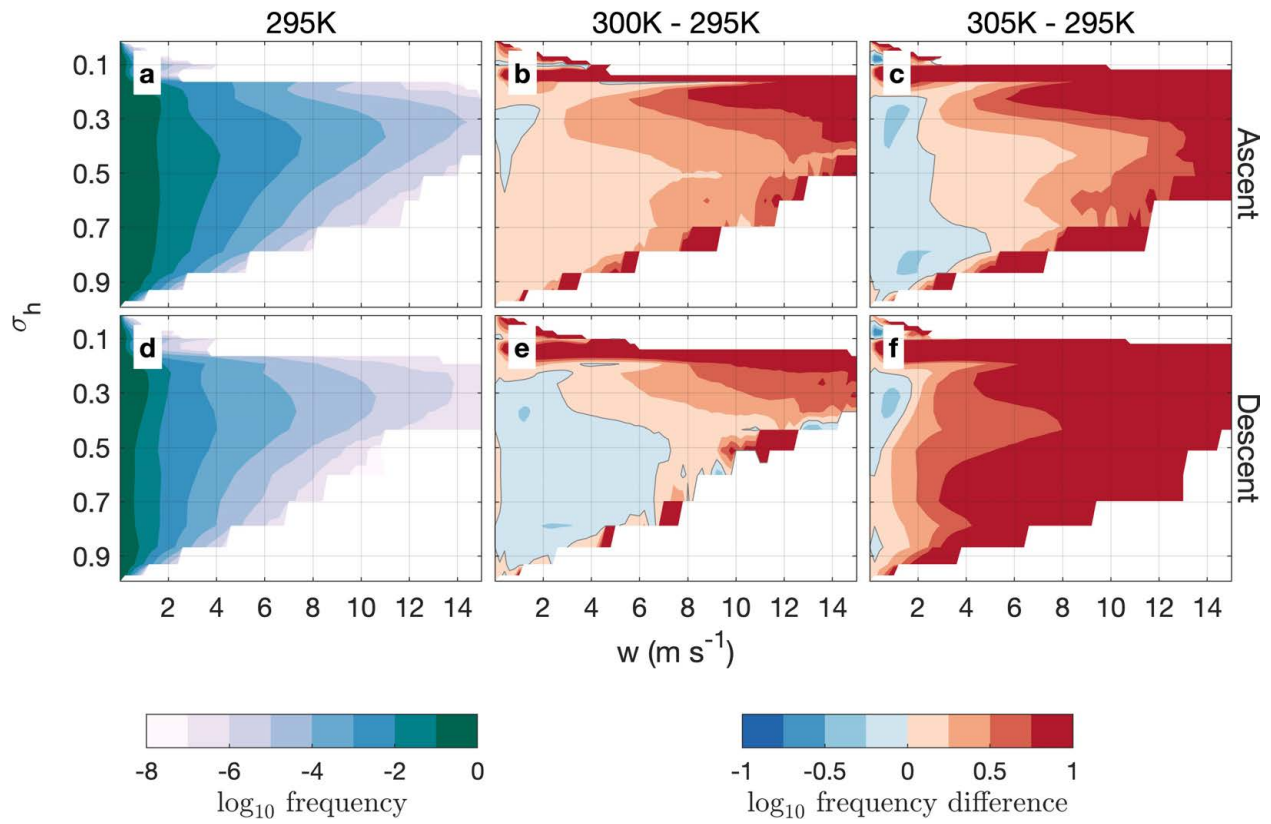


Figure 4.7: For the 295 K simulation, the frequency of hourly mean vertical velocities on the CRM grid exceeding threshold values for the a, ascending and d, descending regions. b, Difference in the frequency between the 300 K and 295 K simulations for the ascending region and e, descending region. c, Difference in the frequency between the 305 K and 295 K simulations for the ascending region and f, descending region.

et al., 2007; Fischer & Knutti, 2016; Lau et al., 2013; Pendergrass & Hartmann, 2014; Sun et al., 2007). Figure 4.7a,d show the \log_{10} distribution of vertical velocities in ascending and descending regions, respectively. Frequencies are calculated as the average fraction of GCM grid cells with at least one CRM grid column containing an hourly vertical velocity that exceeds a threshold value. These frequencies thus include information about the number of GCM grid cells in the ascending/descending region containing an updraft at a certain speed (areal coverage) and the temporal frequency of the updraft speed. Strong vertical velocities are more common in the ascending than in the descending region.

Figure 4.7b,c show the differences in the frequency distributions of vertical velocities between the 295 K and warmer simulations in the ascending region. Note that the differences in Figure 4.7b,c,e,f are also in \log_{10} space, and therefore should be interpreted as ratios rather than arithmetic differences. Changes between the distributions can be influenced by changes to the fraction of GCM grid cells within each region containing updrafts at a certain speed and/or by changes to the temporal frequency of those updrafts. Between the 295 K and 300 K simulations, there is an increase in the frequency of all updraft speeds at all levels, except at speeds below 2 m s^{-1} between $\sigma_h = 0.5$ and $\sigma_h = 0.35$. This is consistent with the intensification of M_c in the ascending region between these two simulations. Between the 295 K and 305 K simulation, there is a decrease in the frequency of all updrafts (blue colors between threshold vertical velocities of 0 and about 2 m s^{-1}), with an intensification of the frequency of the strongest updrafts ($>$ about 2 m s^{-1} above $\sigma_h = 0.7$ and $>$ about 4 m s^{-1} between $\sigma_h = 0.9$ and $\sigma_h = 0.7$). Again, this is consistent with the weakening of M_c in ascending regions between these simulations.

Figure 4.7e,f show the differences in the frequency distributions of vertical velocities between the 295 K and warmer simulations in the descending region. There is decrease in the frequency of all updrafts between the 295 K and warmer simulations, except between $\sigma_h = 0.8$ and $\sigma_h = 0.6$ between 295 K and 305 K. The patterns of change, however, are quite different between panels e and f. Between the 295 K and 300 K simulations, updrafts decrease in frequency at almost all speeds, except in the upper troposphere for $w > 3 \text{ m s}^{-1}$. Between the 295 K and 305 K

simulations, however, there is an increase in the frequency of all updrafts stronger than about 2 m s^{-1} throughout the column.

Generally, there is an increase in the frequency of intense vertical velocities, which agrees with previous work showing that the vertical velocity distribution becomes more positively skewed with warming (Pendergrass & Gerber, 2016). This is directly related to an increase in the mean convective available potential energy (CAPE). Figure 4.8 shows the mean undilute CAPE for parcels lifted from the lowest model level as a function of CRH. The maximum CAPE shifts towards wetter columns in the warmer simulations. There is also an increase in the magnitude of the maximum CAPE by about 500 J kg^{-1} with each 5 K increase in SST.

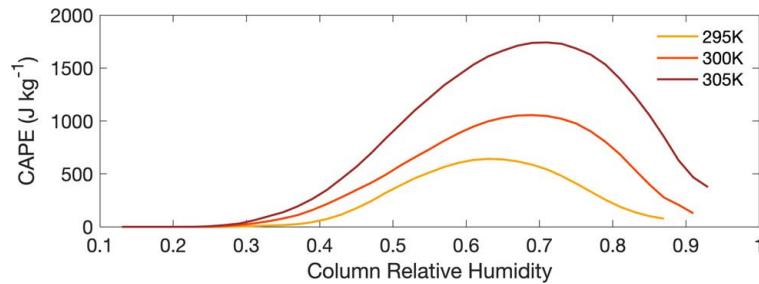


Figure 4.8: Simulated mean convective available potential energy (CAPE) for a parcel based in the lowest model level as a function of column relative humidity.

Figure 4.9a,d show the average updraft fractional area in ascending and descending regions for the 295 K simulation. This is calculated as the average fraction of the CRM grid with vertical velocities exceeding a threshold value, neglecting GCM grid cells that have no updrafts at or exceeding the threshold intensity. Above about 1 m s^{-1} , the fraction of the CRM domain within each GCM grid cell that is ascending is larger in the ascending than in the descending region. As expected, strong updrafts occupy a smaller fraction of the area in both regions.

Figure 4.9b,c show the differences in the updraft fractional area distributions between the 295 K and warmer simulations in the ascending region. The patterns of change are similar to those for the velocity distributions. Between the 295 K and 300 K simulations, the fractional area occupied by updrafts generally increases throughout the column (except for large vertical velocities and at

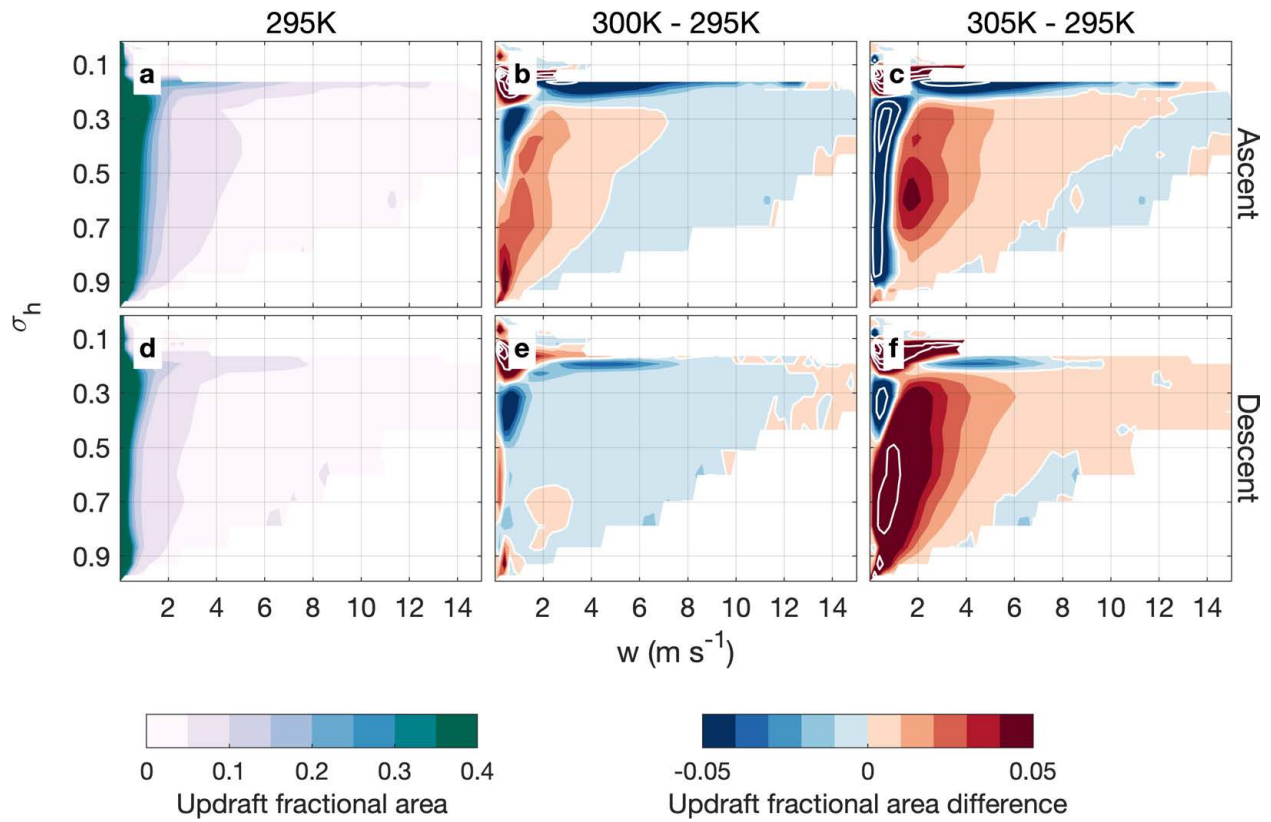


Figure 4.9: For the 295 K simulation, the average updraft fractional area, calculated as the average fraction of the CRM grid with vertical velocities exceeding threshold values for the a, ascending and d, descending regions. b, Difference in the average updraft fractional area between the 300 K and 295 K simulations for the ascending region and e, descending region. c, Difference in the average updraft fractional area between the 305 K and 295 K simulations for the ascending region and f, descending region. White contours in b,c,e,f are drawn every ± 0.10 starting at 0.

the upper levels). Between the 295 K and 305 K simulations, weak updrafts become much ($> 10\%$) smaller while strong updrafts ($> 1 \text{ m s}^{-1}$) become larger.

Figures 4.9e,f show the differences in the updraft fractional area distributions between the 295 K and warmer simulations in the descending region. Changes between the 295 K and 300 K simulations are small. Interestingly, between the 295 K and 305 K simulations, there is a large increase in updraft fractional area for all intensities throughout most of the column.

In summary, despite a monotonic decrease in the global mean M_c , I find non-monotonic changes when I subdivide by the ascending and descending regions. In general, convective updrafts become less common with increased SST, with increases in the size and frequency of the strongest updrafts. However, when looking at changes in just the ascending and descending regions, I find variations that are not consistent with SST and region. A particularly interesting result is the simultaneous decrease in M_c in ascending regions and increase in descending regions between the 295 K and 305 K simulations. That is, the ascending and descending regions are becoming more similar to each other in the 305 K simulation.

4.2.4 Humidity dependence

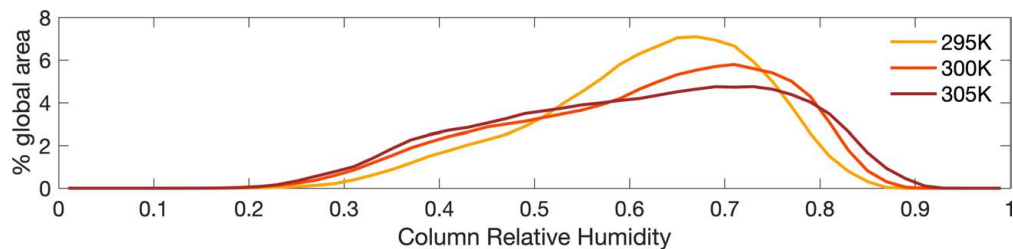


Figure 4.10: Frequency distribution, in average daily percent global area covered, of column relative humidities for bins 0.02 wide.

Up until this point, I have discussed changes to the circulation using averages of quantities taken over very large areas, i.e., either the entire domain, or the ascending/descending regions. In this section, I will discuss the variations to the mean circulation, convective mass flux, and heating terms with SST in more detail by looking at these terms in CRH space. In the real world, tropical

temperature and pressure are close to uniform. Moisture and convective morphology, however, are not. Regions of active deep convection and mean ascent are generally located in the most humid parts of the tropics. Regions of mean descent are conversely located in drier regions. Analyzing changes to the circulation in humidity space permits an assessment of regional changes. In the global RCE simulations, humid regions move around in space and time rather than being linked to geographically fixed SST patterns, the presence of land and topography, or rotation, as they are on earth. Figure 4.10 shows the average daily distribution in percent of global area covered by various CRHs on the GCM grid. Values at the extremes of the distribution are rare, but become more common in the warmer SST simulations. This is seen as a widening and flattening of the CRH distribution, with values drier than 0.5 and wetter than 0.8 both becoming more common with warming, at the expense of the moderate CRHs. An increase in the frequency of dry columns may be associated with an increased state of organization, which dries the atmosphere (Wing et al., 2020).

Figure 4.11a shows \overline{M} for the 295 K simulation binned by CRH percentile. I bin by percentile here because of the shift in the distribution of CRH, and in order to capture differences between the distributions while retaining all of the data. In this figure, the curve separating regions of descent and ascent slopes from drier columns at low levels to wetter columns at the upper levels. Figures 4.11b-c show the difference of \overline{M} binned by CRH percentile between the 300 K and 295 K simulations, and between the 305 K and 295 K simulations, respectively. As was shown in Figure 4.2e, \overline{M} weakens with increasing SST between $\sigma_h = 0.8$ and $\sigma_h = 0.3$. Figure 4.11b-c shows that the intensification of \overline{M} at low levels is occurring for most values of the CRH.

The largest decreases in \overline{M} below $\sigma_h = 0.3$ are in columns more humid than the 80th percentile of the CRH. Figures 4.11d-f show $\overline{Q} = \overline{Q_c} + \overline{Q_R}$ binned by CRH for the 295 K simulation, and its difference from the warmer simulations. Between $\sigma_h = 0.5$ and $\sigma_h = 0.3$, \overline{Q} in this area is increasing with SST, with little change in \overline{Q} below $\sigma_h = 0.5$. The decreases in \overline{M} that occur for columns more humid than the 80th percentile of CRH and between $\sigma_h = 0.8$ and $\sigma_h = 0.3$ are

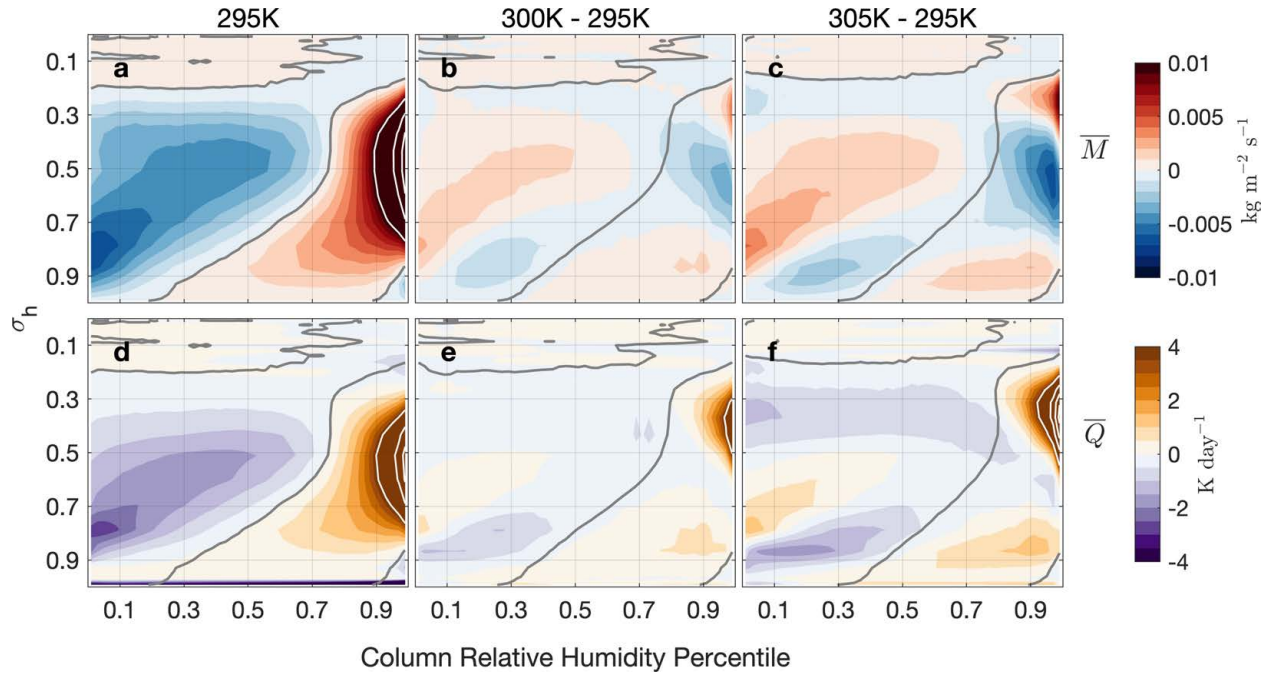


Figure 4.11: Mean mass flux, \overline{M} (top row), and total heating \overline{Q} (bottom row), binned by column relative humidity (CRH) percentile. a, \overline{M} for the 295 K simulation. b, Difference of \overline{M} between the 300 K and 295 K simulations. c, Difference of \overline{M} between the 305 K and 295 K simulations. d-f, As in a-c but for \overline{Q} . White contours in a (d) are drawn every 0.01 $\text{kg/m}^2/\text{s}$ (4 K/day). Grey contour line in all panels are the zero contour of \overline{M} binned by CRH percentile for the a,d 295 K; b,e 300 K; and c,f 305 K simulations.

driven by increases in $\frac{\partial \bar{s}}{\partial z}$. In the part of the column where \bar{Q} is intensifying but \bar{M} is weakening, the increases in dry static stability are outpacing those of \bar{Q} .

In the previous section it was shown that the global mean convective mass flux in the global RCE simulations decreases with increasing SST due to a general decrease in the frequency of weak and moderate updrafts. M_c associated with intense convection increases in the warmer SST simulations mainly because of increases in the frequency and areal coverage of strong updrafts in descending regions. I now analyze changes in M_c and related quantities in CRH space to paint a more detailed picture of what is happening in the simulations.

Figure 4.12a shows the total M_c binned by CRH percentile for the 295 K simulation. The black contour shows the CRH that separates regions of descent (to the left of the line) from regions of ascent (to the right of the line). M_c is generally much larger in the ascending region than in the descending region, and the strongest convective mass fluxes are located in the wettest columns. For columns within the 30th to 70th CRH percentiles, M_c has two maxima. The lower tropospheric maximum is associated with shallow cumulus convection, while the upper-level maximum may be associated with weak convection in stratiform clouds (Houze, 1977). Figures 4.12b-c are similar but for the 300 K and 305 K simulations, respectively. A general weakening of M_c with warming is apparent. Figures 4.13a-c show the same information that is presented in Figures 4.12a-c, but panels b and c now show the difference between the warmer simulations and the 295 K simulation. The largest changes are generally in the wettest columns, above the 90th percentile of the CRH.

Figures 4.12d-l and 4.13d-l show M_c for weak, moderate, and intense convection binned by CRH percentile for each simulation and the differences in intensity-specific M_c between the 295 K and warmer simulations. Weak convection is shallow. It is the main contributor to the total convective mass flux at low levels for the driest columns, and near the tropopause for columns between the 30th and 50th percentiles of CRH. There is a secondary peak in M_c from weak convection over the wettest columns (> 95th percentile). This may be large-scale saturated ascent, rather than weak cumulus convection. Moderate convection extends higher than weak convection and has its strongest mass fluxes in the wettest columns. The convective mass flux of intense convection is

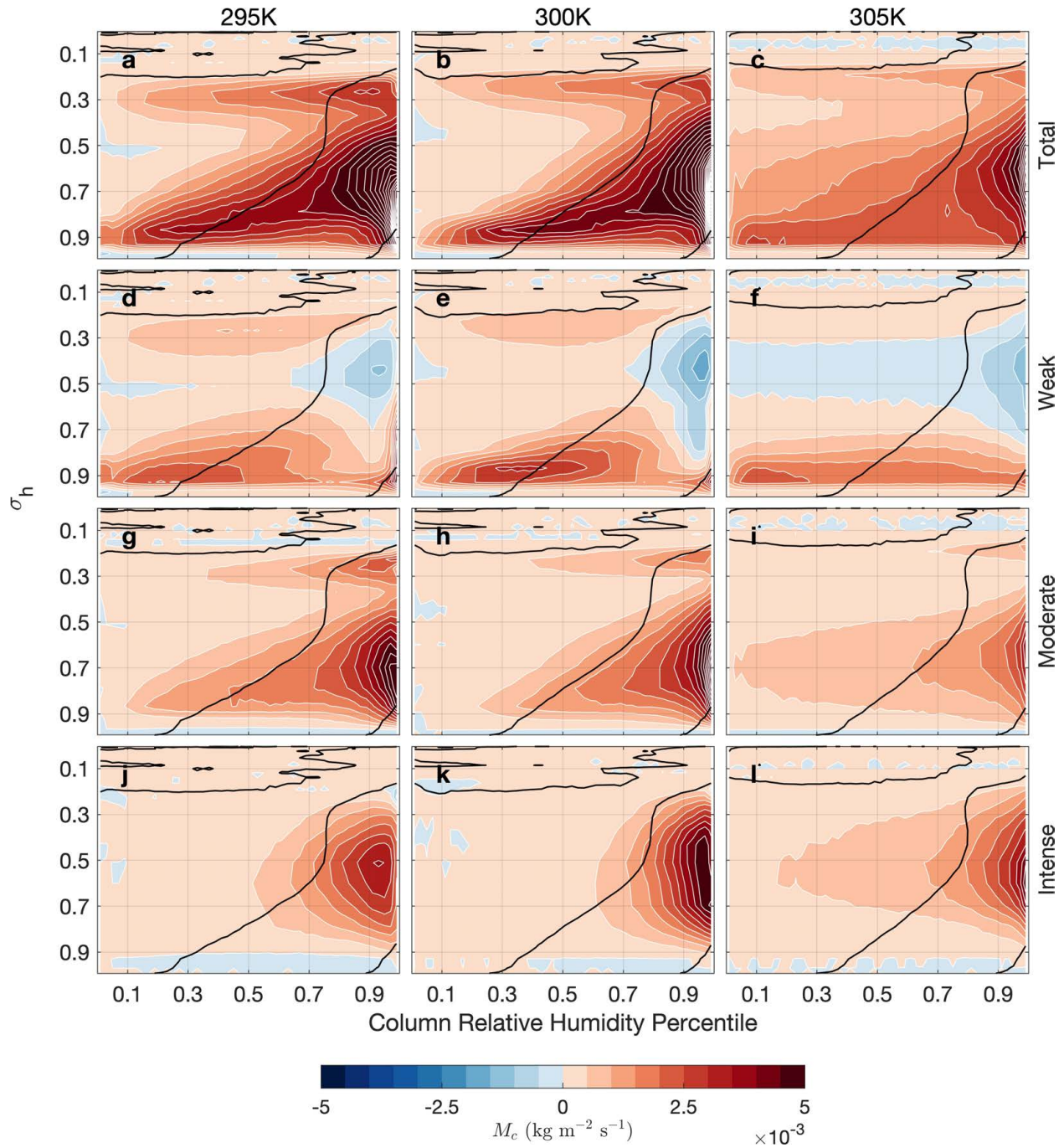


Figure 4.12: M_c binned by column relative humidity (CRH) percentile from (top row, a-c) all convection; (second row, d-f) weak convection; (third row, g-i) moderate convection; and (bottom row, j-l) intense convection. Left column (a,d,g,j) shows values for the 295 K simulation; center column (b,e,h,k) shows values for the 300 K simulation; and right column (c,f,i,l) 305 K simulation. Black contour line in each panel is the zero contour line of the mean mass flux, \bar{M} , binned by CRH for the corresponding simulation.

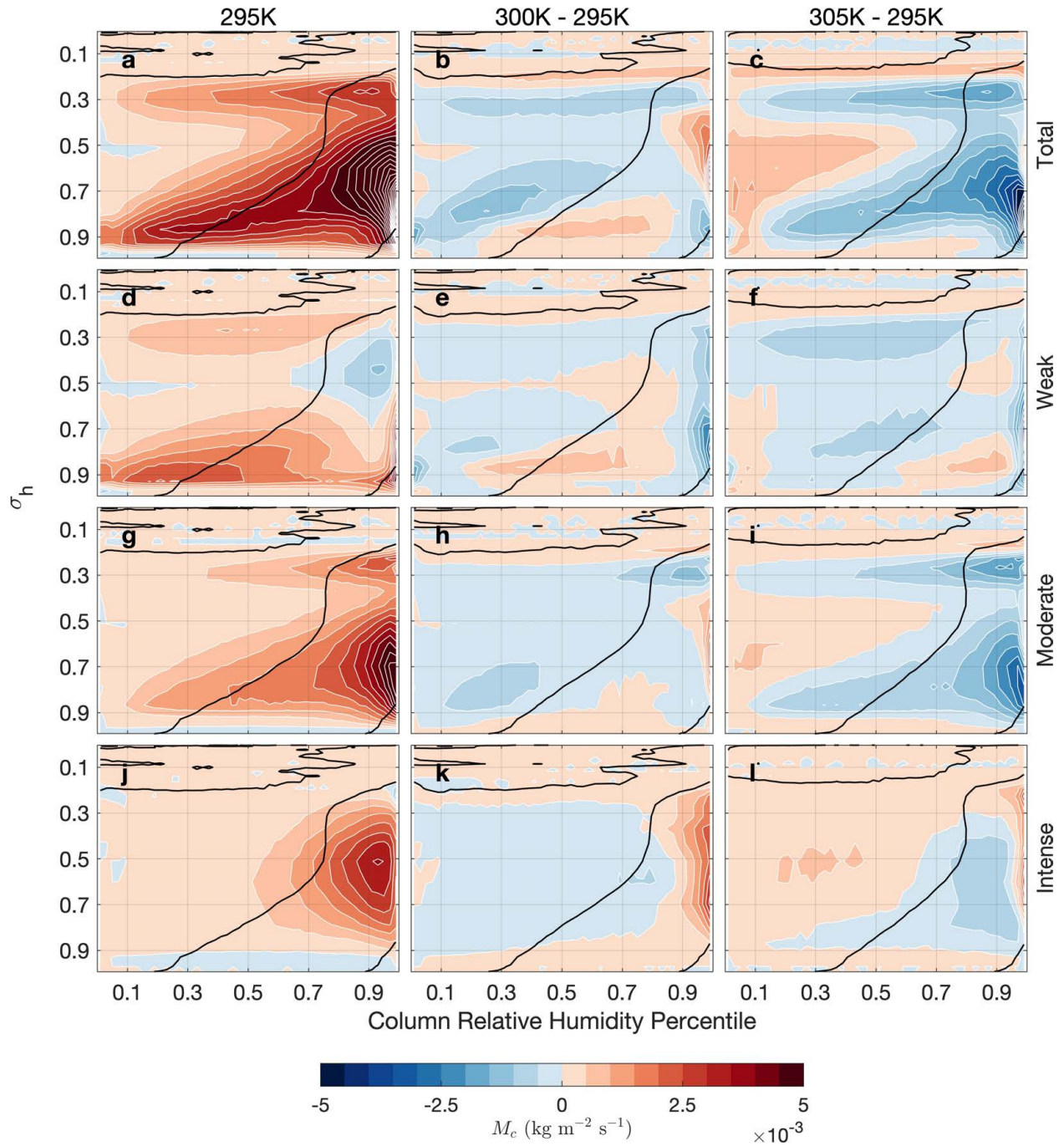


Figure 4.13: As in Figure 4.12 but the center and right columns now show the difference between the 300 K and 295 K simulations (center column) and 305 K and 295 K simulation (right column). Black contour line in each panel is the zero contour line of the mean mass flux, \bar{M} , binned by CRH for the (left column) 295 K, (center column) 300 K, and (right column) 305 K simulations.

located higher in the troposphere because large values of vertical velocity are more common there (see Figure 4.7a). It is located in columns where CAPE is large, but in wetter columns than where CAPE is largest (see Figure 4.8). This is because CAPE maximizes in columns with CRHs around 70%, where dry air entrainment can decelerate cumulus updrafts (e.g. Romps & Kuang, 2010).

In the previous section it was shown that the total M_c decreases monotonically with SST, despite competing and non-monotonic trends between the ascending and descending regions. Between the 295 K and 300 K simulations, I find an intensification of M_c in ascending regions despite a weakening of the total M_c . This is mainly due to an increase of M_c from moderate and intense convection in ascending regions. Figures 4.13b,e,h,k show that this intensification is occurring in the wettest columns (CRH > 90th percentile). The weakening of the global mean M_c between these two simulations is driven by a decrease of M_c from convection of all intensities in the descending region, and is amplified by the increase in α_{dn} . Figures 4.13b,e,h show that this weakening is spread across the descending region.

Between the 295 K and 305 K simulations, there is a large decrease in M_c , primarily from a weakening of M_c from moderate convection in the ascending region (Figures 4.6g and 4.13i). This is despite an intensification of M_c from intense convection in the descending region. Looking at Figures 4.6h, 4.12l, and 4.13l, this increase in M_c in the descending region is small, and occurs for columns wetter than the 20th CRH percentile.

Neelin et al. (2003) and Chou and Neelin (2004) discuss mechanisms responsible for increases in precipitation at the centers of convective areas with simultaneous decreases at their edges. For the wettest regions, there is sufficient moisture to trigger deep convection. In warmer climates, more precipitation is produced in these regions because the air contains more water vapor. At the edges of the precipitation centers, precipitation is inhibited by dry air input resulting from stronger low level moisture gradients. This pattern of change is observed in M_c , which is closely related to precipitation, in some of the differences between the simulations. Figure 4.13h,k,l, which show the change in M_c between the 295 K and 300 K simulations for the moderate and intense convection categories and between the 300 K and 305 K simulations for the intense category, each have a

pattern of intensifying convective mass fluxes in the wettest columns and a decrease at the margins. This pattern is most evident in panel l. However, this pattern is not present in the difference of the overall M_c between the simulations (Figure 4.13b,c), and the reverse pattern occurs for the change in M_c associated with weak convection (Figure 4.13e,f).

4.3 Discussion and Conclusions

The warming-induced weakening of the sinking in clear-sky regions can be understood by considering the tropical clear-sky energy balance. The atmosphere is continuously losing energy radiatively, and this energy sink is balanced by adiabatic descent and warming. For a given radiative cooling rate, the strength of the sinking motion is dictated by the mean tropical static stability profile, which is nearly constant throughout the real-world tropics due to the inability of the tropical atmosphere to support strong pressure gradients. The tropical static stability profile roughly follows a moist adiabat, and will likely become more stable with surface warming in addition to becoming more stable in direct response to increased CO_2 (Merlis, 2015). Increased static stability makes sinking motions in clear-sky regions more efficient, so that for a given amount of radiative cooling slower subsidence is required to maintain energy balance.

This argument has been used to explain why the tropical circulation appears to weaken with warming. However, the rate that mass circulates through the mean flow also depends on the fractional area covered by the ascending and descending regions, and the mean vertical velocity in the ascending regions.

I have used the weak temperature gradient approximation, which is globally applicable in the idealized numerical simulations used here, to develop a simple diagnostic that links the fractional area covered by the ascending region (α_{up}) to the strength of the mean circulation. I show that it is a good approximation in simulations of global radiative-convective equilibrium (RCE) using a model with superparameterized convection. I use it to demonstrate how large increases in non-radiative heating in the ascending region are associated with the decrease in α_{up} with increasing sea surface temperature (SST).

I find that the increase in heating in the ascending region, $\overline{Q_{up}}$, is primarily due to an increase in what I have euphemistically called “stratiform heating,” which includes heating due to environmental (non-convective) condensation, detrainment, and turbulence. Most of this increase in the lower troposphere, and about half in the upper troposphere, can be explained by increases in the vertical moisture gradient with warming, which makes latent heating via environmental condensation more efficient for a constant environmental mass flux in the spaces between the convective updrafts and downdrafts. An investigation of the changes to stratiform heating, and the relationship (if any) between stratiform heating and the heating associated with the convective mass flux, would be an interesting subject for future work.

Byrne and Schneider (2016a) recently developed a theory aimed at explaining the width of the intertropical convergence zone (ITCZ) using an energetics framework. Byrne and Schneider (2016b) use this theory to analyze the observed and modeled contraction of the ITCZ with warming, and determine that it is primarily the result of increased atmospheric moisture, which steepens the meridional moist static energy gradient, and enhances ITCZ cooling through advective and eddy heat transfer. While I similarly find that increased atmospheric moisture is related to the contraction of the ascending area, my analysis shows that it is associated with increased heating in the ascending area. There are important differences between the framework proposed by Byrne and Schneider (2016a) and that outlined here. My simple approximation for the fractional area of the ascending region is made possible by assuming weak temperature gradients, which allows horizontal energy transport to be neglected. This is a good assumption for the tropics and for the global RCE simulations analyzed here. On earth, the Hadley circulation extends into the subtropics where stronger horizontal temperature gradients and rotation give rise to larger horizontal heat transports. Additionally, the framework developed here applies to the total ascending area, rather than the area of the zonal mean tropical circulation. Nevertheless, this framework may be useful for understanding warming-induced changes in the zonally asymmetric Walker circulation.

Using the diagnostic for α_{up} , I obtained an expression for the strength of the mean overturning circulation, \overline{M} . It is inversely proportional to the mean tropical dry static stability, and propor-

tional to the magnitude of the product of the mean heating rates over the ascending and descending regions. Increases in \overline{M} with surface warming are possible given sufficient intensification of the heating in ascending regions and/or cooling in descending regions. The rate of increase in atmospheric radiative cooling with warming is small, however. I have shown that implausibly large increases in heating in the ascending regions would be needed to strengthen \overline{M} , given the rate that dry static stability strengthens with warming. This is why the strength of the mean circulation decreases with warming.

An important question is whether the framework that I have proposed for relating ascending area and the strength of the mean circulation to regional heating rates is too simple to be used to understand the real world. Popp and Bony (2019) noticed a relationship between the degree to which ITCZ convection is zonally clustered and the strength and width of the ITCZ's circulation. They attribute the observed and modeled link between increased clustering and a weakening/widening of the Hadley circulation to decreases in the net heating of the ITCZ, which is in part due to increased radiative cooling from a larger equatorial non-convective region. Their results suggest that the framework I have proposed may be useful for understanding observed variability in the tropical circulation. Other studies have attributed model spread in the simulation of ITCZ width to differences in the modeled response of clouds and radiation to warming (Su et al., 2019), much of which appears to be related to diversity in convective parameterizations (Schiro et al., 2019). The results presented here emphasize the importance of the net heating in the ascending, convective region for the tropical ascent area. I pose that a better understanding of how non-radiative heating over ascending regions responds to warming will help build confidence in future projections of tropical ascent area change.

I have also used the simulations of global RCE with superparameterized convection to investigate changes to the convective mass flux, M_c , with warming. Consistent with Held and Soden (2006), I find decreases in M_c with increased SST. Generally, these decreases are due to less frequent convection, despite intensification of the strongest updraft speeds. My use of a superparameterized model with an earth-like domain size makes this result particularly relevant to the

real world. Previous work has investigated changes to M_c using simulations with parameterized convection (e.g., Vecchi & Soden, 2007).

When I investigate the warming-induced changes of M_c in more detail, I find that the largest changes tend to be located in the wettest columns (column relative humidity percentile > 0.9), where M_c is already large. However, the fractional area covered by these columns is very small (see Figure 4.10). The change in M_c in the much broader dry descending region, despite its very weak magnitude, plays an important role in explaining why the global mean total M_c decreases monotonically with warming. These changes are reinforced by the increase in α_{dn} with SST. For reasons I have not determined, the change in M_c in the ascending and descending regions is non-monotonic and opposite between the regions.

A limitation of this work is the simple bulk microphysics scheme employed by the model. Previous work has shown that in simulations of RCE, single-moment microphysics parameterizations underestimate low clouds when compared to two-moment schemes, which produce more realistic cloud fraction profiles (Igel et al., 2015). Simulated tropical ascent area has been demonstrated to be sensitive to cloud physics parameters (Schiro et al., 2019). Given the importance of clouds in the atmosphere's radiative heating budget, these results may be sensitive to the microphysics parameterization. This is left for future work.

Chapter 5

The future MJO teleconnection

5.1 Introduction

The Madden-Julian Oscillation (MJO) is one of the most important sources of global weather predictability on the extended time range of about 10-40 days (Robertson et al., 2015). Its impact on remote weather is sensitive to a number of factors including the static stability of the tropics (e.g., Wolding et al., 2017), the magnitude of heating anomalies associated with the MJO (Sardeshmukh & Hoskins, 1988), the MJO's propagation speed (Bladé & Hartmann, 1995), the eastward extent of MJO convective propagation (Henderson et al., 2017), and the mean state winds (Henderson et al., 2017), each of which may evolve in response to increased atmospheric greenhouse gas concentrations. There is uncertainty in the response of many of these features to warming (e.g., Maloney et al., 2019). Additionally, cloud parameterizations and coarse grid spacing lead to a relatively poor simulation of the MJO in many climate simulations (Ahn et al., 2017). It is thus unclear how the influence of the MJO over much of the extratropics will change in a future warmer climate (W. Zhou et al., 2020).

One of the global climate changes affecting MJO teleconnection amplitude in which there is more certainty is the strengthening of the tropical dry static stability with surface warming (Xu & Emanuel, 1989; Frierson, 2006). To first order, latent heat release associated with MJO precipitation is balanced by the upward advection of dry static energy. Similarly, radiative cooling in the MJO's dry region is balanced by slow, adiabatic subsidence. The rate that air rises and sinks in the MJO's circulation is tightly constrained by, and inversely proportional to, the tropical dry static stability (Wolding et al., 2016). It is expected that the static stability will increase in the future as the tropical temperature profile adjusts towards the moist adiabatic lapse rate of a warmer surface temperature. Ignoring changes to the MJO's precipitation intensity, this will weaken the MJO's vertical circulation and its associated upper-level divergence. In simulation studies of a future cli-

mate forced with increasing greenhouse gas concentrations, many models predict a weakening of the MJO's circulation strength (Bui & Maloney, 2018; Maloney et al., 2019). However, there is a considerable amount of intermodel spread, much of which is tied to disagreement in future projections of MJO diabatic heating and precipitation (Bui & Maloney, 2018; Maloney et al., 2019; Bui & Maloney, 2019a, 2019b). While previous work has attributed a simulated weakening of MJO teleconnections to the increase in dry static stability (Wolding et al., 2017), a recent study has shown that in climate change simulations the MJO's circulation change is not correlated with its teleconnection changes (W. Zhou et al., 2020).

The lack of an apparent relationship between modeled MJO circulation change and teleconnection change may be related to changes in the mean state winds. Mean state winds, also referred to in this chapter as the basic state or background winds, refer to the winds that vary slowly in time (i.e., on seasonal, rather than daily time scales). Henderson et al. (2017) emphasize the importance of the basic state winds in the MJO teleconnection pattern, showing that biases in modeled MJO teleconnections can be attributed, in part, to biases in the mean state winds. Mean state winds affect both Rossby wave excitation and their propagation. The magnitude of the vorticity and its gradient on the equatorward flank of the jet play an important role in the excitation of Rossby waves by the MJO (Sardeshmukh & Hoskins, 1988; Mori & Watanabe, 2008; Seo & Son, 2012; Seo & Lee, 2017). The jets also act as a waveguide, and their structure and intensity determine the path that Rossby waves take as they propagate, and the types of Rossby waves that can propagate through them (e.g., Hoskins & Ambrizzi, 1993; Karoly, 1983). Tseng et al. (2020) show that differences in Rossby wave propagation drives most of the interannual variability in the MJO teleconnection pattern over the northern Pacific and North America region. W. Zhou et al. (2020) show that modeled increases in the MJO's impact over the North American west coast with warming can mostly be explained by an extension of the Pacific jet, which causes a shift in the MJO teleconnection pattern.

In addition to features of the mean state (its static stability and winds), the MJO teleconnection may also respond to changes to the MJO itself. The MJO teleconnection is known to be sensitive

to its eastward propagation speed. In a simulation study, Bladé and Hartmann (1995) showed that an eastward propagating heat source is associated with a weaker and smaller wavetrain than a stationary heat source. Similarly, a westward propagating heating produces a stronger response than a stationary heat source. This is a linear effect: eastward (westward) propagation effectively embeds the heating in easterlies (westerlies). Many models predict an increase in the MJO's propagation speed with warming (e.g., Rushley et al., 2019), which may contribute to a weakening of the MJO teleconnection with warming.

In the present climate, MJO convection is generally confined to the Indian and West Pacific oceans, while the MJO circulation signal circumnavigates the tropics. In simulations of a future warmer climate, many models predict an increase in the eastward extent of MJO convection (Adames et al., 2017; Bui & Maloney, 2018; Chang et al., 2015; Subramanian et al., 2014). This may be driven by the expansion of the eastward edge of the Indo-Pacific warm pool, a region of very warm tropical sea surface temperatures (Maloney & Xie, 2013). A more eastward propagating MJO will extend the region of Rossby wave excitation by the MJO further eastward as well.

In summary, the MJO teleconnection has a complex dependence on a number of features, each of which may change in a future climate. Model spread in a number of these features makes the speculation of how the MJO teleconnection changes with warming a particular challenge. Not to mention, many climate models struggle to reproduce the observed MJO teleconnection pattern of the current climate (Henderson et al., 2017). How then, can we make reliable predictions of how the MJO teleconnection will change in a future climate? Previous work has already shown that models do not agree on how the MJO teleconnection strength will change with warming (W. Zhou et al., 2020).

This work is aimed at addressing this problem by quantifying the unique impact of climate-change-induced changes to each of the previously mentioned mechanisms on the MJO teleconnection. In other words, given the impact of climate change on individual features of the mean state and MJO, how does the MJO teleconnection respond, and by how much? In this study, I use simulations with a linear baroclinic model (LBM) to quantify the sensitivity of the boreal winter

MJO teleconnection over the Pacific Ocean and North America to perturbations in the MJO and mean state.

5.2 Methods

5.2.1 Linear Baroclinic Model Simulations

The sensitivity of the MJO teleconnection to changes in the MJO's propagation speed, eastward propagation extent, heating magnitude, and of the mean state dry static stability and winds is quantified using simulations with the LBM of Watanabe and Kimoto (2000). The time-integration version of the LBM used here is a spectral model that solves linearized equations for vorticity, divergence, temperature, and surface pressure. The model takes two inputs: a background state and a forcing (which is added to the simulated perturbation field at each time step). A linear model has a few features that make it particularly attractive for the current study. First, it is very inexpensive to run. Second, the linear framework is quite simple, which makes the interpretation of the results straightforward. Third, because the background state is maintained by prescribing it at each time step, it is possible to run simulations with the temperature field out of balance with the wind field. I take advantage of this feature in tests of the sensitivity of the MJO teleconnection to changes in the basic state dry static stability, which can be varied while holding the winds constant, for example.

The model equations are described in appendix B of Watanabe and Kimoto (2000). The model is numerically damped with biharmonic horizontal diffusion, for which I use an e-folding time of 1 hour for the smallest resolvable waves; and with linear drag, with a damping time scale of 0.5 days applied to the lowest 3 model levels, 1 day for the top two model levels, and 20 days for all levels in between. I use this strong damping to prevent the growth of baroclinic waves, particularly because in some simulations I prescribe basic state winds that are not in balance with the basic state temperature. I use a horizontal truncation of T42 (roughly 2.8° horizontal resolution) and 20 vertical levels.

An ensemble of “historical” (2001-2005) and “future” (2096-2100) mean states are derived from averages of five consecutive Januaries of the representative concentration pathway 8.5 (RCP8.5) simulations of the Community Earth System Model (CESM) Large Ensemble (LE) (Kay et al., 2015). I use the CESM-LE in order to identify the magnitude of the consistent climate change signal apart from noise due to internal variability. In using 5 consecutive Januaries, some of the noise due to variability on interannual time scales is suppressed. Previous work has shown that variations in the basic state due to the El Niño Southern Oscillation lead to differences in the MJO teleconnection across the North Pacific and North America region (Tseng et al., 2020). Thus the suppression of the influence of interannual variability increases the consistency between teleconnections simulated by each ensemble member, and aids in the detection of the influence of climate change. I use the first 35 of the 40 CESM-LE members, due to known issues with the last 5⁵. The model is forced with a propagating MJO-like thermal dipole heating with the rate of change of perturbation temperature given by,

$$\frac{\partial T'(\lambda, \phi, z, t)}{\partial t} = A e^{-\frac{\sin^2 \phi}{2\sigma^2}} \sin(k\lambda - \omega t) e^{-\frac{(\lambda-b)^2}{2c^2}} \sin^2 \left(\frac{\pi(z - z_{top})}{z_{bot} - z_{top}} \right), \quad (5.1)$$

where T' is the perturbation temperature of the forcing, ϕ and λ are the latitude and longitude in radians, respectively, z is the model vertical coordinate with subscripts *bot* and *top* referring to the lowest and highest model level, respectively, A is the heating amplitude, k is the zonal wavenumber, ω is the temporal frequency of the heating in days, and t is the time in days. Unless otherwise noted, I set $A = 1 \text{ K day}^{-1}$, $\sigma = 0.1$, $k = 1.9$, ω corresponding to a temporal period of 40 days, $b = 2.27$ radians (130°), and $c = 0.79$ radians (45°). Figure 5.1 shows the heating in the mid-troposphere, where it is a maximum, for $t = 10$ days, 20 days, 30 days, and 40 days. The propagating heat source is constrained to the longitudes over the Indian and West Pacific Oceans by multiplying the sinusoidal heat source by a gaussian (see Eq. 5.1). The model is initialized with the forcing given by setting $t = 1$ day, and integrated for 60 days.

⁵See <http://www.cesm.ucar.edu/projects/community-projects/LENS/known-issues.html>

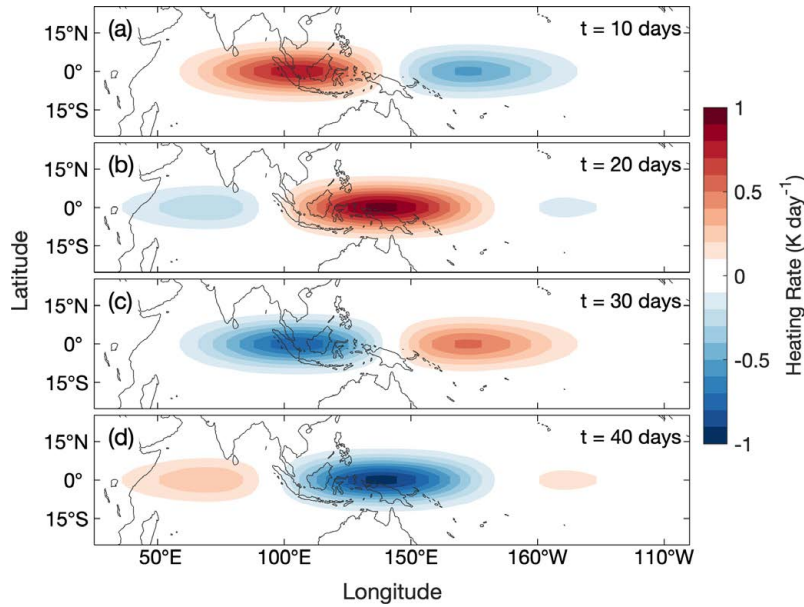


Figure 5.1: Propagating thermal forcing used in the LBM simulations at $t =$ (a) 10 days, (b) 20 days, (c) 30 days, and (d) 40 days.

The LBM simulations used in this study are listed in Table 5.1. The results of previous studies inform the size of the perturbations used in experiments where the full basic state is held constant and the MJO is being perturbed. For climate models simulating realistic MJOs, Rushley et al. (2019) find that the increase in MJO propagation speed may be as much as $4.5\% \text{ K}^{-1}$. Using the increase of the global mean, ensemble mean temperature between the historical and future climates of the CESM-LE, the propagation speed of the perturbed future idealized forcing is chosen to correspond to an MJO period of about 33 days for the experiment where sensitivity to MJO propagation speed is being tested. In modification of the MJO's eastward extent, the eastern edge of the gaussian used to confine the propagating forcing to the Indian and West Pacific Oceans is extended. Specifically, the gaussian multiplier of the future forcing is the historical gaussian with the maximum value sustained for an additional 20° to the east before decreasing. Lastly, Bui and Maloney (2018) find that models that do a better job at simulating observed MJO characteristics simulate changes of the MJO's precipitation amplitude between -10% to $+20\%$ between the historical and future climates under RCP8.5 forcing at the end of the 21st century. In the experiment

Table 5.1: Linear baroclinic model simulations. DSE = dry static energy; hist = historical; futr = future.

Label	Wind	DSE	MJO speed	MJO east extent	MJO intensity
A1	hist	hist	hist	hist	hist
A2	hist	futr	hist	hist	hist
B1	futr	hist	hist	hist	hist
B2	futr	futr	hist	hist	hist
C1	hist	hist	futr	hist	hist
C2	futr	futr	futr	hist	hist
D1	hist	hist	hist	futr	hist
D2	futr	futr	hist	futr	hist
E1	hist	hist	hist	hist	futr
E2	futr	futr	hist	hist	futr

testing sensitivity to MJO amplitude, the perturbed future MJO has a heating amplitude of 1.2 K day^{-1} , corresponding to a 20% amplification of the control forcing.

5.2.2 Defining the MJO in CESM

An MJO index is calculated for the MJO simulated within the first ensemble member of the CESM-LE. While CESM does simulate an eastward-propagating MJO-like convective system, it is much weaker than the observed MJO and that of some other models (Ahn et al., 2017; Li et al., 2016). There is more power at the intraseasonal frequency in the wind field than in outgoing longwave radiation, and so MJO variability in the model is quantified using the first two empirical orthogonal functions (EOFs) of the butterworth bandpass filtered (10-100 days) daily anomalies of the velocity potential difference between 850 hPa and 200 hPa, as in Adames and Wallace (2014). This is done for all months of the two 10-year periods of 1996-2005 and 2091-2100. The leading two EOFs for each period are plotted in Figure 5.2, where projected anomalies of outgoing longwave radiation for each EOF are included. For the earlier period (later period), the first two EOFs explain 23.4% and 22.9% (32.6% and 29.2%) of the total intraseasonal variance, respectively, are well-separated from the other EOFs, and are in quadrature.

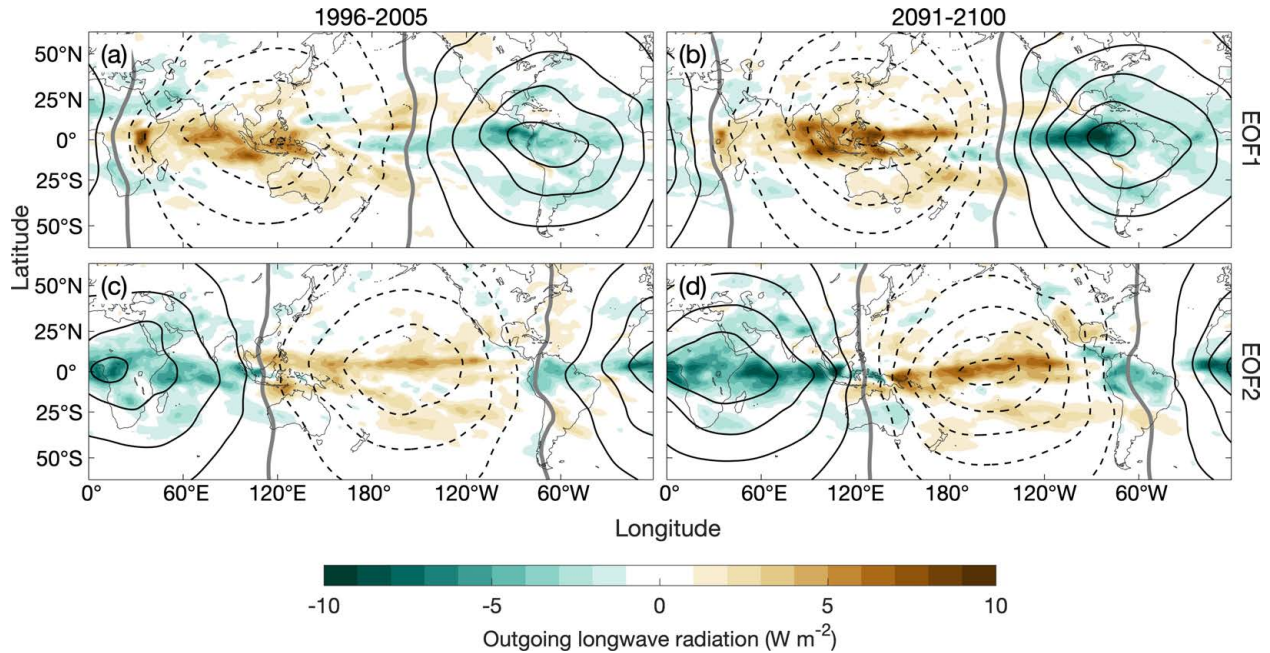


Figure 5.2: First two empirical orthogonal functions (EOFs) of the intraseasonal velocity potential difference between 850 hPa and 200 hPa (contours), and projections of outgoing longwave radiation for each EOF (shading) for (a,c) 1996-2005 and (b,d) 2091-2100. (a,b) EOF1 and (c,d) EOF2.

5.3 Results

5.3.1 Simulated teleconnection change in CESM

I begin with an example that demonstrates the simulated MJO teleconnection and its change in the first ensemble member of the CESM-LE. The “Sensitivity to the Remote Influence of Periodic Events” (STRIPES) index is a useful tool to quantify the magnitude of the consistent MJO signal in remote regions (Jenney, Randall, & Barnes, 2019). Figure 5.3a shows the STRIPES index for January meridional wind at 850 hPa across the northern hemisphere for the period between 1996-2005. I am motivated to use meridional wind at 850 hPa to quantify the MJO teleconnection signal because of the importance of the MJO for prediction of near-surface weather. Over North America, advection is the primary mechanism through which the MJO influences low-level temperature (Seo et al., 2016). Over the northern Pacific Ocean and North America, the simulated hotspots of MJO impact during the historical period are along the northeast Pacific Ocean, and to the north of central North America. These regions are located at the edges of the observed, current climate hotspots in 500 hPa geopotential height (Jenney, Randall, & Barnes, 2019), which is expected for meridional

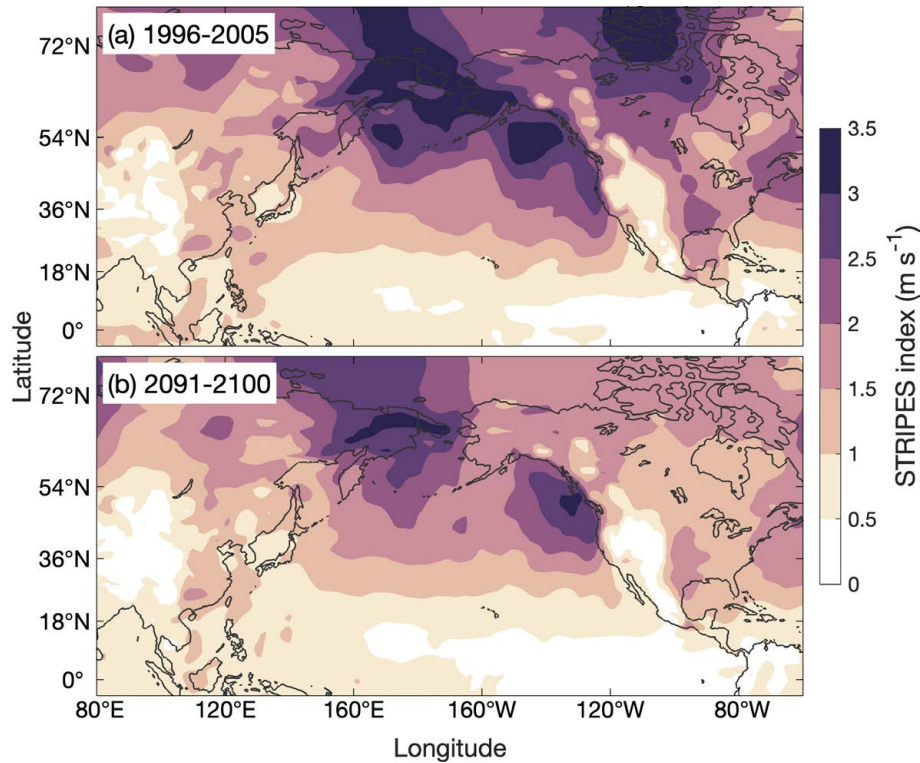


Figure 5.3: STRIPES index of January meridional wind at 850 hPa for the first ensemble member of the CESM-LE for (a) 1996-2005 and (b) 2091-2100.

wind. In the warmer climate, shown in Figure 5.3b, a weakening of the teleconnection amplitude over most regions is observed, especially for the region north of North America.

I have shown the simulated teleconnection change in the first ensemble member of the CESM-LE as an example. Untangling the mechanisms causing the change to the MJO teleconnection in the model is challenging. Many complex and competing factors are at play. Next, instead of trying to understand the causes of the simulated MJO teleconnection in CESM or other global climate models, I will shift focus and use targeted idealized simulations with an LBM to better understand the mechanisms that drive changes to the MJO teleconnection with warming.

5.3.2 Sensitivity experiments with a linear baroclinic model

I conduct experiments with the experimental setup described by Table 5.2. The propagating MJO-like forcing in the model excites a time-varying response in the extratropics. Figure 5.4a shows the time-varying response of meridional wind at 850 hPa for each ensemble member (thin

light blue lines) and the ensemble mean (thick black line) at 49°N , 211°E . The magnitude of peaks and troughs of the ensemble mean response to the propagating forcing is one way to quantify the magnitude of the consistent (ensemble mean) teleconnection strength at each point. Given that the amplitude of an infinite sine or cosine wave is the square root of twice its variance, I calculate the teleconnection strength at each point as the square root of twice the variance of the ensemble mean meridional wind at 850 hPa over a complete period of the input forcing, starting at day 10. I will refer to this quantity as the “amplitude” of the modeled MJO teleconnection. This metric is qualitatively similar to the STRIPES index of Jenney, Randall, and Barnes (2019), but is simplified in order to be applicable to the idealized LBM setup. The MJO of more complex climate models and of the real world is much more variable between and within an event, exhibits variable propagation speed, amplitude and structure, oftentimes does not propagate completely across the Indian Ocean and West Pacific, and does not always begin at the same longitude. Here, the MJO-like propagating forcing of the LBM smoothly propagates through a cycle at a constant speed and is identical between each simulation.

Figure 5.4b shows the amplitude of the modeled MJO teleconnection for the set of simulations performed with both the basic state dry static energy (the vertical gradient of which is the dry static stability) and winds given by historical values. Comparison to Figure 5.3a shows that the teleconnection pattern and magnitudes are quite different between the MJO teleconnection simulated within CESM, and the teleconnection simulated with the LBM. There are many potential reasons for differences, including differences in the structure, intensity, and propagation characteristics of the MJO, nonlinearity in the teleconnection simulated by CESM, the presence of non-MJO features in CESM which add noise not present in the LBM experiments, the fact that Figure 5.3a shows the teleconnection magnitude for a single ensemble member, and Figure 5.4b is for the ensemble mean. Additionally, it is possible that the sample size of 10 consecutive Januaries used in Figure 5.3 contains too much noise to reliably represent the magnitude of the MJO signal, and selectively amplifies regions of higher climatological meridional wind variance. Additionally, magnitudes in Figure 5.4b are weaker than those shown in Figure 5.3a because I have used a relatively weak

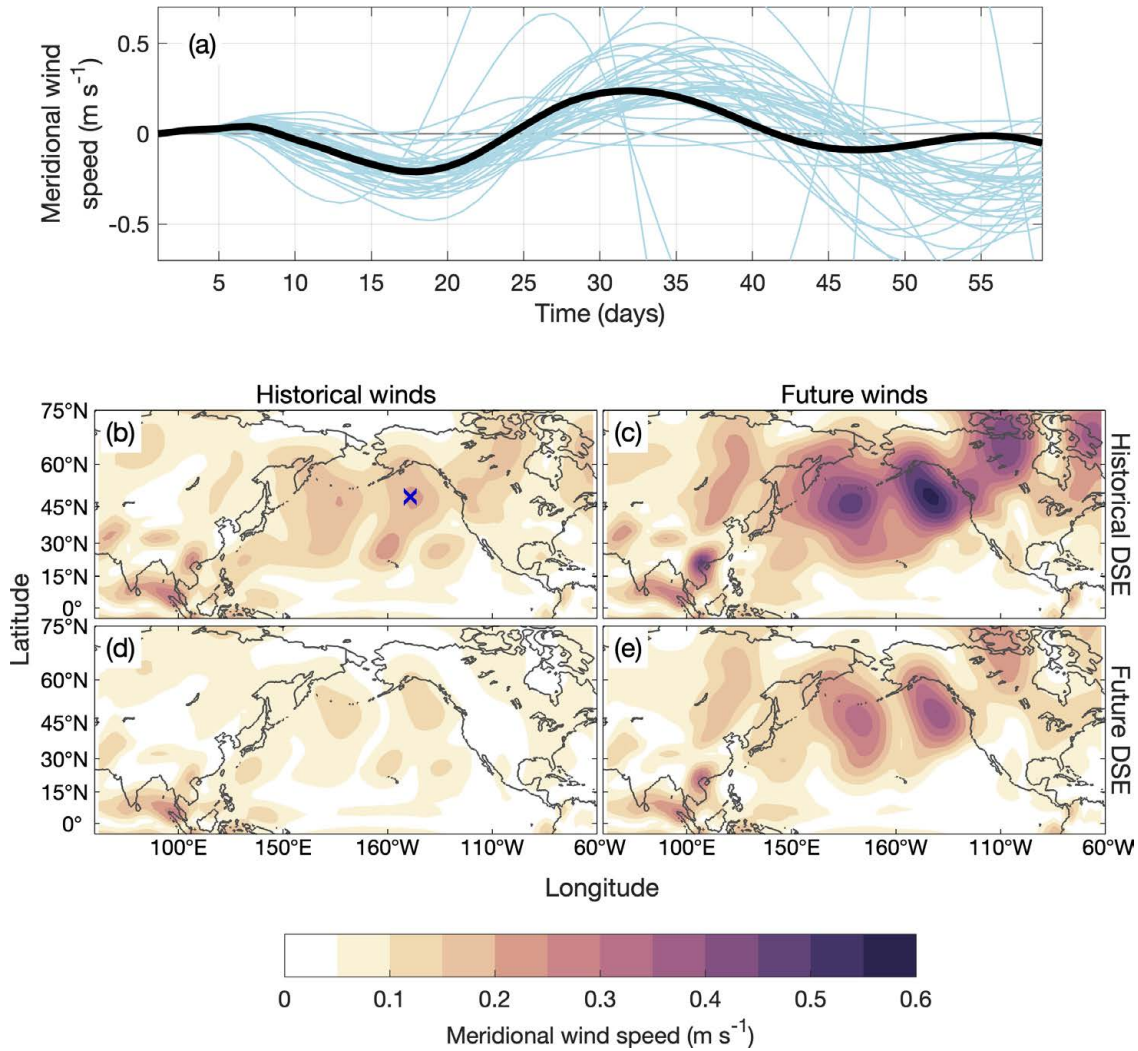


Figure 5.4: (a) The time series of meridional wind at 850 hPa at 49°N, 211°E for each ensemble member (thin blue lines) and the ensemble mean (thick black line) for the set of LBM simulations with the historical basic state winds and dry static energy (DSE). The square root of twice the variance of the ensemble mean meridional wind at 850 hPa for the set of simulations with basic states given by (b) historical winds and DSE, (c) future winds and historical DSE, (d) historical winds and future DSE, and (e) future winds and DSE. These are simulations with labels A1, B1, A2, B2, respectively. The blue “x” in panel (b) is the location shown in panel (a).

amplitude for the propagating input forcing. Nonetheless, the difference between Figures 5.3a and 5.4b is not concerning. The purpose of this study is to estimate the magnitude of the overall teleconnection *change* over the North Pacific and North America region that results from perturbations to the mean state and the MJO, rather than reliably simulating the particular teleconnection pattern and the pattern of its change. It is assumed that the distribution of teleconnection amplitude changes over this large region is not sensitive to the specific representation of the MJO.

Figure 5.4c-e shows the amplitude of the modeled MJO teleconnection but for the set of simulations performed by perturbing the basic state. The thermal forcing used in all simulations is the same. The difference between the top and bottom rows shows the sensitivity of the MJO teleconnection to a change in the dry static energy alone. The pattern of the MJO teleconnection is the same between each top panel and the panel below it, but the teleconnection is weaker in the simulations with future dry static energy because the higher static stability weakens the MJO circulation that results from the prescribed thermal forcing. The difference between the left column and the right column is the sensitivity of the MJO teleconnection amplitude to the simulated change in mean winds between the historical and future climates of the CESM-LE. Now, changes are apparent in both the magnitude of the teleconnection and its spatial pattern.

The difference between panels b and e of Figure 5.4 is the sensitivity of the MJO teleconnection to a change in both the basic state dry static energy and winds. Over most regions, the teleconnection is stronger. This includes the three hot spots at the easternmost tip of the Aleutian Islands, over the Gulf of Alaska, and over the northernmost part of central North America. However, there are regions where the teleconnection is weaker due to a shift in the teleconnection pattern, such as the region just off the southwestern coast of North America. Figure 5.4 shows that changes to the mean winds explain the increases of the teleconnection amplitude over the Northern Pacific and North America. This increase occurs despite the change to the thermal structure of the atmosphere, which alone leads to weaker teleconnections.

I now investigate how changes to the MJO affect the MJO teleconnection by conducting simulations in which the background state is held constant, and either the MJO propagation speed,

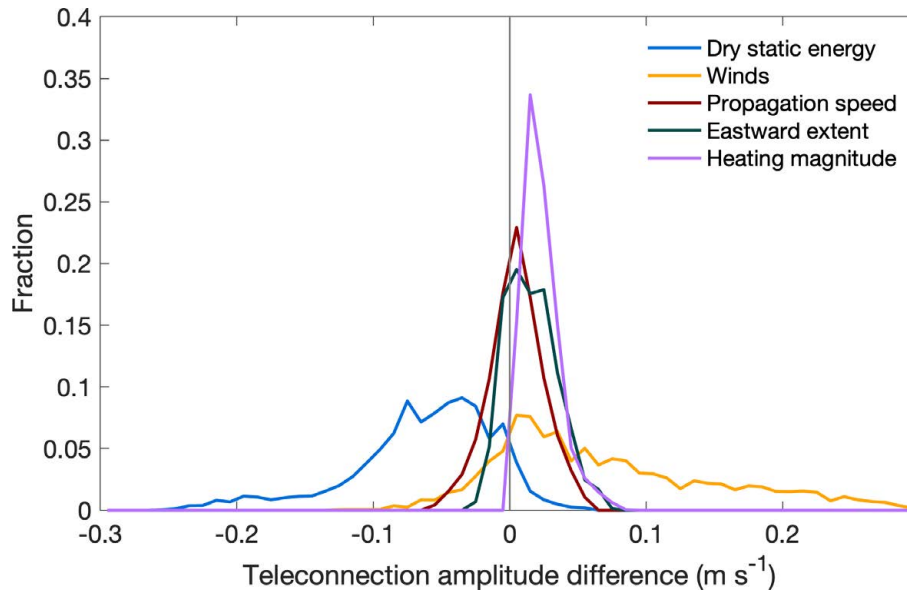


Figure 5.5: Distribution of the difference in the teleconnection amplitude between perturbation and control experiments over the northern Pacific Ocean and North America (150° - 300° E, 15° - 70° N). Distributions plotted are calculated as the mean between the two distributions for experiments 1 and 2 for each perturbed variable (see Table 5.2).

eastward propagation extent, or MJO intensity are perturbed to future values. Figure 5.5 summarizes the results of all simulations over the northern Pacific Ocean and North America region (150° - 300° E, 15° - 70° N). Each line shows the spatial distribution (across grid points) of the difference in the teleconnection amplitude between simulations with a future perturbation and the historical control. Again, for each grid point the teleconnection amplitude is computed as the square root of twice the variance of the ensemble mean time-series of meridional wind at 850 hPa. This is a way of quantifying the magnitude of the inter-ensemble consistent teleconnection across a full period of the MJO-like forcing. Table 5.2 lists the simulations being subtracted to create the distributions shown in Figure 5.5. For each feature, there are two distributions calculated (for the set of experiments listed with I and II in Table 5.2). The distributions plotted in Figure 5.5 are the average between these two distributions. However, for each feature, the resultant two distributions are not very different, which supports the implied assumption that the distribution of MJO teleconnection *changes* over this large region is not state dependent.

Table 5.2: Linear baroclinic model experiments

Feature	Simulations compared	
Dry static stability	I.	A1 & A2
	II.	B1 & B2
Wind	I.	A1 & B1
	II.	A2 & B2
MJO speed	I.	A1 & C1
	II.	B2 & C2
MJO east extent	I.	A1 & D1
	II.	B2 & D2
MJO intensity	I.	A1 & E1
	II.	B2 & E2

For the experiment where the eastward extent of the MJO is increased, only results from the simulation where the eastward extent is increased by 20° are shown, but I also conducted simulations using extensions of 10° and 30° and found similar results (not shown). Distributions with values clustered near zero indicate that there is a small difference in the magnitude of the consistent response to MJO heating between the simulations. That is, the perturbation of the individual feature had little effect on overall MJO teleconnection amplitude across the northern Pacific and North America region. Distributions that are symmetric about zero indicate that between the control and perturbed set of simulations, the difference in the MJO teleconnection is characterized by a shift in the teleconnection pattern. Finally, distributions skewed towards mostly positive or negative numbers indicates that the perturbed feature leads to either a positive or negative change in the magnitude of the MJO teleconnection over most of the region.

The largest changes in teleconnections are for perturbations of the basic state dry static energy or winds. Generally, future perturbations to the dry static energy weaken the MJO teleconnection, while perturbations to the wind strengthen the teleconnection (see Figure 5.4). The tail of the distribution showing the impact of perturbing the basic state wind field is longer than that for dry static energy. This means that for some regions, the possible increase in the magnitude of the MJO teleconnection due to changes in the winds alone is greater than the decrease from changes in the atmosphere's thermodynamic structure. That is, considering basic state changes alone, despite the

weakening of the magnitude of the MJO teleconnection that occurs from an increase in the tropical dry static stability, changes to the mean state winds may lead to an increase in the impact of the MJO over some regions.

MJO changes have a much smaller impact on the magnitude of the MJO teleconnection over the North Pacific and North America region. An increase in the MJO's propagation speed (red curve) leads to a shift in the teleconnection pattern, with no large changes in the overall magnitude of the teleconnection over the region as a whole. Small increases in the magnitude of the MJO teleconnection are apparent due to a 20° increase in the eastward extent and 20% increase in the magnitude of the MJO's heating. However, in isolation these changes are very modest compared to changes in the teleconnection that result from mean state changes.

To the extent that the interactions between the perturbed features are linear in the physical world, and hence may be summed to give the total teleconnection change, Figure 5.5 suggests a few things. First, in a future warmer climate, changes to the basic state, although in isolation responsible for teleconnection amplitude changes of the largest magnitude, here have opposite impacts. In our LBM experiments, these effects largely cancel (see Figure 5.4b-e) over the North Pacific and North America region. Second, in global climate model simulations and in the real world, if future changes to the basic state winds alone support stronger MJO teleconnections over this region, then the effects of basic state changes on the MJO teleconnection will cancel and the future change of the MJO teleconnection may be quite sensitive to the combination of changes to the MJO and the basic state winds. Third, given the upper bound of changes to the MJO (a 20% increase in its magnitude and an increase in its eastward extent), there is potential for an increase in the MJO teleconnection amplitude over much of the northern Pacific and North America region, despite the weakening tendency from the increase in the dry static stability alone.

I now return to the role of the basic state winds in determining the MJO teleconnection amplitude. How are the changes to the mean state winds in the CESM-LE leading to an increase in the magnitude of the consistent teleconnection over the North Pacific and North America region? This

is possible either through an intensification of Rossby wave excitation and/or through mean state shifts that change the nature of Rossby wave propagation in this region.

It is possible to quantify the strength of Rossby wave excitation using the linearized equation for the so-called Rossby wave source (Sardeshmukh & Hoskins, 1988), S' ,

$$S' = -\bar{\zeta}\nabla \cdot \mathbf{v}'_x - \mathbf{v}'_x \cdot \nabla\bar{\zeta} - \zeta'\nabla \cdot \bar{\mathbf{v}}_x - \bar{\mathbf{v}}_x \cdot \nabla\zeta', \quad (5.2)$$

where ζ is the absolute vorticity, \mathbf{v}_x is the divergent wind vector, the overbar represents mean state quantities, and the prime represents anomalies. For the MJO, Seo and Lee (2017) note that the first two terms on the right side of Eq. (5.2), the stretching and advection of basic state vorticity by the anomalous divergent wind, are about an order of magnitude larger than the second two terms, the stretching and advection of anomalous vorticity by the basic state divergent wind, and hence dominate the total S' . Figure 5.6a shows the area-averaged, ensemble mean S' for the two adjacent regions outlined by the black boxes in Figure 5.6b, for the simulations with constant forcing and basic state dry static energy, and historical (solid lines) and future (dashed lines) basic state winds. These two region are chosen because the input forcing is a propagating dipole, which leads to constructive interference of the resultant Rossby waves when the Rossby wave source of the two regions is of the opposite sign (Tseng et al., 2019). Tseng et al. (2019) show that this mechanism leads to more consistent teleconnections given small variations to the mean state. In figure 5.6a, these are times when the Rossby wave source over the western region is of the opposite sign as the eastern region, such as between days 7-12, and 27-30, and 46-50 for the historical period.

Between days 0-5, the Rossby wave source of the two time periods over each region is about the same. This means that differences in the mean state vorticity and its gradient, which are present upon model initialization, are not responsible for the differences in S' between the simulations. It is only after about day 5, when differences in the anomalous circulation begin to emerge, that the Rossby wave source over these regions begins to diverge. That is, the deviation of the future S' from the historical S' after day 5 must be from changes to the \mathbf{v}'_x term, and are not initially due to differences in the basic state.

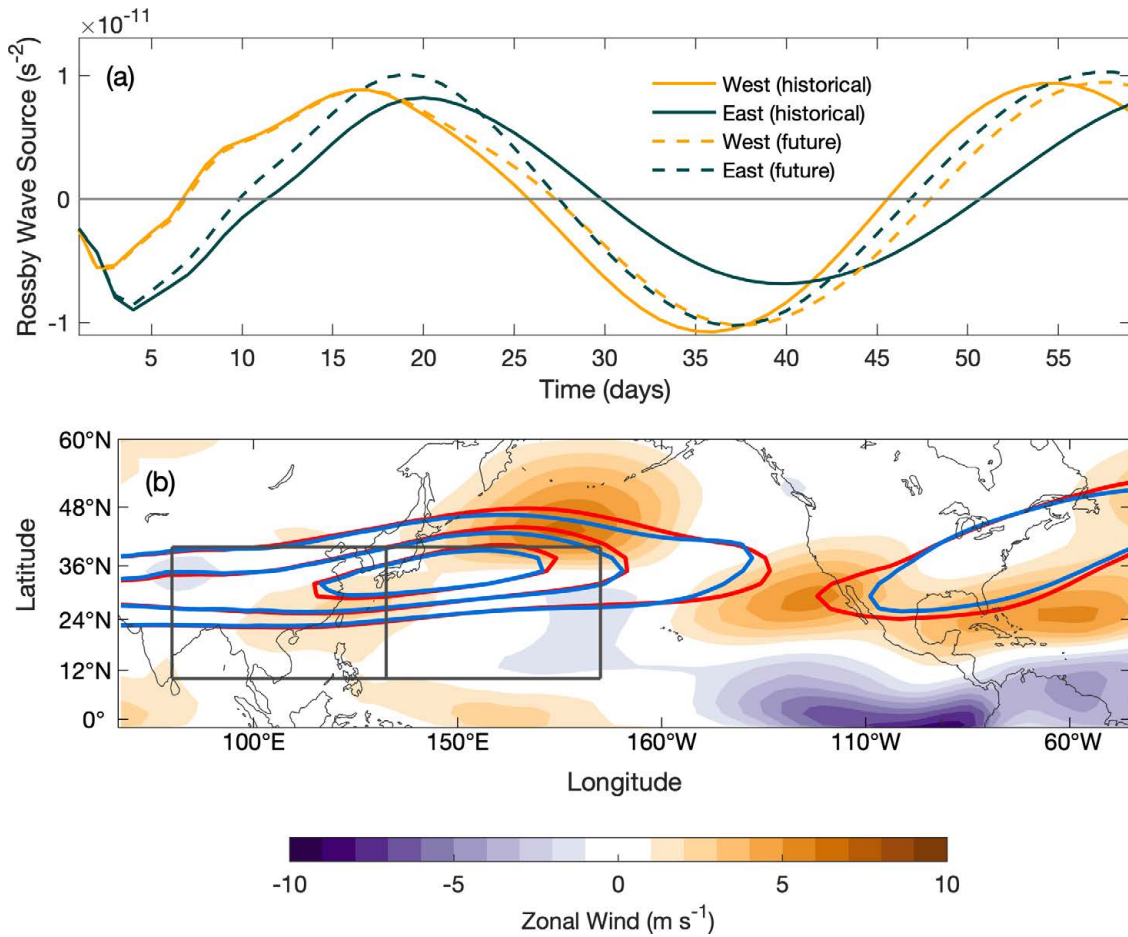


Figure 5.6: (a) The spatially averaged ensemble mean Rossby wave source over the two adjacent regions (west) 10° - 40° N, 80° - 132.5° E and (east) 10° - 40° N, 132.5° - 185° E, for the LBM simulations with constant forcing and basic state dry static energy, and either historical (solid) or future (dashed) basic state winds. (b) Ensemble mean January basic state zonal wind contours for the historical (blue contours) and future (red contours) period, and their difference (shading). Contour lines start at 32.5 m s^{-1} and increase by 15 m s^{-1} . Black boxes outline the west and east regions of panel (a).

At day 27 of the future simulation, the Rossby wave sources of the east and west regions converge and remain in phase with each other throughout the remainder of the simulation. This means that from day 27 onward, the Rossby wave source over the jet entrance region is characterized by a monopole rather than a dipole pattern, which leads to destructive interference of the excited Rossby waves (Tseng et al., 2019). This supports *weaker* teleconnections in the simulations with future basic state winds, and hence does not explain why the opposite is what is actually simulated. I conclude that the increase in the magnitude of the extratropical response to MJO heating over the North Pacific and North America in the simulation with future winds is likely from a change to Rossby wave propagation.

Figure 5.6b shows the structure of the January ensemble mean upper-tropospheric jet for the historical and future CESM-LE climates, respectively. The difference in the zonal wind at the same level between the climates is shaded. The jet extends further eastward, and is wider on its northeast flank. Both the zonal extension of the boreal winter Pacific jet and of the increase of the zonal wind speed on its north flank with warming are robust across models (Matsumura et al., 2019). The eastward extension, specifically, has been shown to be important for simulated increases of the MJO's impact on the North American west coast (W. Zhou et al., 2020). Increases in teleconnection amplitude over the North Pacific and North America region may be related to these changes, although further work is required to verify this and identify specific mechanisms.

Another possible cause of higher teleconnection amplitudes in the simulations with future winds is increased consistency between ensemble members of the basic state winds of the future climate. This would lead to more consistent simulated teleconnection patterns between ensemble members. This is unlikely driving the increase in teleconnection amplitude that we see when running the LBM with future winds because the inter-member variance of upper-tropospheric winds over the Pacific is larger for the future set of basic states than the historical set (not shown).

5.4 Discussion and conclusions

Changes to the impact of tropical heating, such as the Madden-Julian Oscillation (MJO), on the extratropics under global warming may impact climate predictability on subseasonal-to-seasonal timescales. Many factors influence tropical-extratropical teleconnections including the global mean state (i.e., its static stability and winds) and the nature of the tropical heating. Climate change simulations do not agree on how some of these features will change under global warming, and do not agree on how the MJO teleconnection will change over many parts of the extratropics, which makes constraining and understanding the future change to the MJO teleconnection a particular challenge.

Motivated by a desire to untangle the impacts of individual changes to features of the climate on changes to the MJO teleconnection with warming, I conduct a set of sensitivity experiments with a linear baroclinic model of the atmosphere. In each experiment, a climate feature is perturbed by an amount that is informed by end-of-century estimates in climate simulations with strong CO₂ forcing (RCP8.5). Specifically, I test sensitivity to the basic state static stability and winds, and MJO eastward propagation extent, propagation speed, and heating intensity. For an ensemble of January mean states given by the Community Earth System Model (CESM) Large Ensemble (LE), and using an idealized propagating thermal forcing, I find that over the North Pacific and North American region, the largest changes in MJO impacts are from mean state changes, rather than changes to MJO characteristics. Consistent with previous work, I find that the increase of the dry static stability in the tropics with warming leads to weaker teleconnections. Conversely, I find that the change to the mean state winds simulated in the CESM-LE leads to stronger teleconnections. This increase does not appear to be related to differences in Rossby wave excitation, and is likely related to changes in Rossby wave propagation between the climates.

Comparatively, end-of-century perturbations to the MJO lead to much smaller changes in the simulated MJO teleconnection than changes to the mean state. When the MJO is perturbed in isolation, I find that changes to the MJO's speed lead to a shift of the MJO teleconnection pattern rather than an overall increase or decrease in the magnitude of the response to MJO heating. Addi-

tionally, while an increase of the magnitude and eastward extent of the MJO's heating at the upper bound of what is expected to occur in a future climate indeed drives an increase in the magnitude of the MJO teleconnection, it is still much weaker than the increase that was found here due to changes to the mean state winds.

The competing impacts of changes to the mean state static stability and winds may contribute to why the changes to the magnitude of MJO impacts over the North Pacific and North American region are uncertain amongst models (W. Zhou et al., 2020). Despite a weakening tendency from increases in static stability, here I show that the change to the mean state winds are sufficient to offset this weakening, and perhaps may even lead to a strengthening of the MJO teleconnection. The increase of the tropical dry static stability is driven by shifts in thermodynamic balance and will generally be uniform throughout the tropics because of weak tropical temperature gradients. This makes confidence in this particular response of the climate to increasing greenhouse gas concentrations quite high. On the other hand, Rossby wave propagation is very sensitive to the mean state winds. Small differences in the mean state, for example, that between the climatologies of July and August (Yun et al., 2011), or between El Niño and La Niña years (Tseng et al., 2020), lead to large differences in the response to tropical forcing. It is likely that future projections of the MJO teleconnection will be sensitive to the combination of changes to the MJO and basic state winds. In addition, it is likely that current model spread in future projections of the MJO teleconnection is a result of model spread in the combination of future representations of the basic state winds and to the MJO in the warmer climate.

Here I have used a linear model to explore how the MJO teleconnection responds to changes in the mean state and to the MJO itself. While this permits a straightforward diagnosis of causal relationships, the linear framework is missing nonlinear relationships between the mean state and the MJO forcing. For example, the mean state exerts a strong control on MJO propagation characteristics (Jiang et al., 2020). The MJO may also play an active role in shaping the midlatitude mean state winds, for example through the modulation of the local Hadley cell (Lyu et al., 2019). Such feedbacks are not simulated in the LBM. Nonetheless, previous work has shown that the MJO

teleconnection is, to first order, linear (Mori & Watanabe, 2008). Additionally, I believe that this work is a compelling first step towards understanding the intriguing model spread in future MJO teleconnection strength in the extratropics.

Chapter 6

Conclusions

In this dissertation, I explored the impact of the Madden-Julian Oscillation (MJO) on the current and future climate. In Chapter 2, I developed an index to quantify the impact of the MJO on a remote region, and used it to quantify the seasonality and regionality of the MJO's impact over North American temperature in Chapter 3.

In a future warmer climate, the MJO teleconnection may change, in part due to a weakening of the tropical circulation and of the tropical convective mass flux. In Chapter 4, I used energy and mass balance arguments to demonstrate how the strength of the tropical mean circulation is related to the relative heating and cooling rates between convective and clear tropical regions. In Chapter 5, I used a linear baroclinic model to quantify the sensitivity of the MJO teleconnection to this weakening of the tropical circulation, and to other basic state and MJO changes.

The STRIPES index developed in Chapter 2 quantifies the magnitude and consistency of the MJO signal at a point, and is a powerful tool that condenses, into a single number, the information that would otherwise be obtained through many maps of composites. It allows a user to concisely highlight areas of greatest MJO impact, and thus has an advantage over other methods because it does not compromise richness of information for human interpretability.

One of the interesting results of this study was the finding that the MJO signal is detectable in the time series of temperature and precipitation of many of the weather stations across North America. This is interesting for two main reasons. First, previous studies looking at the MJO's impact over the extratropics have used gridded reanalysis products, where data represent averages over large areas. Because of this area-averaging, the time series of temperature and precipitation for grid cells in these types of products is much smoother than what is typical for a weather station. This makes the detection of the MJO signal an easier task. Second, the human experience of weather happens at point locations. The fact that the MJO signal is detectable for point observations makes it more applicable to society.

The STRIPES index has many potential applications. For example, in Chapter 3 I used the index to show that the MJO's impact over North America has seasonality and regionality. In Chapter 5, I used STRIPES to quantify the strength and change of the MJO teleconnection in a global climate model. Beyond my work, it has also already been used in other studies, such as Mayer and Barnes (2020), where it is used to assess the the MJO teleconnection in numerical hindcasts. This index could also be used to help motivate the development of statistical forecast models for regions where numerical forecast models struggle to simulate observed teleconnections, or to concisely perform a climate model intercomparison of the simulated MJO teleconnection. Finally, this index is not limited to the MJO. It can be used for any periodic phenomenon that is characterized by somewhat smoothly periodic behavior, such as the Quasi-Biennial Oscillation or the 11-year solar cycle.

In Chapter 4, I developed a simple diagnostic that links the area fraction of ascending motion to heating rates over convective and clear regions. I showed that it worked well for idealized global tropics simulations, and used it to explain, from an energy and mass balance perspective, how the area fraction of large-scale rising motion and the strength of the mean tropical overturning circulation depend on heating rates due to radiative and convective processes. This diagnostic relied on two key assumptions that make it less applicable to the real world: weak temperature gradients and mass balance. In the tropics, the first of these two assumptions is quite reasonable, especially on time scales longer than a few hours and away from the surface. To the extent that mass balance is also a reasonable assumption (which depends on the phenomenon), the framework laid out in this chapter may also be used to investigate tropical phenomena of the physical earth. For example, this framework may be useful in understanding the mechanisms driving variability in convective clustering along the Intertropical Convergence Zone.

In this work, I have used energy and mass balance arguments to show why the global mean mean circulation weakens with warming. An important next step in this line of research is developing a better understanding of how these broad changes will manifest on smaller scales. One of the results of Chapter 4 showed that despite a simulated monotonic decrease of the global mean

convective mass flux, the change to the region-specific convective mass flux did not always follow the same trend. For example, between the simulations with sea surface temperatures of 295 K and 300 K, the convective mass flux of the most deeply convective regions *increased*. This shows that there is clearly at least one additional degree of freedom in the regional expression of large-scale changes. This is an important result, because it suggests that caution is needed before concluding that a weakening of the global mean convective mass flux directly implies a weakening of the most intense convective systems. Additionally, it is proof that the framework used in Chapter 4 is insufficient for investigating these regional changes to convective behavior with warming. An important consideration is whether there does indeed exist any physical constraint on these regional scales. This remains to be determined.

Lastly, in Chapter 5, I used simulations with a linear model to show that the strongest changes to the January MJO teleconnection with global warming are from mean state changes, rather than changes to MJO intensity or propagation characteristics. However, because of cancellation between the resulting teleconnection change due to competing effects of increased dry static stability and changes to the background winds, the MJO teleconnection change will likely be sensitive to the specific combination of MJO and mean state wind changes. It is plausible that the reason why future projections of the MJO teleconnection strength are not correlated with changes to MJO circulation strength in simulations (W. Zhou et al., 2020) is because of additional contributions from changes in the mean state winds, and to MJO propagation characteristics. One avenue for future work is to investigate this hypothesis. Another possible direction for future work is to repeat this study using the projected future mean state winds of one or many other climate models to determine if the same increase in MJO teleconnection strength over the North Pacific and North America region, and hence cancellation between the competing impacts of mean state changes, results. Lastly, this study was performed for the January mean state. An interesting future direction is to investigate the simulated teleconnection change in climate models during other seasons, and to use these methods to investigate the mechanisms.

References

- Adames, Á. F., Kim, D., Sobel, A. H., Del Genio, A., & Wu, J. (2017). Changes in the structure and propagation of the MJO with increasing CO₂: MJO CHANGES WITH INCREASING CO₂. *J. Adv. Model. Earth Syst.*, *9*(2), 1251–1268. doi: 10.1002/2017MS000913
- Adames, Á. F., & Wallace, J. M. (2014). Three-Dimensional structure and evolution of the MJO and its relation to the mean flow. *J. Atmos. Sci.*, *71*(6), 2007–2026. doi: 10.1175/JAS-D-13-0254.1
- Ahn, M.-S., Kim, D., Sperber, K. R., Kang, I.-S., Maloney, E., Waliser, D., ... on behalf of WGNE MJO Task Force (2017). MJO simulation in CMIP5 climate models: MJO skill metrics and process-oriented diagnosis. *Clim. Dyn.*, *49*(11), 4023–4045. doi: 10.1007/s00382-017-3558-4
- Allen, M. R., & Ingram, W. J. (2002). Constraints on future changes in climate and the hydrologic cycle. *Nature*, *419*(6903), 228.
- Arakawa, A., & Schubert, W. H. (1974). Interaction of a cumulus cloud ensemble with the Large-Scale environment, part I. *J. Atmos. Sci.*, *31*(3), 674–701.
- Baggett, C. F., Barnes, E. A., Maloney, E. D., & Mundhenk, B. D. (2017). Advancing atmospheric river forecasts into subseasonal-to-seasonal time scales: Forecasting ARs at S2S time scales. *Geophys. Res. Lett.*, *44*(14), 7528–7536. doi: 10.1002/2017GL074434
- Baggett, C. F., Nardi, K. M., Childs, S. J., Zito, S. N., Barnes, E. A., & Maloney, E. D. (2018). Skillful subseasonal forecasts of weekly tornado and hail activity using the Madden-Julian oscillation. *J. Geophys. Res. D: Atmos.*, *53*, 1494. doi: 10.1029/2018JD029059
- Barnston, A. G., & Livezey, R. E. (1987). Classification, seasonality and persistence of Low-Frequency atmospheric circulation patterns. *Mon. Weather Rev.*, *115*(6), 1083–1126. doi: 10.1175/1520-0493(1987)115<1083:CSAPOL>2.0.CO;2
- Barrett, B. S. (2019). Connections between the Madden-Julian oscillation and surface temperatures in winter 2018 over eastern north america. *Atmos. Sci. Lett.*, *20*(1), e869. doi: 10.1002/

asl.869

- Baxter, S., Weaver, S., Gottschalck, J., & Xue, Y. (2014). Pentad evolution of wintertime impacts of the Madden–Julian oscillation over the contiguous United States. *J. Clim.*, *27*(19), 7356–7367. doi: 10.1175/JCLI-D-14-00105.1
- Becker, E. J., Berbery, E. H., & Higgins, R. W. (2011). Modulation of cold-season U.S. daily precipitation by the Madden-Julian oscillation. *J. Clim.*, *24*(19), 5157–5166. doi: 10.1175/2011JCLI4018.1
- Betts, A. K. (1998). Climate-Convection feedbacks: Some further issues. *Climatic Change; Dordrecht*, *39*(39), 35–38. doi: 10.1023/A:1005323805826
- Betts, A. K., & Ridgway, W. (1989). Climatic equilibrium of the atmospheric convective boundary layer over a tropical ocean. *J. Atmos. Sci.*, *46*(17), 2621–2641. doi: 10.1175/1520-0469(1989)046<2621:CEOTAC>2.0.CO;2
- Black, J., Johnson, N. C., Baxter, S., Feldstein, S. B., Harnos, D. S., & L’Heureux, M. L. (2017). The predictors and forecast skill of northern hemisphere teleconnection patterns for lead times of 3–4 weeks. *Mon. Weather Rev.*, *145*(7), 2855–2877. doi: 10.1175/MWR-D-16-0394.1
- Bladé, I., & Hartmann, D. L. (1995). The linear and nonlinear extratropical response of the atmosphere to tropical intraseasonal heating. *J. Atmos. Sci.*, *52*(24), 4448–4471. doi: 10.1175/1520-0469(1995)052<4448:TLANER>2.0.CO;2
- Bond, N. A., & Vecchi, G. A. (2003). The influence of the Madden–Julian oscillation on precipitation in Oregon and Washington. *Weather Forecast.*, *18*(4), 600–613. doi: 10.1175/1520-0434(2003)018<0600:TIOTMO>2.0.CO;2
- Bui, H. X., & Maloney, E. D. (2018). Changes in Madden-Julian oscillation precipitation and wind variance under global warming. *Geophys. Res. Lett.*
- Bui, H. X., & Maloney, E. D. (2019a). Mechanisms for global warming impacts on Madden–Julian oscillation precipitation amplitude. *J. Clim.*, *32*(20), 6961–6975. doi: 10.1175/JCLI-D-19-0051.1

- Bui, H. X., & Maloney, E. D. (2019b). Transient response of MJO precipitation and circulation to greenhouse gas forcing. *Geophys. Res. Lett.*, *7*, 847. doi: 10.1029/2019GL085328
- Byrne, M. P., Pendergrass, A. G., Rapp, A. D., & Wodzicki, K. R. (2018). Response of the intertropical convergence zone to climate change: Location, width, and strength. *Curr Clim Change Rep*, *4*(4), 355–370. doi: 10.1007/s40641-018-0110-5
- Byrne, M. P., & Schneider, T. (2016a). Energetic constraints on the width of the intertropical convergence zone. *J. Clim.*, *29*(13), 4709–4721. doi: 10.1175/JCLI-D-15-0767.1
- Byrne, M. P., & Schneider, T. (2016b). Narrowing of the ITCZ in a warming climate: Physical mechanisms: NARROWING ITCZ: PHYSICAL MECHANISMS. *Geophys. Res. Lett.*, *43*(21), 11,350–11,357. doi: 10.1002/2016GL070396
- Cassou, C. (2008). Intraseasonal interaction between the Madden-Julian oscillation and the north atlantic oscillation. *Nature*, *455*(7212), 523–527. doi: 10.1038/nature07286
- Chang, C.-W. J., Tseng, W.-L., Hsu, H.-H., Keenlyside, N., & Tsuang, B.-J. (2015). The Madden-Julian oscillation in a warmer world. *Geophys. Res. Lett.*, *42*(14), 6034–6042.
- Charney, J. G. (1963). A note on large-scale motions in the tropics. *Journal of the Atmospheric Sciences*, *20*(6), 607–609.
- Chikira, M. (2014). Eastward-Propagating intraseasonal oscillation represented by Chikira–Sugiyama cumulus parameterization. part II: Understanding moisture variation under weak temperature gradient balance. *J. Atmos. Sci.*, *71*(2), 615–639. doi: 10.1175/JAS-D-13-038.1
- Chou, C., & Chen, C.-A. (2010). Depth of convection and the weakening of tropical circulation in global warming. *J. Clim.*, *23*(11), 3019–3030. doi: 10.1175/2010JCLI3383.1
- Chou, C., Chen, C.-A., Tan, P.-H., & Chen, K. T. (2012). Mechanisms for global warming impacts on precipitation frequency and intensity. *J. Clim.*, *25*(9), 3291–3306. doi: 10.1175/JCLI-D-11-00239.1
- Chou, C., & Neelin, J. D. (2004). Mechanisms of global warming impacts on regional tropical precipitation. *J. Clim.*, *17*(13), 2688–2701. doi: 10.1175/1520-0442(2004)017<2688:MOGWIO>2.0.CO;2

- Curtis, S. (2017). The Madden-Julian oscillation: A tool for regional seasonal precipitation outlooks? *Atmosphere*, 8(9), 180. doi: 10.3390/atmos8090180
- Curtis, S., & Gamble, D. W. (2016). The boreal winter Madden-Julian oscillation's influence on summertime precipitation in the greater caribbean. *J. Geophys. Res. D: Atmos.*, 121(13), 7592–7605.
- Del Genio, A. D., Yao, M.-S., & Jonas, J. (2007). Will moist convection be stronger in a warmer climate?: CONVECTION STRENGTH IN a WARMER CLIMATE. *Geophys. Res. Lett.*, 34(16), 1086. doi: 10.1029/2007GL030525
- DelSole, T., Trenary, L., Tippet, M. K., & Pegion, K. (2017). Predictability of week-3–4 average temperature and precipitation over the contiguous united states. *J. Clim.*, 30(10), 3499–3512. doi: 10.1175/JCLI-D-16-0567.1
- Diao, Y., Li, T., & Hsu, P. C. (2018). Influence of the boreal summer intraseasonal oscillation on extreme temperature events in the northern hemisphere. *J. Meteorol. Res.*
- Donald, A., Meinke, H., Power, B., Maia, A. d. H. N., Wheeler, M. C., White, N., . . . Ribbe, J. (2006). Near-global impact of the Madden-Julian oscillation on rainfall. *Geophys. Res. Lett.*, 33(9), L09704. doi: 10.1029/2005GL025155
- Ferranti, L., Palmer, T. N., Molteni, F., & Klinker, E. (1990). Tropical-Extratropical interaction associated with the 30–60 day oscillation and its impact on medium and extended range prediction. *J. Atmos. Sci.*, 47(18), 2177–2199. doi: 10.1175/1520-0469(1990)047<2177:TEIAWT>2.0.CO;2
- Fischer, E. M., & Knutti, R. (2016). Observed heavy precipitation increase confirms theory and early models. *Nat. Clim. Chang.*, 6(11), 986–991. doi: 10.1038/nclimate3110
- Frierson, D. M. W. (2006, December). Robust increases in midlatitude static stability in simulations of global warming. *Geophys. Res. Lett.*, 33(24), L02705. doi: 10.1029/2006GL027504
- Garfinkel, C. I., Feldstein, S. B., Waugh, D. W., Yoo, C., & Lee, S. (2012). Observed connection between stratospheric sudden warmings and the Madden-Julian oscillation: MJO AND

- SSW. *Geophys. Res. Lett.*, 39(18), 30,937. doi: 10.1029/2012GL053144
- Gensini, V. A., Gold, D., Allen, J. T., & Barrett, B. S. (2019). Extended US tornado outbreak during late may 2019: A forecast of opportunity. *Geophys. Res. Lett.*, 46(16), 10150–10158.
- Ghil, M., & Mo, K. (1991). Intraseasonal oscillations in the global atmosphere. part i: Northern hemisphere and tropics. *J. Atmos. Sci.*, 48(5), 752–779. doi: 10.1175/1520-0469(1991)048<0752:IOITGA>2.0.CO;2
- Goss, M., & Feldstein, S. B. (2015). The impact of the initial flow on the extratropical response to Madden–Julian oscillation convective heating. *Mon. Weather Rev.*, 143(4), 1104–1121. doi: 10.1175/MWR-D-14-00141.1
- Grabowski, W. W. (2001). Coupling cloud processes with the Large-Scale dynamics using the Cloud-Resolving convection parameterization (CRCP). *J. Atmos. Sci.*, 58(9), 978–997. doi: 10.1175/1520-0469(2001)058<0978:CCPWTLL>2.0.CO;2
- Guo, Y., Shinoda, T., Lin, J., & Chang, E. K. M. (2017). Variations of northern hemisphere storm track and extratropical cyclone activity associated with the Madden–Julian oscillation. *J. Clim.*, 30(13), 4799–4818. doi: 10.1175/JCLI-D-16-0513.1
- Gutzler, D. S., & Madden, R. A. (1989). Seasonal variations in the spatial structure of intraseasonal tropical wind fluctuations. *J. Atmos. Sci.*, 46(5), 641–660. doi: 10.1175/1520-0469(1989)046<0641:SVITSS>2.0.CO;2
- Hartmann, D. L. (1994). *Global physical climatology*. Academic Press.
- He, J., Lin, H., & Wu, Z. (2011). Another look at influences of the Madden-Julian oscillation on the wintertime east asian weather. *J. Geophys. Res. D: Atmos.*, 116(3), 1–18. doi: 10.1029/2010JD014787
- Held, I. M., & Soden, B. J. (2006). Robust responses of the hydrological cycle to global warming. *J. Clim.*, 19(21), 5686–5699. doi: 10.1175/JCLI3990.1
- Henderson, S. A., & Maloney, E. D. (2018). The impact of the Madden–Julian oscillation on High-Latitude winter blocking during el niño–southern oscillation events. *J. Clim.*, 31(13), 5293–5318. doi: 10.1175/JCLI-D-17-0721.1

- Henderson, S. A., Maloney, E. D., & Barnes, E. A. (2016). The influence of the Madden–Julian oscillation on northern hemisphere winter blocking. *J. Clim.*, *29*(12), 4597–4616. doi: 10.1175/JCLI-D-15-0502.1
- Henderson, S. A., Maloney, E. D., & Son, S. W. (2017). Madden-Julian oscillation pacific teleconnections: The impact of the basic state and MJO representation in general circulation models. *J. Clim.*, *30*(12), 4567–4587. doi: 10.1175/JCLI-D-16-0789.1
- Hendon, H. H., & Salby, M. L. (1994). The life cycle of the Madden–Julian oscillation. *J. Atmos. Sci.*, *51*(15), 2225–2237. doi: 10.1175/1520-0469(1994)051<2225:TLCOTM>2.0.CO;2
- Higgins, R. W., & Mo, K. C. (1997). Persistent north pacific circulation anomalies and the tropical intraseasonal oscillation. *J. Clim.*, *10*(2), 223–244. doi: 10.1175/1520-0442(1997)010<0223:PNPCAA>2.0.CO;2
- Hoskins, B. J. (2013). The potential for skill across the range of the seamless weather-climate prediction problem: A stimulus for our science. *Quart. J. Roy. Meteor. Soc.*, *139*(672), 573–584. doi: 10.1002/qj.1991
- Hoskins, B. J., & Ambrizzi, T. (1993). Rossby wave propagation on a realistic longitudinally varying flow. *J. Atmos. Sci.*, *50*(12), 1661–1671. doi: 10.1175/1520-0469(1993)050<1661:RWPOAR>2.0.CO;2
- Hoskins, B. J., & Karoly, D. J. (1981). The steady linear response of a spherical atmosphere to thermal and orographic forcing. *J. Atmos. Sci.*, *38*(6), 1179–1196. doi: 10.1175/1520-0469(1981)038<1179:TSLROA>2.0.CO;2
- Houze, R. A., Jr. (1977). Structure and dynamics of a tropical squall–line system. *Monthly Weather Review*, *105*(12), 1540–1567.
- Hu, Y., & Fu, Q. (2007). Observed poleward expansion of the hadley circulation since 1979. *Atmos. Chem. Phys.*
- Hudson, D., Marshall, A. G., Alves, O., Young, G., Jones, D., & Watkins, A. (2015). Forewarned is forearmed: Extended-Range forecast guidance of recent extreme heat events in australia. *Weather Forecast.*, *31*(3), 697–711. doi: 10.1175/WAF-D-15-0079.1

- Igel, A. L., Igel, M. R., & van den Heever, S. C. (2015). Make it a double? sobering results from simulations using Single-Moment microphysics schemes. *J. Atmos. Sci.*, 72(2), 910–925. doi: 10.1175/JAS-D-14-0107.1
- James, W. E. (1953). Forecasting ground frost. *Meteorol. Mag.*, 82(969), 91.
- Jenney, A. M., Nardi, K. M., Barnes, E. A., & Randall, D. A. (2019). The seasonality and regionality of MJO impacts on north american temperature. *Geophys. Res. Lett.*, 46(15), 9193–9202. doi: 10.1029/2019GL083950
- Jenney, A. M., Randall, D. A., & Barnes, E. A. (2019). Quantifying regional sensitivities to periodic events: Application to the MJO. *J. Geophys. Res. D: Atmos.*, 44, 7528. doi: 10.1029/2018JD029457
- Jenney, A. M., Randall, D. A., & Barnes, E. A. (2020). Mechanisms driving MJO teleconnection changes with warming. *Weather and Climate Dynamics*.
- Jenney, A. M., Randall, D. A., & Branson, M. D. (2020). Understanding the response of tropical ascent to warming using an energy balance framework. *J. Adv. Model. Earth Syst.*, 12(6), 228. doi: 10.1029/2020MS002056
- Jiang, X., Maloney, E., & Su, H. (2020). Large-scale controls of propagation of the Madden-Julian oscillation. *npj Climate and Atmospheric Science*, 3(1), 1–8. doi: 10.1038/s41612-020-00134-x
- Johansson, Å. (2007). Prediction skill of the NAO and PNA from daily to seasonal time scales. *J. Clim.*, 20(10), 1957–1975. doi: 10.1175/JCLI4072.1
- Johnson, N. C., Collins, D. C., Feldstein, S. B., L'Heureux, M. L., & Riddle, E. E. (2014). Skillful wintertime north american temperature forecasts out to 4 weeks based on the state of ENSO and the MJO*. *Weather Forecast.*, 29(1), 23–38. doi: 10.1175/WAF-D-13-00102.1
- Johnson, N. C., & Feldstein, S. B. (2010). The continuum of north pacific sea level pressure patterns: Intraseasonal, interannual, and interdecadal variability. *J. Clim.*, 23(4), 851–867. doi: 10.1175/2009JCLI3099.1
- Jones, C., & Carvalho, L. M. V. (2014). Sensitivity to Madden–Julian oscillation variations on

- heavy precipitation over the contiguous united states. *Atmos. Res.*, 147-148, 10–26. doi: 10.1016/j.atmosres.2014.05.002
- Jones, C., Gottschalck, J., Carvalho, L. M. V., & Higgins, W. (2011). Influence of the Madden–Julian oscillation on forecasts of extreme precipitation in the contiguous united states. *Mon. Weather Rev.*, 139(2), 332–350. doi: 10.1175/2010MWR3512.1
- Jones, C., Waliser, D. E., Lau, W. K. M., & Stern, W. (2004). Global occurrences of extreme precipitation and the Madden–Julian oscillation: Observations and predictability. *J. Clim.*, 17(23), 4575–4589. doi: 10.1175/3238.1
- Kalnay, E., Kanamitsu, M., Kistler, R., Collins, W., Deaven, D., Gandin, L., . . . Joseph, D. (1996). The NCEP/NCAR 40-year reanalysis project. *Bull. Am. Meteorol. Soc.*, 77(3), 437–472. doi: 10.1175/1520-0477(1996)077<0437:TNYRP>2.0.CO;2
- Kang, W., & Tziperman, E. (2018). The MJO-SSW teleconnection: Interaction between MJO-Forced waves and the midlatitude jet. *Geophys. Res. Lett.*, 45, 4400–4409. doi: 10.1029/2018GL077937
- Karoly, D. J. (1983). Rossby wave propagation in a barotropic atmosphere. *Dyn. Atmos. Oceans*, 7(2), 111–125. doi: 10.1016/0377-0265(83)90013-1
- Kay, J. E., Deser, C., Phillips, A., Mai, A., Hannay, C., Strand, G., . . . Vertenstein, M. (2015). The community earth system model (CESM) large ensemble project : A community resource for studying climate change in the presence of internal climate variability. *Bull. Am. Meteorol. Soc.*, 96(8), 1333–1349. doi: 10.1175/BAMS-D-13-00255.1
- Khairoutdinov, M., Randall, D., & DeMott, C. (2005). Simulations of the atmospheric general circulation using a Cloud-Resolving model as a superparameterization of physical processes. *J. Atmos. Sci.*, 62(7), 2136–2154. doi: 10.1175/JAS3453.1
- Khairoutdinov, M., & Randall, D. A. (2001). A cloud resolving model as a cloud parameterization in the NCAR community climate system model: Preliminary results. *Geophys. Res. Lett.*, 28(18), 3617–3620. doi: 10.1029/2001GL013552
- Khairoutdinov, M., & Randall, D. A. (2003). Cloud resolving modeling of the ARM summer

- 1997 IOP: Model formulation, results, uncertainties, and sensitivities. *J. Atmos. Sci.*, *60*(4), 607–625. doi: 10.1175/1520-0469(2003)060<0607:CRMOTA>2.0.CO;2
- Kiladis, G. N., Dias, J., Straub, K. H., Wheeler, M. C., Tulich, S. N., Kikuchi, K., ... Ventrice, M. J. (2014). A comparison of OLR and Circulation-Based indices for tracking the MJO. *Mon. Weather Rev.*, *142*(5), 1697–1715. doi: 10.1175/MWR-D-13-00301.1
- Knutson, T. R., & Manabe, S. (1995). Time-Mean response over the tropical pacific to increased CO₂ in a coupled Ocean-Atmosphere model. *J. Clim.*, *8*(9), 2181–2199. doi: 10.1175/1520-0442(1995)008<2181:TMROTT>2.0.CO;2
- Knutson, T. R., & Weickmann, K. M. (1987). 30–60 day atmospheric oscillations: Composite life cycles of convection and circulation anomalies. *Monthly Weather Review*, *115*(7), 1407–1436. doi: 10.1175/1520-0493(1987)115<1407:DAOCLC>2.0.CO;2
- Kooperman, G. J., Pritchard, M. S., Burt, M. A., Branson, M. D., & Randall, D. A. (2016). Impacts of cloud superparameterization on projected daily rainfall intensity climate changes in multiple versions of the community earth system model. *Journal of Advances in Modeling Earth Systems*, *8*(4), 1727–1750.
- Lau, W. K. M., & Chan, P. H. (1986). Aspects of the 40–50 day oscillation during the northern summer as inferred from outgoing longwave radiation. *Mon. Weather Rev.*, *114*(7), 1354–1367. doi: 10.1175/1520-0493(1986)114<1354:AOTDOD>2.0.CO;2
- Lau, W. K. M., & Kim, K.-M. (2015). Robust hadley circulation changes and increasing global dryness due to CO₂ warming from CMIP5 model projections. *Proc. Natl. Acad. Sci. U. S. A.*, *112*(12), 3630–3635. doi: 10.1073/pnas.1418682112
- Lau, W. K. M., Wu, H.-T., & Kim, K.-M. (2013). A canonical response of precipitation characteristics to global warming from CMIP5 models: PRECIPITATION AND GLOBAL WARMING. *Geophys. Res. Lett.*, *40*(12), 3163–3169. doi: 10.1002/grl.50420
- Lee, Y.-Y., & Grotjahn, R. (2019). Evidence of specific MJO phase occurrence with summertime california central valley extreme hot weather. *Adv. Atmos. Sci.*, *36*(6), 589–602. doi: 10.1007/s00376-019-8167-1

- Li, X., Tang, Y., Zhou, L., Chen, D., Yao, Z., & Islam, S. U. (2016). Assessment of Madden–Julian oscillation simulations with various configurations of CESM. *Clim. Dyn.*, *47*(7), 2667–2690. doi: 10.1007/s00382-016-2991-0
- Limpasuvan, V., Thompson, D. W. J., & Hartmann, D. L. (2004). The life cycle of the northern hemisphere sudden stratospheric warmings. *J. Clim.*, *17*(13), 2584–2596. doi: 10.1175/1520-0442(2004)017<2584:TLCOTN>2.0.CO;2
- Lin, H. (2009). Global extratropical response to diabatic heating variability of the asian summer monsoon. *J. Atmos. Sci.*, *66*(9), 2697–2713. doi: 10.1175/2009JAS3008.1
- Lin, H., Brunet, G., & Derome, J. (2009). An observed connection between the north atlantic oscillation and the Madden–Julian oscillation. *J. Clim.*, *22*(2), 364–380. doi: 10.1175/2008JCLI2515.1
- Lin, H., Brunet, G., & Fontecilla, J. S. (2010). Impact of the Madden-Julian oscillation on the intraseasonal forecast skill of the north atlantic oscillation. *Geophys. Res. Lett.*, *37*(19). doi: 10.1029/2010GL044315
- Lin, H., Brunet, G., & Mo, R. (2010). Impact of the Madden–Julian oscillation on winter-time precipitation in canada. *Mon. Weather Rev.*, *138*(10), 3822–3839. doi: 10.1175/2010MWR3363.1
- Lorenz, D. J., & Hartmann, D. L. (2006). The effect of the MJO on the north american monsoon. *J. Clim.*, *19*(3), 333–343. doi: 10.1175/JCLI3684.1
- Lu, J., Vecchi, G. A., & Reichler, T. (2007). Expansion of the hadley cell under global warming. *Geophys. Res. Lett.*, *34*(6), 35. doi: 10.1029/2006GL028443
- Lu, W., & Hsu, P. C. (2017). Factors controlling the seasonality of the Madden-Julian oscillation. *Dyn. Atmos. Oceans*, *78*, 106–120. doi: 10.1016/j.dynatmoce.2017.04.002
- Lyu, M., Wu, Z., Shi, X., & Wen, M. (2019). Distinct impacts of the MJO and the NAO on cold wave amplitude in china. *Q.J.R. Meteorol. Soc.*, *145*(721), 1617–1635. doi: 10.1002/qj.3516
- Madden, R. A. (1986). Seasonal variations of the 40-50 day oscillation in the tropics. *J. Atmos.*

- Sci.*, 43(24), 3138–3158.
- Madden, R. A., & Julian, P. R. (1971). Detection of a 40–50 day oscillation in the zonal wind in the tropical pacific. *Journal of the Atmospheric Sciences*, 28(5), 702–708. doi: 10.1175/1520-0469(1971)028<0702:DOADOI>2.0.CO;2
- Madden, R. A., & Julian, P. R. (1972). Description of Global-Scale circulation cells in the tropics with a 40–50 day period. *Journal of the Atmospheric Sciences*, 29(6), 1109–1123. doi: 10.1175/1520-0469(1972)029<1109:DOGSCC>2.0.CO;2
- Maher, P., Vallis, G. K., Sherwood, S. C., Webb, M. J., & Sansom, P. G. (2018). The impact of parameterized convection on climatological precipitation in atmospheric global climate models. *Geophys. Res. Lett.*, 45(8), 3728–3736. doi: 10.1002/2017GL076826
- Maloney, E. D., Adames, Á. F., & Bui, H. X. (2019). Madden–Julian oscillation changes under anthropogenic warming. *Nat. Clim. Chang.*, 9(1), 26–33. doi: 10.1038/s41558-018-0331-6
- Maloney, E. D., & Xie, S.-P. (2013). Sensitivity of tropical intraseasonal variability to the pattern of climate warming: MJO ACTIVITY AND CLIMATE WARMING. *J. Adv. Model. Earth Syst.*, 5(1), 32–47. doi: 10.1029/2012MS000171
- Mariotti, A., Ruti, P. M., & Rixen, M. (2018). Progress in subseasonal to seasonal prediction through a joint weather and climate community effort. *npj Climate and Atmospheric Science*, 1(1), 4. doi: 10.1038/s41612-018-0014-z
- Matsueda, S., & Takaya, Y. (2015). The global influence of the Madden–Julian oscillation on extreme temperature events. *J. Clim.*(February 2008), 150330095237008. doi: 10.1175/JCLI-D-14-00625.1
- Matsumura, S., Ueki, S., & Horinouchi, T. (2019). Contrasting responses of midlatitude jets to the north pacific and north atlantic warming. *Geophys. Res. Lett.*, 46(7), 3973–3981. doi: 10.1029/2019GL082550
- Mayer, K. J., & Barnes, E. A. (2020). Subseasonal midlatitude prediction skill following Quasi-Biennial oscillation and Madden–Julian oscillation activity. *Weather and Climate Dynamics*, 1(1), 247–259.

- McKinnon, K. A., Rhines, A., Tingley, M. P., & Huybers, P. (2016). Long-lead predictions of eastern united states hot days from pacific sea surface temperatures. *Nat. Geosci.*, *9*(5), 389–394. doi: 10.1038/ngeo2687
- Menne, M. J., Durre, I., Vose, R. S., Gleason, B. E., & Houston, T. G. (2012). An overview of the global historical climatology network-daily database. *J. Atmos. Ocean. Technol.*, *29*(7), 897–910. doi: 10.1175/JTECH-D-11-00103.1
- Merlis, T. M. (2015). Direct weakening of tropical circulations from masked CO2 radiative forcing. *Proc. Natl. Acad. Sci. U. S. A.*, *112*(43), 13167–13171. doi: 10.1073/pnas.1508268112
- Mo, K. C. (2000). Intraseasonal modulation of summer precipitation over north america. *Mon. Weather Rev.*, *128*(5), 1490–1505. doi: 10.1175/1520-0493(2000)128<1490:IMOSPO>2.0.CO;2
- Mo, K. C., & Higgins, R. W. (1998). Tropical convection and precipitation regimes in the western united states. *J. Clim.*, *11*(9), 2404–2423.
- Moon, J. Y., Wang, B., & Ha, K. J. (2011). ENSO regulation of MJO teleconnection. *Clim. Dyn.*, *37*(5), 1133–1149. doi: 10.1007/s00382-010-0902-3
- Moon, J.-Y., Wang, B., Ha, K.-J., & Lee, J.-Y. (2013). Teleconnections associated with northern hemisphere summer monsoon intraseasonal oscillation. *Clim. Dyn.*, *40*(11), 2761–2774. doi: 10.1007/s00382-012-1394-0
- Moore, R. W., Martius, O., & Spengler, T. (2010). The modulation of the subtropical and extratropical atmosphere in the pacific basin in response to the Madden–Julian oscillation. *Mon. Weather Rev.*, *138*(7), 2761–2779. doi: 10.1175/2010MWR3194.1
- Mori, M., & Watanabe, M. (2008). The growth and triggering mechanisms of the PNA: A MJO-PNA coherence. *J. Meteorol. Soc. Japan*, *86*(1), 213–236. doi: 10.2151/jmsj.86.213
- Mundhenk, B. D., Barnes, E., Maloney, E., & Baggett, C. (2018). Skillful empirical subseasonal prediction of landfalling atmospheric river activity using the Madden-Julian oscillation and quasi-biennial oscillation. *Nature Clim. and Atmos. Sci.*, *1*. doi: 10.1038/s41612-017-0008

- Mundhenk, B. D., Barnes, E. A., & Maloney, E. D. (2016). All-season climatology and variability of atmospheric river frequencies over the north pacific. *J. Clim.*, *29*(13), 4885–4903. doi: 10.1175/JCLI-D-15-0655.1
- Neelin, J. D., Chou, C., & Su, H. (2003). Tropical drought regions in global warming and el nino teleconnections. *Geophys. Res. Lett.*, *30*(24).
- Newman, M., & Sardeshmukh, P. D. (1998). The impact of the annual cycle on the north Pacific/North american response to remote Low-Frequency forcing. *J. Atmos. Sci.*, *55*(8), 1336–1353. doi: 10.1175/1520-0469(1998)055<1336:TIOTAC>2.0.CO;2
- Pendergrass, A. G., & Gerber, E. P. (2016). The rain is askew: Two idealized models relating vertical velocity and precipitation distributions in a warming world. *J. Clim.*, *29*(18), 6445–6462. doi: 10.1175/JCLI-D-16-0097.1
- Pendergrass, A. G., & Hartmann, D. L. (2014). The atmospheric energy constraint on Global-Mean precipitation change. *J. Clim.*, *27*(2), 757–768. doi: 10.1175/JCLI-D-13-00163.1
- Popp, M., & Bony, S. (2019). Stronger zonal convective clustering associated with a wider tropical rain belt. *Nat. Commun.*, *10*(1), 4261. doi: 10.1038/s41467-019-12167-9
- Ralph, F. M., Neiman, P. J., Kiladis, G. N., & Weickmann, K. (2010). A multiscale observational case study of a pacific atmospheric river exhibiting Tropical–Extratropical connections and a mesoscale frontal wave. *Mon. Weather Rev.*, *139*(4), 1169–1189. doi: 10.1175/2010MWR3596.1
- Randall, D., DeMott, C., Stan, C., Khairoutdinov, M., Benedict, J., McCrary, R., ... Branson, M. (2016). Simulations of the tropical general circulation with a multiscale global model. *Meteorol. Monogr.*, *56*, 15.1–15.15. doi: 10.1175/AMSMONOGRAPHS-D-15-0016.1
- Randall, D., Khairoutdinov, M., Arakawa, A., & Grabowski, W. (2003). Breaking the cloud parameterization deadlock. *Bull. Am. Meteorol. Soc.*, *84*(11), 1547–1564. doi: 10.1175/BAMS-84-11-1547
- Riddle, E. E., Stoner, M. B., Johnson, N. C., L’Heureux, M. L., Collins, D. C., & Feldstein, S. B. (2013). The impact of the MJO on clusters of wintertime circulation anomalies over the

- north american region. *Clim. Dyn.*, *40*(7-8), 1749–1766. doi: 10.1007/s00382-012-1493-y
- Riehl, H., & Malkus, J. (1958). On the heat balance of the equatorial trough zone. *geophysica. Helsinki*, *6*, 3–4.
- Robertson, A. W., Kumar, A., Peña, M., & Vitart, F. (2015). Improving and promoting subseasonal to seasonal prediction. *Bull. Am. Meteorol. Soc.*, *96*(3), ES49–ES53. doi: 10.1175/BAMS-D-14-00139.1
- Rodney, M., Lin, H., & Derome, J. (2013). Subseasonal prediction of wintertime north american surface air temperature during strong MJO events. *Mon. Weather Rev.*, *141*(8), 2897–2909. doi: 10.1175/MWR-D-12-00221.1
- Romps, D. M., & Kuang, Z. (2010). Do undiluted convective plumes exist in the upper tropical troposphere? *J. Atmos. Sci.*, *67*(2), 468–484. doi: 10.1175/2009JAS3184.1
- Roundy, P. E., MacRitchie, K., Asuma, J., & Melino, T. (2010). Modulation of the global atmospheric circulation by combined activity in the Madden-Julian oscillation and the el niño-southern oscillation during boreal winter. *J. Clim.*, *23*(15), 4045–4059. doi: 10.1175/2010JCLI3446.1
- Rushley, S. S., Kim, D., & Adames, Á. F. (2019). Changes in the MJO under greenhouse Gas–Induced warming in CMIP5 models. *J. Clim.*, *32*(3), 803–821. doi: 10.1175/JCLI-D-18-0437.1
- Salby, M. L., & Hendon, H. H. (1994). Intraseasonal behavior of clouds, temperature, and motion in the tropics. *Journal of the Atmospheric Sciences*, *51*(15), 2207–2224. doi: 10.1175/1520-0469(1994)051<2207:IBOCTA>2.0.CO;2
- Sardeshmukh, P. D., & Hoskins, B. J. (1988). The generation of global rotational flow by steady idealized tropical divergence. *Journal of the Atmospheric Sciences*, *45*(7), 1228–1251. doi: 10.1175/1520-0469(1988)045<1228:TGOGRF>2.0.CO;2
- Schiro, K. A., Su, H., Wang, Y., Langenbrunner, B., Jiang, J. H., & Neelin, J. D. (2019). Relationships between tropical ascent and high cloud fraction changes with warming revealed by perturbation physics experiments in CAM5. *Geophys. Res. Lett.*, *46*(16), 10112–10121. doi:

10.1029/2019GL083026

- Schneider, T., O’Gorman, P. A., & Levine, X. J. (2010). WATER VAPOR AND THE DYNAMICS OF CLIMATE CHANGES. *Rev. Geophys.*, *48*(3), D22104. doi: 10.1029/2009RG000302
- Schreck, C. J., Cordeira, J. M., & Margolin, D. (2013). Which MJO events affect north american temperatures? *Mon. Weather Rev.*, *141*(11), 3840–3850. doi: 10.1175/MWR-D-13-00118.1
- Seager, R., Naik, N., & Vecchi, G. A. (2010). Thermodynamic and dynamic mechanisms for Large-Scale changes in the hydrological cycle in response to global warming. *J. Clim.*, *23*(17), 4651–4668. doi: 10.1175/2010JCLI3655.1
- Seo, K.-H., & Lee, H.-J. (2017). Mechanisms for a PNA-Like teleconnection pattern in response to the MJO. *J. Atmos. Sci.*, *74*(6), 1767–1781. doi: 10.1175/JAS-D-16-0343.1
- Seo, K.-H., Lee, H.-J., & Frierson, D. M. W. (2016). Unraveling the teleconnection mechanisms that induce wintertime temperature anomalies over the northern hemisphere continents in response to the MJO. *J. Atmos. Sci.*, *73*(9), 3557–3571. doi: 10.1175/JAS-D-16-0036.1
- Seo, K.-H., & Son, S.-W. (2012). The global atmospheric circulation response to tropical diabatic heating associated with the Madden–Julian oscillation during northern winter. *J. Atmos. Sci.*, *69*(1), 79–96. doi: 10.1175/2011JAS3686.1
- Simmons, A. J., Wallace, J. M., & Branstator, G. W. (1983). Barotropic wave propagation and instability, and atmospheric teleconnection patterns. *Journal of the Atmospheric Sciences*, *40*(6), 1363–1392. doi: 10.1175/1520-0469(1983)040<1363:BWPAIA>2.0.CO;2
- Singh, M. S., & O’Gorman, P. A. (2015). Increases in moist-convective updraught velocities with warming in radiative-convective equilibrium: Increases in updraught velocities with warming. *Q.J.R. Meteorol. Soc.*, *141*(692), 2828–2838. doi: 10.1002/qj.2567
- Slade, S. A., & Maloney, E. D. (2013). An intraseasonal prediction model of atlantic and east pacific tropical cyclone genesis. *Mon. Weather Rev.*, *141*(6), 1925–1942. doi: 10.1175/MWR-D-12-00268.1
- Sobel, A. H., & Bretherton, C. S. (2000). Modeling tropical precipitation in a single column. *J. Clim.*, *13*(24), 4378–4392. doi: 10.1175/1520-0442(2000)013<4378:MTPIAS>2.0.CO;2

- Sobel, A. H., Nilsson, J., & Polvani, L. M. (2001). The weak temperature gradient approximation and balanced tropical moisture waves. *J. Atmos. Sci.*, *58*(23), 3650–3665. doi: 10.1175/1520-0469(2001)058<3650:TWTGAA>2.0.CO;2
- Son, S.-W., Lim, Y., Yoo, C., Hendon, H. H., & Kim, J. (2017). Stratospheric control of the Madden–Julian oscillation. *J. Clim.*, *30*(6), 1909–1922. doi: 10.1175/JCLI-D-16-0620.1
- Stan, C., Straus, D. M., Frederiksen, J. S., Lin, H., Maloney, E. D., & Schumacher, C. (2017). Review of Tropical-Extratropical teleconnections on intraseasonal time scales: The subseasonal to seasonal (S2S) teleconnection Sub-Project. *Rev. Geophys.*, *55*(4), 902–937. doi: 10.1002/2016RG000538
- Stevens, B., Satoh, M., Auger, L., Biercamp, J., Bretherton, C. S., Chen, X., ... others (2019). Dyamond: the dynamics of the atmospheric general circulation modeled on non-hydrostatic domains. *Progress in Earth and Planetary Science*, *6*(1), 61.
- Su, H., Jiang, J. H., Neelin, J. D., Shen, T. J., Zhai, C., Yue, Q., ... Yung, Y. L. (2017). Tightening of tropical ascent and high clouds key to precipitation change in a warmer climate. *Nat. Commun.*, *8*, 15771. doi: 10.1038/ncomms15771
- Su, H., Zhai, C., Jiang, J. H., Wu, L., Neelin, J. D., & Yung, Y. L. (2019). A dichotomy between model responses of tropical ascent and descent to surface warming. *npj Climate and Atmospheric Science*, *2*(1), 8. doi: 10.1038/s41612-019-0066-8
- Subramanian, A., Jochum, M., Miller, A. J., Neale, R., Seo, H., Waliser, D., & Murtugudde, R. (2014). The MJO and global warming: A study in CCSM4. *Clim. Dyn.*, *42*(7-8), 2019–2031. doi: 10.1007/s00382-013-1846-1
- Sun, Y., Solomon, S., Dai, A., & Portmann, R. W. (2007). How often will it rain? *J. Clim.*, *20*(19), 4801–4818. doi: 10.1175/JCLI4263.1
- Ting, M., & Sardeshmukh, P. D. (1993). Factors determining the extratropical response to equatorial diabatic heating anomalies. *J. Atmos. Sci.*, *50*(6), 907–918. doi: 10.1175/1520-0469(1993)050<0907:FDTERT>2.0.CO;2
- Tippett, M. K. (2018). Robustness of relations between the MJO and U.S. tornado occurrence.

- Mon. Weather Rev.*, 146(11), 3873–3884. doi: 10.1175/MWR-D-18-0207.1
- Tseng, K.-C., Maloney, E., & Barnes, E. (2019). The consistency of MJO teleconnection patterns: An explanation using linear rossby wave theory. *J. Clim.*, 32(2), 531–548. doi: 10.1175/JCLI-D-18-0211.1
- Tseng, K.-C., Maloney, E., & Barnes, E. A. (2020). The consistency of MJO teleconnection patterns on interannual time scales. *J. Clim.*, 33(9), 3471–3486. doi: 10.1175/JCLI-D-19-0510.1
- Vecchi, G. A., & Soden, B. J. (2007). Global warming and the weakening of the tropical circulation. *J. Clim.*, 20(17), 4316–4340. doi: 10.1175/JCLI4258.1
- Vitart, F., Ardilouze, C., Bonet, A., Brookshaw, A., Chen, M., Codorean, C., . . . Zhang, L. (2017). The subseasonal to seasonal (S2S) prediction project database. *Bull. Am. Meteorol. Soc.*, 98(1), 163–173. doi: 10.1175/BAMS-D-16-0017.1
- Vitart, F., & Molteni, F. (2010). Simulation of the madden-julian oscillation and its teleconnections in the ECMWF forecast system. *Q.J.R. Meteorol. Soc.*, 136(649), 842–855. doi: 10.1002/qj.623
- Wang, B., & Rui, H. (1990). Synoptic climatology of transient tropical intraseasonal convection anomalies: 1975-1985. *Meteorol. Atmos. Phys.*, 44(1), 43–61. doi: 10.1007/BF01026810
- Wang, B., & Xie, X. (1997). A model for the boreal summer intraseasonal oscillation. *J. Atmos. Sci.*, 54(1), 72–86. doi: 10.1175/1520-0469(1997)054<0072:AMFTBS>2.0.CO;2
- Wang, L., Li, T., Zhou, T., & Rong, X. (2013). Origin of the intraseasonal variability over the north pacific in boreal summer. *J. Clim.*, 26(4), 1211–1229. doi: 10.1175/JCLI-D-11-00704.1
- Wang, S., Ma, D., Sobel, A. H., & Tippet, M. K. (2018). Propagation characteristics of BSISO indices. *Geophys. Res. Lett.*. doi: 10.1029/2018GL078321
- Watanabe, M., & Kimoto, M. (2000). Atmosphere-ocean thermal coupling in the north atlantic: A positive feedback. *Q.J Royal Met. Soc.*, 126(570), 3343–3369. doi: 10.1002/qj.49712657017
- Wheeler, M. C., & Hendon, H. H. (2004). An All-Season Real-Time multivariate MJO index:

- Development of an index for monitoring and prediction. *Mon. Weather Rev.*, 132(8), 1917–1932. doi: 10.1175/1520-0493(2004)132<1917:AARMMI>2.0.CO;2
- White, C. J., Carlsen, H., Robertson, A. W., Klein, R. J. T., Lazo, J. K., Kumar, A., ... Zebiak, S. E. (2017). Potential applications of subseasonal-to-seasonal (S2S) predictions. *Meteorol. Appl.*, 24(3), 315–325. doi: 10.1002/met.1654
- Wing, A. A., Reed, K. A., Satoh, M., Stevens, B., Bony, S., & Ohno, T. (2018). Radiative–convective equilibrium model intercomparison project. *Geoscientific Model Development*, 11(2), 793–813. doi: 10.5194/gmd-11-793-2018
- Wing, A. A., Stauffer, C. L., Becker, T., Reed, K. A., Ahn, M., Arnold, N. P., ... Zhao, M. (2020). Clouds and convective Self-Aggregation in a Multi-Model ensemble of Radiative-Convective equilibrium simulations. *J. Adv. Model. Earth Syst.*. doi: 10.1029/2020MS002138
- Wodzicki, K. R., & Rapp, A. D. (2016). Long-term characterization of the pacific ITCZ using TRMM, GPCP, and ERA-Interim: PACIFIC ITCZ CHARACTERIZATION. *J. Geophys. Res. D: Atmos.*, 121(7), 3153–3170. doi: 10.1002/2015JD024458
- Wolding, B. O., Maloney, E. D., & Branson, M. (2016). Vertically resolved weak temperature gradient analysis of the Madden-Julian oscillation in SP-CESM: WTG ANALYSIS OF THE MJO IN SP-CESM. *J. Adv. Model. Earth Syst.*, 8(4), 1586–1619. doi: 10.1002/2016MS000724
- Wolding, B. O., Maloney, E. D., Henderson, S., & Branson, M. (2017). Climate change and the Madden-Julian oscillation: A vertically resolved weak temperature gradient analysis: CLIMATE CHANGE AND THE MJO. *Journal of Advances in Modeling Earth Systems*, 9(1), 307–331. doi: 10.1002/2016MS000843
- Xu, K.-M., & Emanuel, K. A. (1989, July). Is the tropical atmosphere conditionally unstable? *Mon. Weather Rev.*, 117(7), 1471–1479. doi: 10.1175/1520-0493(1989)117<1471:ITTACU>2.0.CO;2
- Yasunari, T. (1979). Cloudiness fluctuations associated with the northern hemisphere summer

- monsoon. *Journal of the Meteorological Society of Japan. Ser. II*, 57(3), 227–242. doi: 10.2151/jmsj1965.57.3_227
- Yun, K.-S., Kim, S.-Y., Ha, K.-J., & Watanabe, M. (2011). Effects of subseasonal basic state changes on rossby wave propagation during northern summer: BASIC STATE EFFECT ON ROSSBY WAVES. *J. Geophys. Res.*, 116(D24). doi: 10.1029/2011JD016258
- Zhang, C. (2013). Madden-Julian oscillation: Bridging weather and climate. *Bull. Am. Meteorol. Soc.*, 94(12), 1849–1870. doi: 10.1175/BAMS-D-12-00026.1
- Zheng, C., Kar-Man Chang, E., Kim, H.-M., Zhang, M., & Wang, W. (2018). Impacts of the Madden–Julian oscillation on Storm-Track activity, surface air temperature, and precipitation over north america. *J. Clim.*, 31(15), 6113–6134. doi: 10.1175/JCLI-D-17-0534.1
- Zhou, S., L’Heureux, M., Weaver, S., & Kumar, A. (2012). A composite study of the MJO influence on the surface air temperature and precipitation over the continental united states. *Clim. Dyn.*, 38(7-8), 1459–1471. doi: 10.1007/s00382-011-1001-9
- Zhou, W., Yang, D., Xie, S.-P., & Ma, J. (2020). Amplified Madden–Julian oscillation impacts in the Pacific–North america region. *Nat. Clim. Chang.*. doi: 10.1038/s41558-020-0814-0
- Zhu, Z., & Li, T. (2017). The statistical extended-range (10–30-day) forecast of summer rainfall anomalies over the entire china. *Clim. Dyn.*, 48(1), 209–224. doi: 10.1007/s00382-016-3070

Appendix A

Supplemental figures

The figures included here are intended to support the main text. Figures A.1-A.3 are the same as main text Figure 2.3a, but use MJO days that are not independent. Figures A.4-A.6 are the same as main text Figure 2.3a, but do not have the adjustments described in the main text to remove minor sensitivities; i.e, phases are ordered from 1-8 and not shifted, and only a slope of 6 days per phase is used to calculate the STRIPES index. Figure A.7 is the same as the main text Figure 2.6 but for precipitable water, where units are mm day^{-1} .

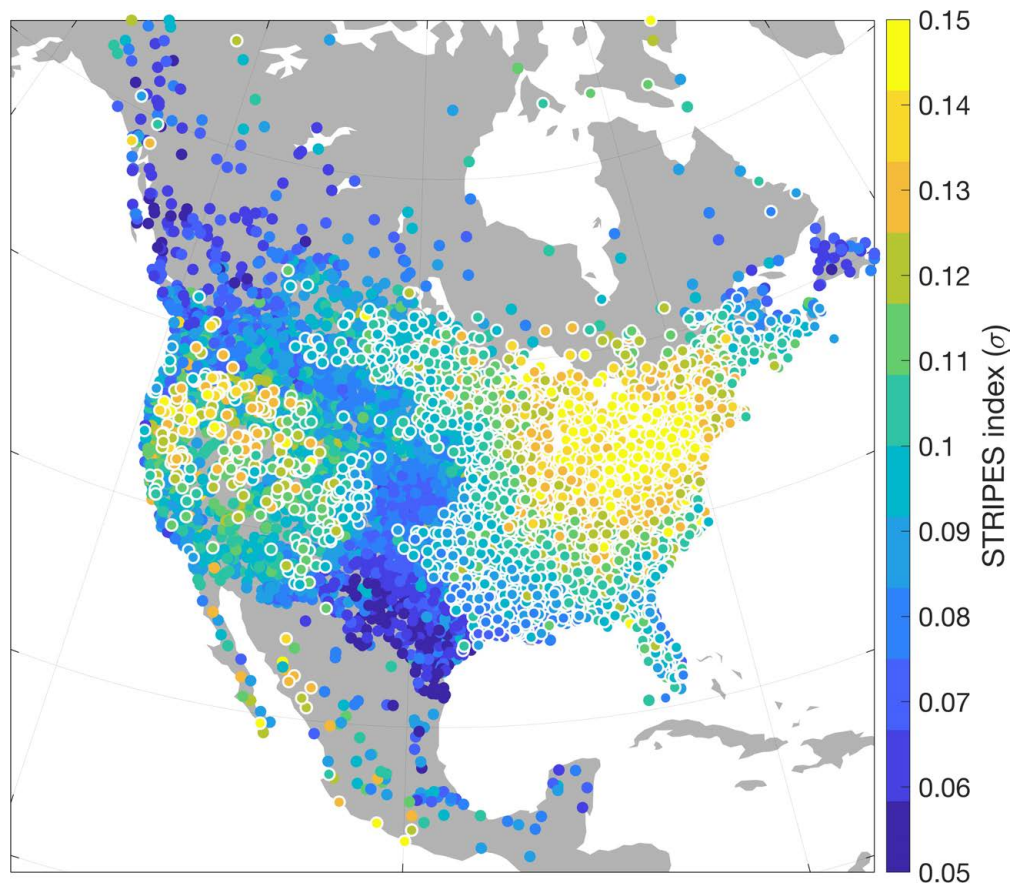


Figure A.1: STRIPES index for North American weather stations (each point on the map is a unique weather station) for daily maximum temperature (TMAX) after the MJO for the years 1974-2017. Days used in the calculation of the STRIPES index are not independent (see main text for more information).

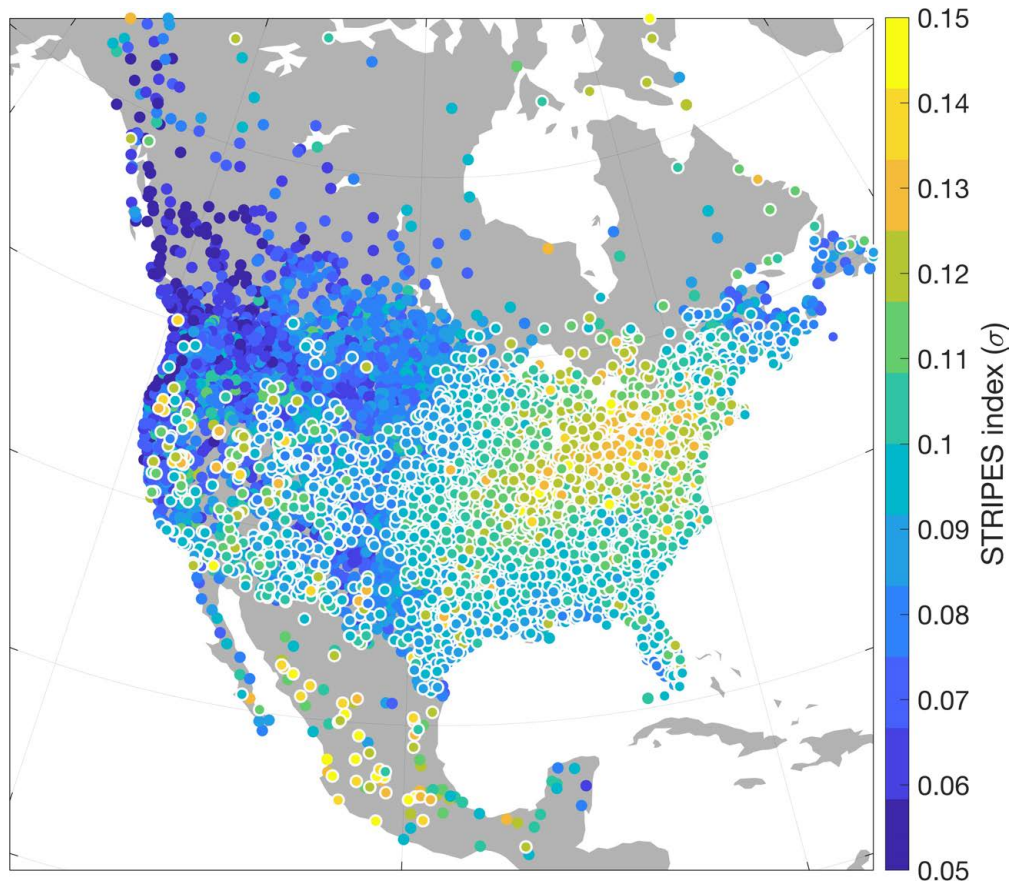


Figure A.2: As in A.1 but for daily minimum temperature (TMIN).

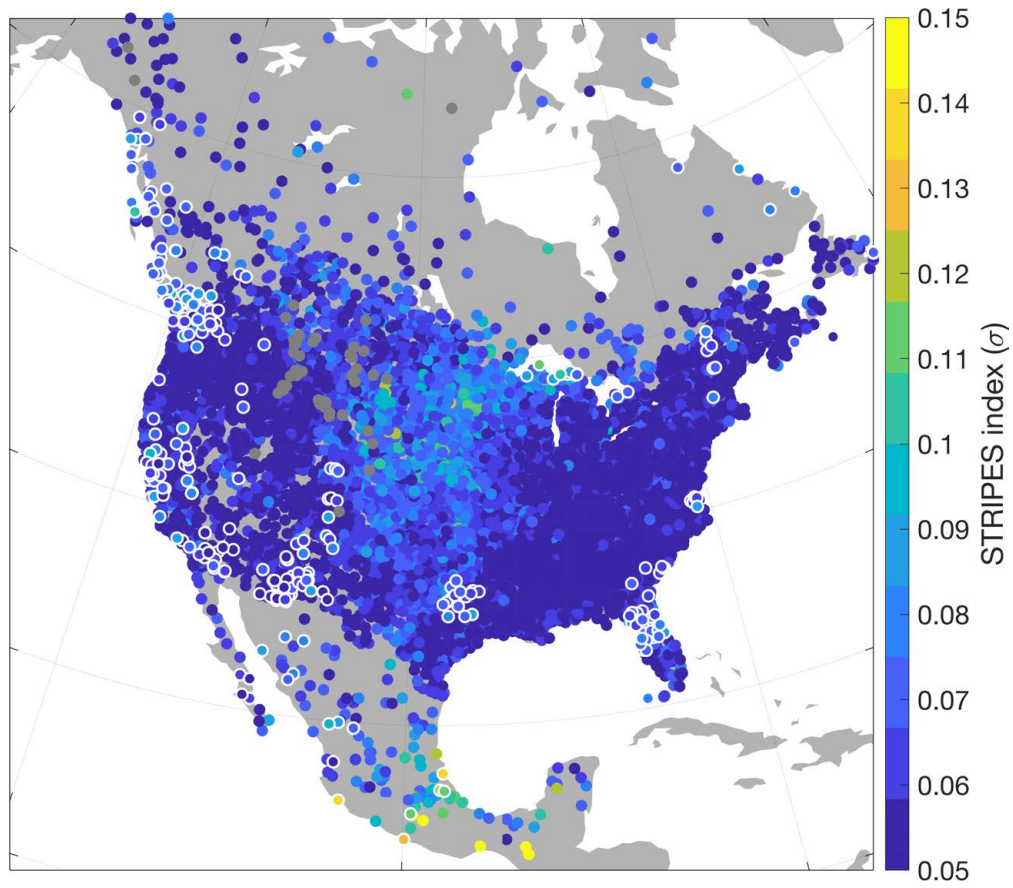


Figure A.3: As in A.1 but for daily precipitation totals (PRCP).

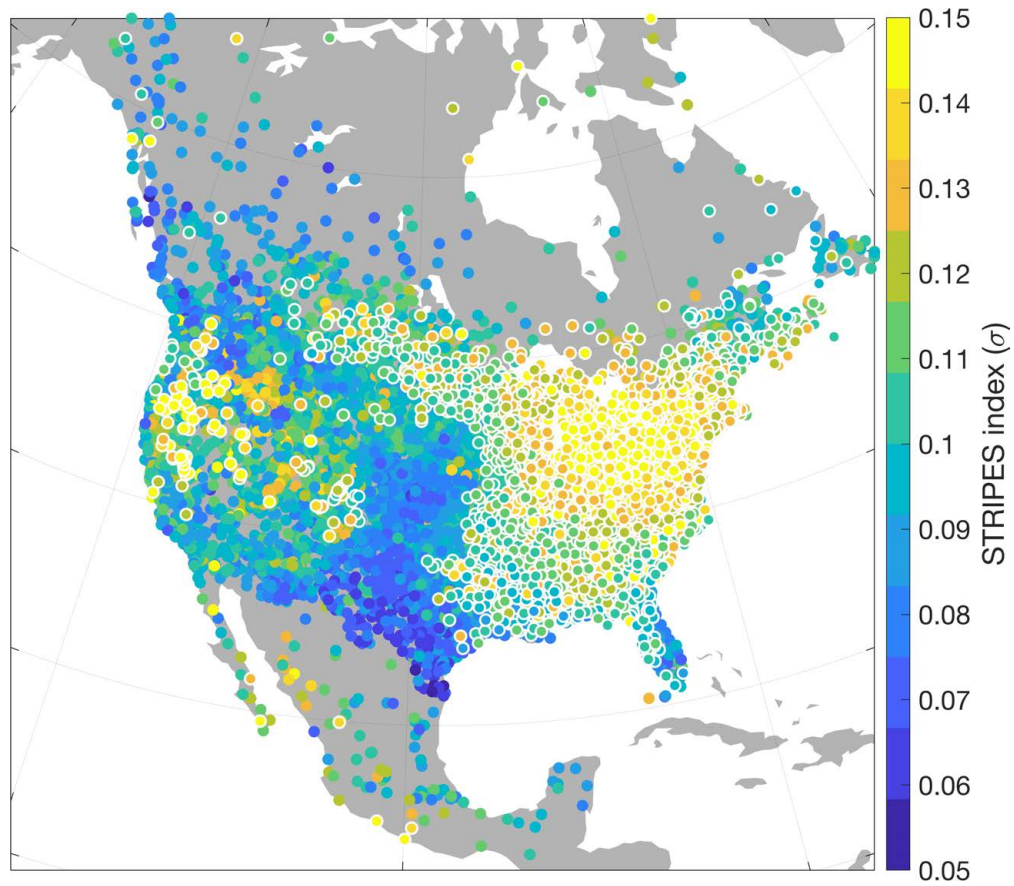


Figure A.4: As in A.1 but MJO days are independent. Additionally, the STRIPES index is calculated using only a slope of 6 days per phase in diagonal averages, and no shifting of phases is done (see main text).

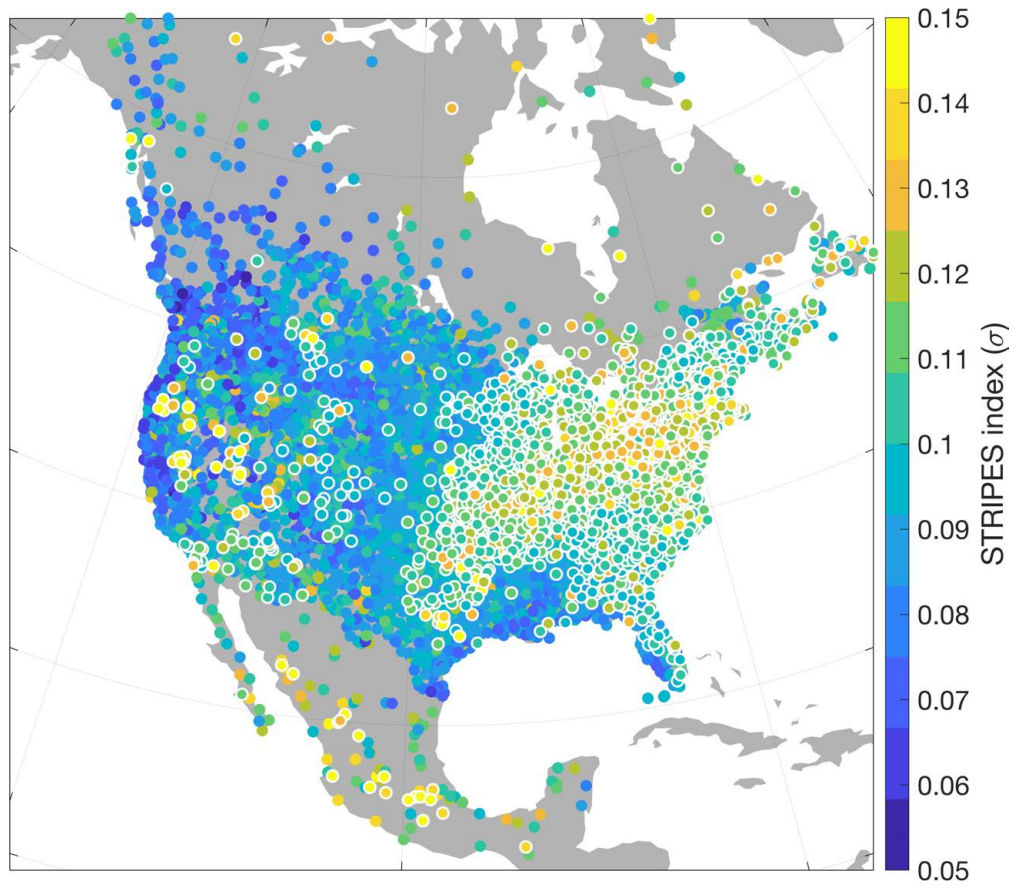


Figure A.5: As in A.4 but for daily minimum temperature (TMIN).

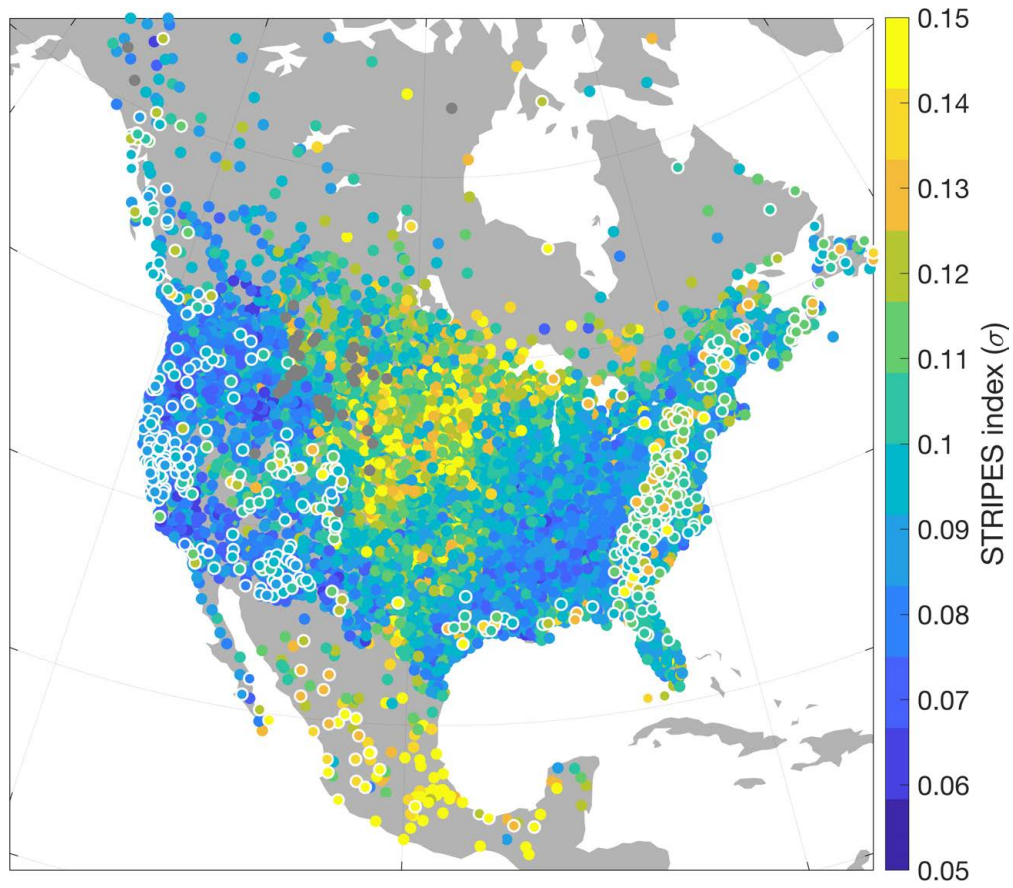


Figure A.6: As in A.4 but for daily precipitation totals (PRCP).

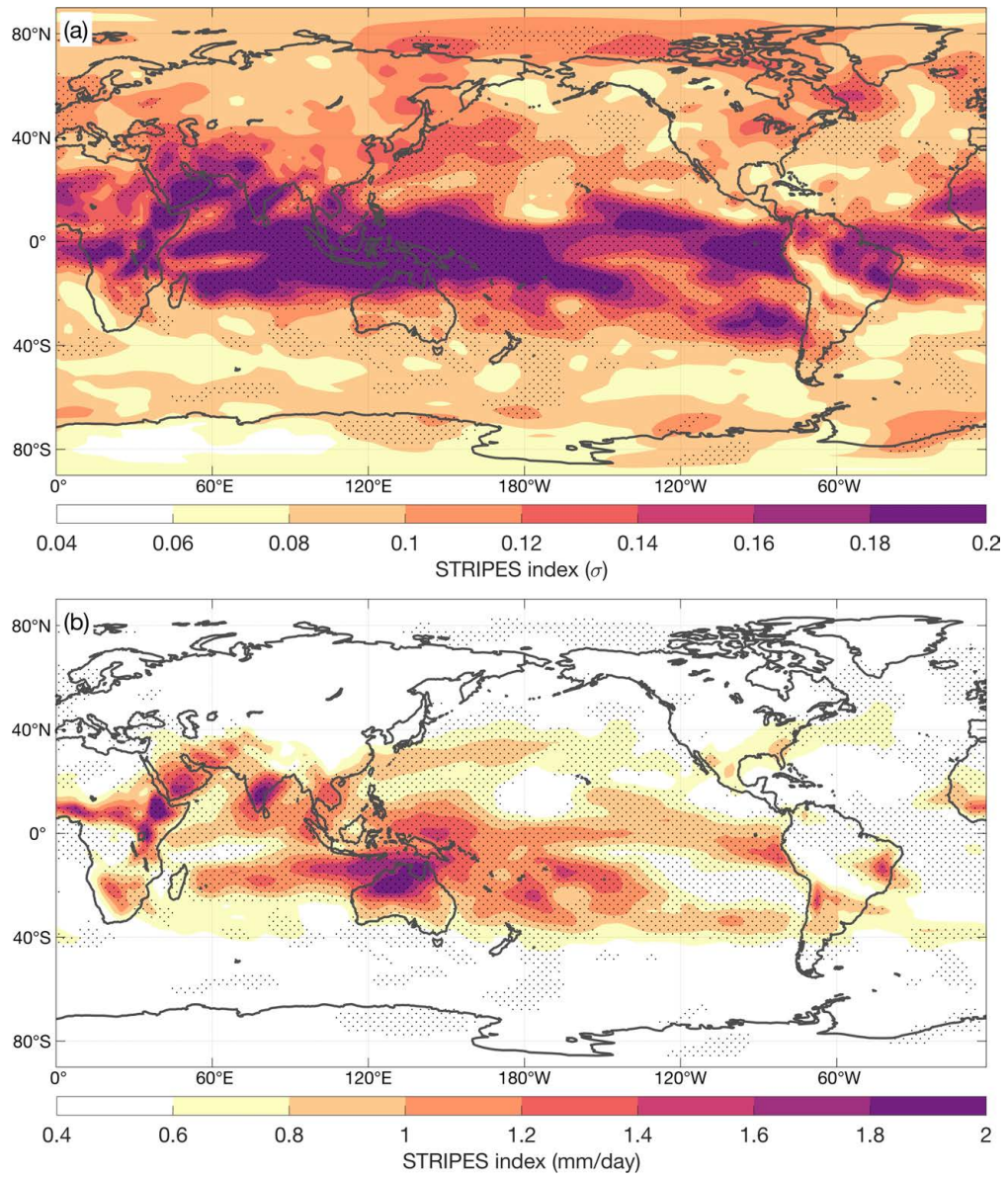


Figure A.7: As in main text Figure 2.6 but for precipitable water.